SEISMIC PERFORMANCE OF POST-TENSIONED CAST-IN-PLACE
REINFORCED CONCRETE BEAMS

A THESIS SUBMITTED TO
THE GRADUATE SCHOOL OF NATURAL AND APPLIED SCIENCES
OF
MIDDLE EAST TECHNICAL UNIVERSITY

BY

ERTÜRK TUNCER

IN PARTIAL FULFILLMENT OF THE REQUIREMENTS
FOR
THE DEGREE OF DOCTOR OF PHILOSOPHY
IN
CIVIL ENGINEERING

JANUARY 2025

Approval of the thesis:

SEISMIC PERFORMANCE OF POST-TENSIONED CAST-IN-PLACE REINFORCED CONCRETE BEAMS

submitted by **ERTÜRK TUNCER** in partial fulfillment of the requirements for the degree of **Doctor of Philosophy** in **Civil Engineering, Middle East Technical University** by,

Prof. Dr. Naci Emre Altun
Dean, **Graduate School of Natural and Applied Sciences**   _____

Prof. Dr. Erdem Canbay
Head of the Department, **Civil Engineering**   _____

Prof. Dr. Barış Binici
Supervisor, **Civil Engineering, METU**   _____

Examining Committee Members:

Prof. Dr. Güney Özcebe
Civil Engineering, TEDU   _____

Prof. Dr. Barış Binici
Civil Engineering, METU   _____

Prof. Dr. Erdem Canbay
Civil Engineering, METU   _____

Prof. Dr. Ahmet Yakut
Civil Engineering, METU   _____

Prof. Dr. Sabahattin Aykaç
Civil Engineering, Gazi University   _____

Date: 10.01.2025

I hereby declare that all information in this document has been obtained and presented in accordance with academic rules and ethical conduct. I also declare that, as required by these rules and conduct, I have fully cited and referenced all material and results that are not original to this work.

Name Last name : Ertürk Tuncer

Signature :

ABSTRACT

SEISMIC PERFORMANCE OF POST-TENSIONED CAST-IN-PLACE REINFORCED CONCRETE BEAMS

Tuncer, Ertürk
Doctor of Philosophy, Civil Engineering
Supervisor : Prof. Dr. Barış Binici

January 2025, 123 pages

Post-tensioning is an efficient solution for reinforced concrete beams in long-span moment-resisting frame systems. This study experimentally investigates the seismic performance of post-tensioned reinforced concrete beams. For this purpose, exterior and interior post-tensioned beam-to-column joints were chosen from a code-compliant prototype frame building and 1:2 scaled specimens were constructed. The primary test variables were mild steel ratio, load-balancing ratio, and specimen location. The laboratory results were examined through comparisons of base shear-lateral displacement, moment-curvature, crack width, energy dissipation, equivalent viscous damping ratio, and stiffness degradation. A simple section analysis approach was taken to specify the minimum mild steel ratio of bonded post-tensioned reinforced concrete beams for ductile response. In addition to those, non-linear finite element analyses were conducted to simulate the behavior of the test specimens and compare with the experimental findings. After validating the model, stress profiles for reinforcing steel and tendon were studied. Lastly, the maximum crack width, tendon stress, confined concrete strain, and ultimate curvature computed using numerical model were compared with experimental results and design codes.

Keywords: Post-tension, Reinforced Concrete Beam, Seismic Design, Mild Steel

ÖZ

ARD-GERMELİ YERİNDE DÖKÜM BETONARME KİRİŞLERİN SİSMİK PERFORMANSI

Tuncer, Ertürk
Doktora, İnşaat Mühendisliği
Tez Yöneticisi: Prof. Dr. Barış Binici

Ocak 2025, 123 sayfa

Uzun açıklıklı moment aktaran çerçeve sistemlerdeki betonarme kirişler için ardgerme etkili bir çözümdür. Bu çalışma ardgermeli betonarme kirişlerin sismik performansını deneysel olarak soruşturmaktadır. Bu amaçla, deprem yönetmeliği ile uyumlu prototip çerçeve bir binadan dış ve iç ardgermeli kolon-kiriş birleşimleri seçilmiştir ve 1:2 ölçekli numuneler inşa edilmiştir. Test değişkenleri yumuşak çelik oranı, yük dengeleme oranı ve numune konumudur. Laboratuvar sonuçları taban kesmesi-yanal deplasman, moment-eğrilik, çatlak genişliği, enerji yayılması, eşdeğer viskozlu sönümleme oranı ve sertlik degradasyonu kıyaslamalarıyla değerlendirilmiştir. Aderanslı ardgermeli betonarme kirişlerin sünek davranışı için minimum yumuşak çelik oranını belirlemek amacıyla basit bir kesit analiz yaklaşımı uygulanmıştır. Bunlara ek olarak, test numunelerinin davranışını simüle etmek ve deney bulguları ile kıyaslamak için doğrusal olmayan sonlu eleman analizleri yürütülmüştür. Modelin doğrulanmasının ardından, yumuşak çelik ve tendon için gerilme profilleri çalışılmıştır. Son olarak, numerik model kullanılarak hesaplanan maksimum çatlak genişliği, tendon gerilmesi, sargılı beton birim deformasyonu ve kopma eğriliği deneysel sonuçlar ve tasarım şartnameleriyle kıyaslanmıştır.

Anahtar Kelimeler: Ardgerme, Betonarme Kiriş, Sismik Tasarım, Yumuşak Donatı

to Gizem and Nehir Mira

ACKNOWLEDGMENTS

TABLE OF CONTENTS

LIST OF TABLES

TABLES

LIST OF FIGURES

FIGURES

LIST OF ABBREVIATIONS

ABBREVIATIONS

ACI	American Concrete Institute
ASTM	American Society for Testing and Materials
c.g.c	Center of gravity of concrete
c.g.s	Center of gravity of prestressing steel
CIP	Cast-In-Place
CP	Collapse Prevention
DR	Drift Ratio
FE	Finite Element
FEA	Finite Element Analysis
FEM	Finite Element Method
FEMA	Federal Emergency Management Agency
FRP	Fiber Reinforced Polymer
LC	Load Cell
LS	Life Safety
LVDT	Linear Variable Displacement Transformer
PTE	Post Tensioned Exterior
PTI	Post Tensioned Interior
RC	Reinforced Concrete
TBEC	Turkey Building Earthquake Code

TS	Turkish Standards
1D	One-dimensional
3D	Three-dimensional

LIST OF SYMBOLS

SYMBOLS

A_{bottom} Bottom mild steel area

A_g Rectangular section gross area

A_{ps} Post-tensioning tendon area

A_s Tension steel area

A_{top} Top mild steel area

A_s' Compression steel area

A_v Web reinforcement area

b Initial tangent ratio of hardening branch

b_{eff} Effective flange width

b_w Section width

c Neutral axis depth

d Distance measured from the top compression fiber of the concrete to the centroid of mild steel in tension zone

d_b Longitudinal rebar diameter

d_p Distance measured from the top compression fiber of the concrete to the centroid of prestressing steel in tension zone

D Overstrength factor

E_c Modulus of elasticity for concrete

E_d Cumulative dissipated energy

E_{ps}	Modulus of elasticity for prestressing steel
E_s	Modulus of elasticity for reinforcing steel
E_{s0}	Strain energy
f_c'	Characteristic compressive strength of concrete
$f_{c,ave}'$	Average characteristic compressive strength of concrete
f_{cd}	Design strength of concrete
f_{ce}	Average compressive strength of the concrete for test samples
f_{ci}'	Compressive strength of concrete at the time of initial prestressing
$f_{c,i}'$	Compressive strength of concrete for i^{th} sample
f_{ct}	Tensile strength of concrete
f_{pd}	Design strength of prestressing steel
f_{pe}	Effective prestress level
f_{pi}	Initial prestress level
f_{ps}	Prestressing steel stress
f_{pu}	Rupture strength for prestressing steel
f_{py}	Yield strength for prestressing steel
f_y	Yield strength for longitudinal rebar and mesh reinforcement
f_{yd}	Design yield strength of reinforcing steel
f_{yt}	Yield strength of the transverse reinforcement
f_u	Ultimate strength for mild steel and mesh reinforcement
f_{ywe}	Average yield strength of the transverse reinforcement

F_c Force due to concrete

$F_i{}^+$ Maximum lateral load at i^{th} cycle in push direction

$F_i{}^-$ Maximum lateral load at i^{th} cycle in pull direction

F_{ps} Force due to prestressing steel

F_s Force due to reinforcing steel

G_c Compressive fracture energy

G_f Tensile fracture energy

h Section height or vertical distance between top and bottom LVDTs used for beam curvature

H Lateral load applied via horizontal hydraulic jack

H_{top} Vertical distance between between horizontal hydraulic jack centerline and beam top face

H_{bottom} Vertical distance between the hinge centerline and beam top face

i Cycle number for hysteresis loop

K_i Initial stiffness

K_{sec} Secant stiffness

L Shear span length

l_n Clear span length

l_p Plastic hinge length

L_0 Initial length of LVDT

L_A Horizontal distance component of curve AC

L_B Horizontal distance component of curve BC

L_T	Total length of tendon span
M	Bending moment
M_{cr}	Cracking moment capacity of a section
M_j	Total moment at beam-to-column joint
$M_{j,lower}$	Joint moment contribution due to lower storey
$M_{j,upper}$	Joint moment contribution due to upper storey
M_{max}	Maximum moment
M_r	Ultimate moment capacity of a section
M_u	Factored bending moment
N	Axial load
N_u	Factored axial load
P	Prestressing force
R	Behavior factor
R_0	Initial curvature
R_1	Support reaction obtained through strain gauge
R_2	Vertical support reaction at the pinned support
s	Transverse reinforcement spacing
s_w	Clear distance between adjacent webs
S_{DS}	Design spectral acceleration coefficient for the short periods
S_{D1}	Design spectral acceleration coefficient for $T = 1$ sec.
S_s	Spectral acceleration coefficient for the short periods
S_1	Spectral acceleration coefficient for $T = 1$ sec.

V	Shear
V_c	Shear contribution of concrete only (either $V_{con,ps}$ or $V_{con,rc}$)
$V_{con,ps}$	Shear contribution due to concrete for the prestressed sections
$V_{con,rc}$	Shear contribution due to concrete for the reinforced concrete sections
V_{flex}	Shear force due to flexure
V_{max}	Maximum shear
V_{shear}	Shear capacity of a section
V_{steel}	Shear contribution provided by the transverse steel only
V_y	Yield lateral load
V_u	Factored shear force
V_{ult}	Ultimate lateral load
w_b	Balanced distributed load
w_{max}	Maximum crack width
w_{res}	Residual crack width
x	Distance measured from column's outer face
y_A	Tendon elevation at point A
y_B	Tendon elevation at point B
$\bar{y}$	Geometric center of a section measured vertically from the bottom face
z	Shear span
α_{se}	Coefficient for confining steel
α_1	Material constant
α_2	Material constant

α_3 Material constant

α_4 Material constant

β_1 Factor relating depth of equivalent rectangular compressive stress block to depth of neutral axis

Υ_p Factor used for prestressing reinforcement type

ε Strain

$\varepsilon_c{}^{CP}$ Confined concrete strain at collapse prevention limit state

ε_{cu} Crushing strain of concrete

$\varepsilon_{cu,c}$ Confined concrete strain

ε_{py} Yield strain of prestressing steel

ε_s Strain at the level of tension steel

ε_{sh} Strain hardening level for mild steel

ε_{bottom} Average strain of LVDT positioned on the bottom face of the beam

ε_{top} Average strain of LVDT positioned on the top face of the beam

ε_u Ultimate strain for mild steel and mesh reinforcement

ε_y Yield strain for mild steel and mesh reinforcement

ρ Tension steel ratio ($^{A_s}/_{b_w d}$) for beams

ρ' Compression steel ratio ($^{A_s{}'}/_{b_w d}$) for beams

ρ_p Prestressing steel ratio ($^{A_{ps}}/_{b_w d_p}$)

$\rho_{sh,min}$ Minimum of the volumetric ratio of the transverse reinforcement in both directions

σ Stress

$\Delta_i{}^+$ Maximum lateral displacement at i^{th} cycle in push direction

$\Delta_i{}^-$ Maximum lateral displacement at i^{th} cycle in pull direction

Δ_h Lateral displacement at the column tip

ΔL_{top} Average displacement of LVDT positioned on the top face of the beam

ΔL_{bottom} Average displacement of LVDT positioned on the bottom face of the beam

Δ_u Ultimate displacement

Δ_v Vertical displacement at the column tip

Δ_y Yield displacement

ϕ Curvature

ϕ_u Ultimate curvature

ϕ_y Yield curvature

μ_ϕ Curvature ductility (ϕ_u/ϕ_y)

μ_Δ Displacement ductility (Δ_u/Δ_y)

ψ_p Prestressing steel index

ζ_{eq} Equivalent viscous damping ratio

CHAPTER 1

INTRODUCTION

1.1   General

Post-tensioning technology is primarily preferred in moment-resisting frame structures due to its superior properties such as enabling the use of thinner slabs, longer spans, and shorter floor heights with the help of reduced beam and slab depths (Aalami, 2023). In 1872, the concept of prestressed concrete was first introduced by P.H. Jackson who used tie rods to design a beam with the aid of a series of blocks. In 1888, C.W. Doehring developed a system using metal wires for prestressing slabs. In the early 1920s, W.H. Hewett suggested the idea of circular prestressing by applying hoop-stressed horizontal reinforcement along the tank perimeter to prevent cracking due to internal liquid pressure. However, these attempts were unsuccessful since the time-dependent losses associated with prestressing could not be compensated. To address this issue, Eugene Freyssinet proposed a method using high-strength concrete and high-strength steel. In 1940, he designed the Freyssinet system incorporating the conical wedge anchors for 12-wire tendons. In 1963, T.Y. Lin presented a principle known as the load-balancing technique utilizing the vertical force component of the tendons to counteract the gravity loads applied on the beam (Nawy, 2009). The theory behind prestressing can be summarized as follows: Concrete is strong in compression but weak in tension, causing flexural cracks during the initial loading phases. To mitigate this problem, an external compressive force is applied in the longitudinal direction of the structural element. Consequently, it reduces the tensile stresses occurring at mid-span and supports, resulting in a strain profile that is almost entirely in compression throughout the section height.

Today, post-tensioning is commonly used in the floor systems of reinforced concrete (RC) buildings, such as flat slabs and beam slabs, and in numerous types of bridge

systems. Additionally, it can be carried out for the design of high-rise buildings, airports, silos, nuclear reactor vessels, and underground structures. Figure 1.1 illustrates some examples of post-tensioned structures in Turkey. The post-tensioning process involves the following steps: (1) Strands are placed in longitudinal ducts before the concrete is cast, and they are tensioned after the concrete gains adequate strength. (2) The prestressing ducts are filled with epoxy-based cement grout to provide permanent protection for the strands and to establish a bond between the prestressing steel and the surrounding concrete. In post-tensioned RC beams, the use of parabolic tendon layout helps to carry more loads since the load-balancing method provides additional shear resistance.

(a) Atatürk Airport multi-story car park
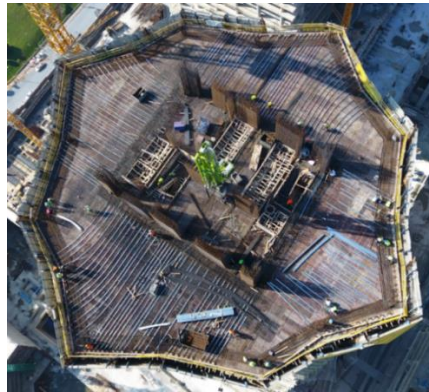
(b) Vakıfbank General Directorate, post-tensioned flat slab

Figure 1.1 Examples of post-tensioned structures (Photo courtesy, Freysas Sustainable Technology)
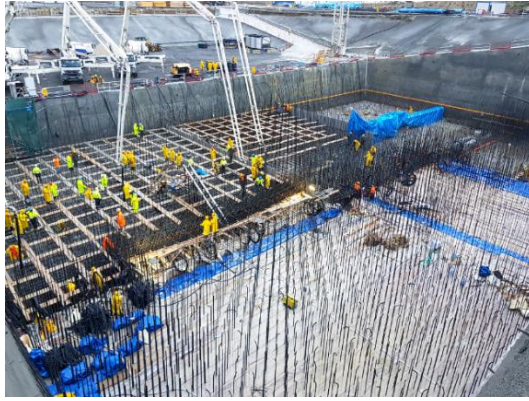
(c) Canakkale 1915 Bridge, anchorage blocks

(d) Ankara Sheraton Hotel Culture and Conventional Center, beam-slab

(e) İzmit Nuh Cement Silo Factory

Figure 1.1. (cont'd)

In the serviceability design of a post-tensioned RC beam, the tensile and compressive stresses in the concrete section are calculated at the supports and mid-span for various stages (i.e., at transfer and after the completion of long-term losses). Then, these stresses are compared with the allowable limits specified by design codes such as ACI 318, Eurocode, and TS3233. Furthermore, the design guidelines provided in the earthquake specifications are strictly followed, particularly for beam-to-column connection details. In seismic design, lateral loads obtained from the elastic design spectrum are reduced using the behavior factor (R) and overstrength factor (D). Following the ultimate design phase, the tendon area and the amount of reinforcing steel are determined through structural analyses considering all possible load combinations of gravity and earthquake forces.

As a result of the initial prestressing force, localized compressive stresses are observed in the regions near the supports. Several practical methods are available to reduce this excessive stress accumulation. For instance, tendon eccentricity can be adjusted by raising certain parts of the tendon toward the support zone. Another alternative is to provide necessary anchorage reinforcement (i.e., closed ties, stirrups) over a short segment of the tendon. Mild steel is typically employed in post-tensioned beams as it helps to carry a portion of ultimate flexural moment. Additionally, non-prestressed steel controls the excessive camber due to the long-term creep of the concrete, restricts crack width, and improves ductility. Prestressing steel enhances stiffness, contributes to self-centering ability, and reduces plastic deformation. Therefore, it is essential to optimize the benefits of each component in a post-tensioned RC beam section. Consequently, the combination of tendon and mild steel, known as the partial prestressing, has emerged. An optimal layout of tendon and reinforcing steel is needed to achieve a safe and economical design.

This work has been conducted to investigate the seismic response of post-tensioned cast-in-place RC beams. In this chapter, a comprehensive literature review of both numerical and experimental studies is presented. Subsequently, the objectives and scope of the research are outlined.

4

1.2   Literature Review

Park and Thompson (1977) conducted tests on ten post-tensioned interior reinforced concrete beam-to-column sub-assemblages subjected to cyclic loading. They compared the structural performance of fully and partially prestressed test specimens. The experimental results indicated that transverse steel was necessary in the plastic hinge zones of the joints to provide confinement and prevent diagonal tension failure. It was also found that mild steel placed in the compression zone increased the ductility of the connection. Then, it was concluded that the partial prestressing improved the deformation capacity.

Thompson and Park (1980) carried out a parametric study to assess the moment-curvature responses of post-tensioned RC rectangular beam sections. The longitudinal rebar ratio, mild steel configuration, strand area, and prestressing steel layout were identified as primary test variables. The study revealed that fully prestressed rectangular sections with a single layer of strand exhibited greater moment capacity as the tendon area increased. However, a sudden capacity drop was seen as the ratio of strand area to concrete area became larger. Besides, the researchers recommended designing beams with at least two symmetrically placed prestressing tendons. They also noted that the sections with one layer strand exhibited lower energy absorption capacity (i.e., a more brittle response) since the compressive load was resisted solely by the concrete. For this purpose, mild steel was added to increase the ductility level of the section. In the case of partially prestressed beams, parametric study showed that the presence of a central prestressing steel delayed cracking and enhanced the strength without significantly reducing the ductility. Additionally, all moment-curvature relations obtained were verified by the experimental results.

Naaman et al. (1986) focused on the ductility analysis of partially prestressed reinforced concrete flexural members. Accordingly, an extensive parametric study was performed to evaluate the curvature ductility of such structural elements using several variables such as concrete compressive strength, partial prestressing ratio,

prestressing steel grade, and reinforcing index. The researchers compared the analytical results with the ones gathered from experimental studies, then, they developed some mathematical equations about the curvature ductility and plastic rotation. The results demonstrated that a reduction in the effective prestressing level led to smaller curvature ductility due to delayed yielding. Partial prestressing had minimal impact on the section ductility. It was also seen that lower ductility indices were obtained with the usage of high-strength concrete.

Interior post-tensioned beam-to-column joints subjected to the reversed cyclic loading were experimentally studied by Cheok and Lew (1991,1993). They aimed to understand the effects of post-tensioning steel configuration and fully vs. partially prestressed bonded strand application on the structural behavior. The test results were also evaluated by comparing the hysteresis responses of precast and monolithic specimens. Accordingly, connection strengths and ductility levels were similar for both joint types. The other remarkable point was that the partial prestressing emerged as a strong alternative to achieve higher energy capacity.

Priestley and Tao (1993) performed an analytical study to test the seismic behavior of precast prestressed interior beam-to-column joints with partially debonded tendons. Consequently, this research pointed out that an appropriate debonding length on either side of the column increased the shear capacity and minimized residual deformations.

Stanton (1997) and Stone (1995) conducted several experiments on the seismic performance of partially prestressed precast RC joints. Based on this research, the researchers found out that the hybrid system exhibited minor damage. Similarly, it was observed that the cracks disappeared upon unloading. On the other hand, the monolithic RC joint showed visible cracks and experienced sudden shear strengh degradation. Besides, it was stated that such a joint could be designed to achieve similar flexural strength with the equivalent conventional RC specimen.

Priestley and MacRae (1996) investigated the cyclic behavior of exterior and interior unbonded post-tensioned beam-to-column joints. The test results indicated that the

deformation capacities of both specimens exceeded the design drift level of 2%. It was seen that the cracks were uniformly distributed throughout the connection zone. Additionally, the ratio of residual displacement to maximum displacement was negligibly small since the post-tensioning steel helped restore the joint to its original position.

El-Sheikh et al. (1999) studied the seismic design of two six-story unbonded post-tensioned precast concrete frames using pushover and time-history analyses. Firstly, they developed two analytical models to understand the response of interior beam-to-column connections. In the fiber model, it was assumed that linear elastic deformations occurred in the beam and column elements. Truss elements were used for unbonded tendons. Shear deformation of the panel zone was constructed using zero-length spring elements. In the spring model, non-linear behavior was incorporated using zero-length rotational springs. Both models well predicted the hysteretic behavior of the joints tested in the laboratory. After validating the models with experimental results, the researchers carried out non-linear static and dynamic analyses for the frames. Then, this study concluded that unbonded post-tensioned precast beam-to-column sub-assemlages provided satisfactory behavior in terms of strength, ductility, and stiffness.

Kashiwazaki and Noguchi (2001) conducted several experiments to test the seismic behavior of interior post-tensioned RC beam-to-column joints. These joints were also numerically analyzed using non-linear finite element method (FEM) to verify the laboratory outputs. The main purpose of this study was to investigate the influence of prestressing force level on the shear capacity of the connections. The results obtained from both numerical simulations and experiments revealed that the joint shear capacity was not significantly affected by the prestressing force. However, the cracks with smaller angle were observed as the initial prestressing force increased. It can be attributed to the self-centering ability of post-tensioning strands.

Alcocer et al. (2002) tested two full-scale beam-to-column joints in a precast concrete frame under cyclic loading. The main test variable in this study was the presence of prestressing. Accordingly, it was understood that unbonded post-tensioning strands reduced beam rotations at the joint region. The results indicated that unbonded post-tensioning strands reduced beam rotations at the joint region. Additionally, the post-tensioned specimen experienced the strength degradation at a drift ratio of approximately 3.5%. Based on these results, it was inferred that the specimen exhibited a ductile response.

The exterior post-tensioned and conventional reinforced concrete beam-to-column regions subjected to the reverse cyclic loading were experimentally tested by Hamahara et al. (2007). The amount of mild steel and strand, tendon eccentricity, and, the location of tendon anchorage were investigated in the context of this study. At the end of the laboratory program, the researchers developed a shear design procedure for the post-tensioned joint types. The proposed method showed a good agreement with the experimental data.

Ozden and Ertas (2007) carried out some experiments on exterior post-tensioned precast beam-to-column connections subjected to displacement-controlled reverse cyclic loading. The main goal of this study was to understand the effect of mild steel on the joint's structural performance. The researchers observed that the flexural strengths of test specimens did not significantly change up to a drift ratio of approximately 4%. Additionally, it was noted that the joint zones behaved in a more ductile manner as the mild steel amount increased. They also suggested that an optimal amount of reinforcing steel was in the range of 20% to 30% based on the key structural parameters such as strength, deformability, and energy dissipation capacity.

Hawileh et al. (2010) implemented three-dimensional (3D) non-linear finite element (FE) analysis to estimate the structural response of interior precast beam-to-column joints under cyclic loading. In the scope of this research, stress and strain fields for both mild reinforcement and post-tensioning tendon were investigated. Accordingly,

the results showed that the stresses in the strands remained below the yield line during the tests. Besides, the connection failed due to the fracture of mild steel. The authors emphasized that high accuracy was attained between numerical model and laboratory tests.

In the study of Davey et al. (2016), two half-scale exterior post-tensioned reinforced concrete beam-to-column connections were designed in accordance with Australian standards. While one of the specimens had uniform strand distribution across the beam width, outer tendon layout of the other specimen was highly close to the joint region. The researchers also employed 3D finite element analysis to model the test setup. According to the experimental results, both specimens exhibited satisfactory performance without substantial drop in the lateral load capacity until a drift ratio of around 3%. It was observed that different tendon layouts did not significantly affect the structural behavior. Another key finding was that the post-tensioning facilitated the closure of cracks upon unloading. Furthermore, parametric analysis results signified that higher levels of prestressing force led to a reduction in overall ductility.

Wang et al. (2018) implemented some experiments on post-tensioned precast beam-to-column joints through a series of quasi-static tests. The researchers proposed a model to improve seismic performance of the precast joints. Accordingly, steel jacket was applied close to beam ends to prevent the failure of concrete spalling. Steel angles were used to transfer the shear forces throughout the beam-to-column zone. Post-tensioning strands enabled minimizing the residual deformation and improving self-centering ability. The reinforcing steel acted as replaceable energy dissipators, thereby increasing the ductility level of the joint. In the scope of this study, monolithic RC joint was also investigated. The laboratory results indicated that the conventional sub-assemblage demonstrated larger crack widths relative to the those of precast specimens. Based on the experimental observations, it was concluded that the precast beam-to-column connection presented adequate structural performance.

Guan et al. (2019) examined the seismic performance of full-scale post-tensioned precast interior beam-to-column connections under reverse cyclic loading. They introduced the application of arc-shaped prestressing steel as a novel alternative. While the upward prestressing bars contributed to the moment-bearing capacity of the beam, the downward ones provided additional resistance against construction loads. A conventional specimen was also designed for comparison purposes. Test results demonstrated that both joint types-precast and monolithic-exhibited similar behavior in terms of ductility, strength, and stiffness.

Zhou et al. (2020) analyzed damage developments of hybrid joints using the results compiled from existing experimental studies. Accordingly, they constructed a numerical model calibrated with the test results. Then, an explicitly defined damage model was recommended to evaluate the performance of the beam-to-column connections. Several variables involving the initial stress of the strand, concrete compressive strength, and transverse reinforcement ratio were examined. The results revealed that higher initial stress decreased the plastic rotation since the post-tensioning strand limited the residual deformations. Also, a higher amount of transverse steel enhanced the confined strength of the concrete, therefore, a greater deformation capacity was obtained in the joint region.

Cai et al. (2021) proposed an innovative method for self-centering precast beam-to-column connections utilizing unbonded post-tensioning strands along with steel top and seat angles. In the scope of that research, several test parameters such as initial prestressing force, beam depth, and seat angle layout were investigated. In addition to the experimental work, numerical simulations were performed to examine the seismic behavior of the joints under cyclic loading. The study showed that post-tensioning enhanced the self-centering ability, thereby minimizing residual deformations in the joint zones. On the other hand, steel angles played a critical role to improve energy dissipation capacity of the connections. Consequently, the specimens with steel angles showed more ductile behavior compared to the others. Also, the findings indicated that increasing the initial prestressing force level contributed to a higher load-carrying capacity and greater initial stiffness.

Hwang et al. (2021) evaluated the behavior of post-tensioned precast concrete beam-to-column joints under reverse cyclic loading. The effective prestress of tendons and the compressive strength of the grout were selected as control variables. The researchers also tested a monolithic RC specimen to understand the effect of post-tensioning on the seismic performance. The experimental study revealed that the high level of prestressing caused early crushing of the concrete at the joint zone. For this reason, it was necessary to increase the amount of transverse steel at the beam-to-column joint. Additionally, the grout strength had no major impact on the lateral load capacity of the specimen. While all precast specimens failed due to the crushing of concrete at the beam end zones, the conventional specimen exhibited shear failure near the joint region. As a result, several flexural cracks were observed and severe damage occurred in the panel zone of RC specimen. In light of experimental results, the researchers also proposed an analytical model to investigate the bond-slip failure between the concrete and the tendon using zero-length springs. Accordingly, it was noted that the analytical model successfully captured the hysteretic behavior obtained from the experiments.

Paudel et al. (2022) analyzed the seismic behavior of post-tensioned precast wide U-shaped interior beam-to-column joints through numerical simulations. In this study, several reinforcement arrangements involving spandrel reinforcement, post-tensioning strand, and A-truss rebar were used. The analysis results showed that the spandrel beam reinforcements provided better moment transfer and the transverse prestressing strands improved the lateral confinement. It was observed that the crack formation occurred in the later stages of loading history for the specimens with post-tensioned strand and transverse mild steel. Besides, prestressed and non-prestressed steel used in modified joints made significant contributions to the lateral load capacity and energy dissipation as compared to the control specimen.

Three full-scale RC beam-to-column joints were numerically and experimentally examined by Wu et al. (2023) to discover the seismic response of connection systems. The test specimens were categorized into three groups: (i) a combination of bolted angles and post-tensioning tendons, (ii) only post-tensioning tendons, and (iii)

only bolted angles. The laboratory findings revealed that the use of only post-tensioning significantly enhanced self-centering ability and ultimate displacement capacity. On the contrary, the joint with only bolted angles presented a stable energy dissipation capacity. Then, it was concluded that the combination of both elements in a joint exhibited a perfect structural performance. In the second part of this research, FE model was validated using the hysteresis curves obtained from the experiments. Then, calibration was applied for this model and a parametric study was conducted to analyze the effects of the variables such as initial prestressing force, tendon area, initial bolt force, bolt grade, and section geometry on the joint behavior. Accordingly, higher lateral load capacity was attained with the increase in the initial prestressing force and strand area. Besides, the ratio of initial bolt force to the bolt grade was defined within a limited range.

Liao et al. (2024) performed several tests to investigate the cyclic response of precast concrete beam-to-column connections with partially bonded draped prestressing tendons. For this purpose, they designed exterior and interior precast specimens and compared their responses with the equivalent post-tensioned cast-in-place (CIP) reinforced concrete ones. The findings of this research implied that the interior specimen exhibited greater lateral load capacity and initial stiffness compared to those of exterior one due to the presence of two T-shaped beams. Also, the maximum drift ratios were 3.5% and 2.5% for interior and exterior joints, respectively. It was concluded that the recommended precast joint could be used in high seismic zones since it satisfied the life safety (LS) performance requirements. The overall performances of the conventional and precast specimens were highly close to each other.

Srisuwan and Yooprasertchai (2024) proposed an innovative technique that combines steel slit dampers and prestressing tendons to evaluate the seismic performance of exterior beam-to-column precast concrete joints through quasi-static cyclic loading tests. For this purpose, test specimens with and without post-tensioning strands were constructed. The experimental results revealed that post-tensioned joints improved self-centering ability, resulting in smaller inelastic

deformations. Also, it was understood that steel slit dampers enhanced dissipation capacity and prevented major structural damage. Consequently, a slower rate of stiffness degradation was observed since the prestressing steel mitigated the pinching effect. The bonding between the tendon and surrounding concrete improved seismic behavior of the joint by reducing tensile stresses occurring near the column edge surfaces.

The beam-to-column connection is a critical factor in evaluating the seismic performance of reinforced concrete structural systems. The past earthquakes have shown that the majority of the severe damage occurred in these joint zones. The poor material properties, lack of transverse reinforcements, and improper seismic design details are the main causes of the building failures. For this purpose, some retrofitting techniques such as fiber reinforced polymer (FRP) and steel jacketing have been developed. In addition to those, Maddah et al. (2020), Khodaei et al. (2021) and Yurdakul and Avsar (2016) conducted several experiments using the combination of steel angles and post-tensioning bars as local retrofitting technique through the joint panel. Based on this method, the connection area was enlarged to increase load carrying capacity, enhance ductility level, and improve energy dissipation capacity. This retrofit system also reduced the shear demand inside the core region, and higher shear capacity was obtained due to the confinement effect of the steel angles. Similarly, post-tensioning minimized the pinching effect on the load-displacement response. The test results demonstrated that this strengthening application prevented the shear failure and satisfied the design principle of strong column-weak beam.

In general, the post-tensioned RC beam-to-column sub-assemblages exhibit lower displacement ductility as compared to the conventional ones. The reasoning behind this behavior can be attributed to the brittle material characteristics of the tendon. For this reason, such systems are supported by the mild steel to increase deformation capacity. On the other hand, yielding and fracture of reinforcing steel cause irrecoverable repair at the joint zone. Then, externally placed energy devices such as friction dampers, fuse-type dissipaters, lead-extrusion dampers have been proposed as innovative method in the last two decades since they provided large non-linear

displacements without significant damage. Accordingly, the previous studies showed that the joints equipped with the post-tensioning strand, mild steel, and energy devices improved lateral stiffness and provided higher energy dissipation (Quing et al. (2023), Huang et al. (2020,2021), Morgen et al. (2008), Feng et al. (2021)).

In light of the literature review, the following inferences can be made:

- The majority of existing studies have focused on precast concrete beams. Therefore, more comprehensive research on post-tensioned cast-in-place members both for interior and exterior beam-to-column connections is required to investigate seismic performance for different levels of post-tensioning and mild steel ratios.

- The effect of load-balancing ratio on the structural performance has not been extensively investigated. In this regard, seismic design targets may not be adequately achieved since tendon geometry, steel reinforcement layouts, and prestressing strand area may affect ductility and deformation capacities.

- The minimum tensile mild steel ratio providing a ductile response for post-tensioned RC beams has not been investigated. Similarly, the relationship between member ductility and seismic behavior factors has not been explicitly described. Such uncertainties could result in major design errors. Consequently, it is difficult to obtain a optimal design for structural engineers. For this reason, further work might be needed to clarify and fill these gaps.

- The maximum crack width and residual crack width for post-tensioned cast-in-place beams have not been studied in detail. Post-earthquake investigations in such systems may require an understanding of the residual damage and maximum sustained deformation.

1.3 Aim and Scope

The main goal of this research is to understand the seismic behavior of post-tensioned cast-in-place reinforced concrete moment-resisting frames. The objectives of the study are given as follows:

- To investigate the effects of mild steel ratio, load-balancing ratio, specimen location (i.e., exterior, interior), and presence of prestressing on the seismic response of post-tensioned cast-in-place RC beam plastic hinge regions,
- To evaluate the ductility levels of post-tensioned cast-in-place RC beams by comparing moment-curvature responses, base shear-lateral displacement curves, maximum and residual crack width measurements, and energy, damping, and stiffness properties,
- To investigate minimum tensile non-prestressed steel ratio for bonded post-tensioned reinforced concrete beams,
- To compare and validate non-linear finite element-based analyses with experimental results,
- To investigate damage progression, plastic hinge length, and stress profiles for reinforcing steel and prestressing strands through finite element analyses,
- To analyze the maximum crack width, tendon stress, confined concrete strain, and ultimate curvature obtained from finite element simulations by comparing experimental data and design code recommendations.

In this regard, a full-scale four-story prototype building was modeled and examined using structural analysis methods. Member dimensions, reinforcement layouts, and tendon geometries were determined in accordance with relevant design specifications. Then, beam-to-column sub-assemblages were isolated by considering the inflection points of the prototype building. In this research project funded by the Scientific and Technological Research Council of Turkey (TUBITAK) under grant number 119M973, a total of seven 1:2 scaled specimens were constructed and tested due to the physical limitations of Structural Mechanics Laboratory of Middle East

Technical University. The flowchart of the project is given in Figure 1.2 on which the scope of this thesis study is highlighted in green.
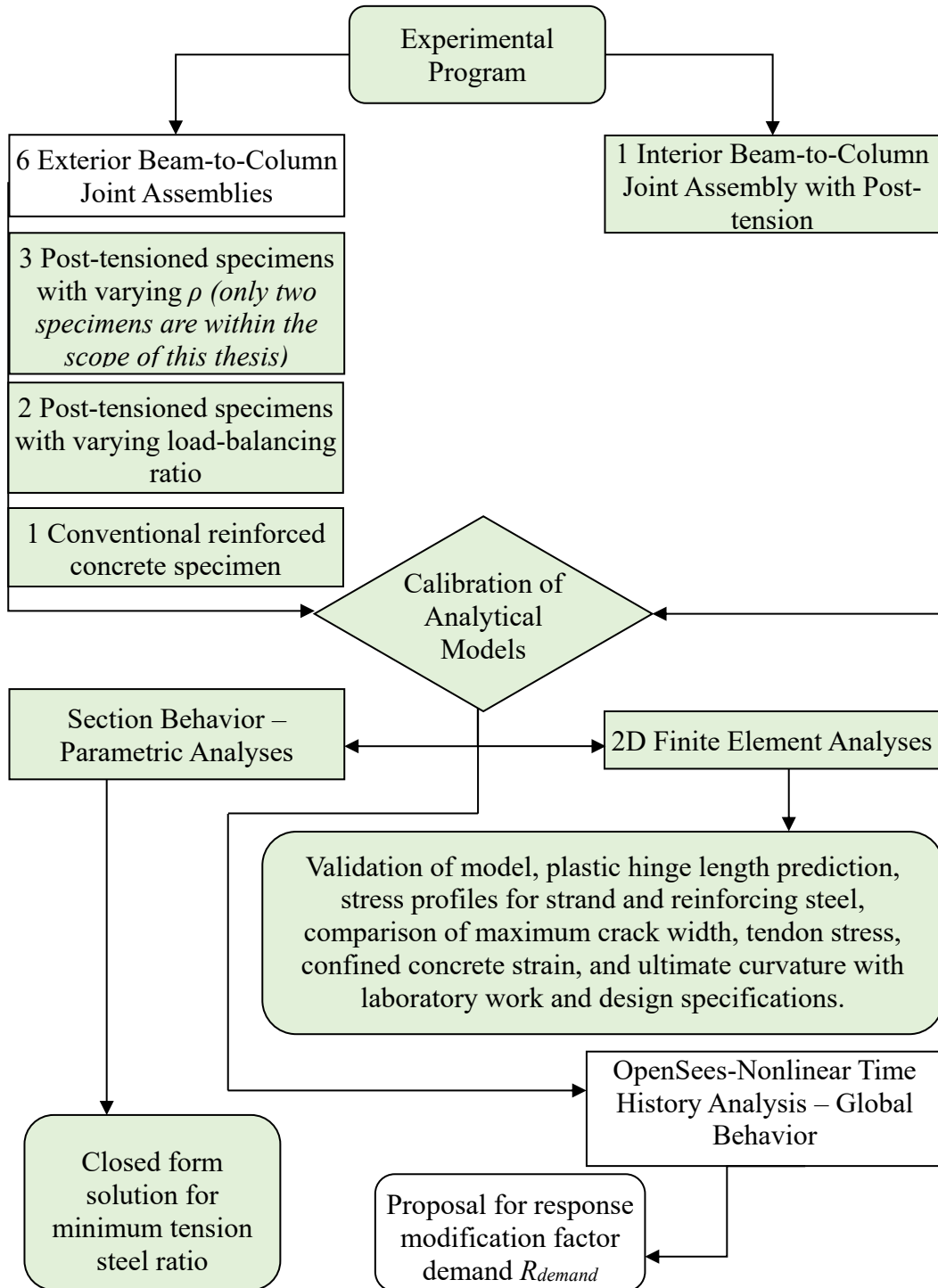

Figure 1.2. The flowchart of the research project

1.4   Organization of Thesis

This thesis study is composed of four chapters. Chapter 1 presents an overview of the chronological development, prominent characteristic properties, and application phases of post-tensioning. Moreover, a detailed literature review is provided in the same section. Then, the aim and scope of this thesis are defined. Chapter 2 introduces a comprehensive description of the experimental procedure. Exterior and interior test specimens were designated by considering the inflection points of four-story moment resisting frame building analyzed. Then, 1:2 scaling factor was adopted for the specimen preparation due to physical constraints of the laboratory. It is necessary to emphasize that all experimental stages including concrete casting, framework construction, reinforcement detailing, and post-tensioning were conducted in the Structural Mechanics Laboratory at Middle East Technical University. Displacement-controlled cyclic loading protocol was carried out for five beam-to-column sub-assemblages. Consequently, base shear-lateral displacement, moment-curvature, column axial load-lateral displacement, beam moment-bar slip rotation, tendon force-lateral displacement, maximum crack width-residual crack width, crack patterns, and damage photographs were obtained for each specimen. The test beams were also compared in terms of their normalized stiffness degradation, cumulative dissipated energy, and equivalent viscous damping ratio responses. Chapter 3 consists of parametric and numerical studies. A simplified sectional analysis was implemented for the post-tensioned reinforced concrete rectangular sections involving a single layer of prestressing strand and mild steel. For this purpose, strain profile and stress distribution were drawn based on the ultimate limit state assumptions. Then, a force equilibrium equation depending on several parameters was explicitly formulated. Accordingly, the maximum value of prestressing steel index was employed to achieve the minimum mild steel ratio for bonded post-tensioned beams. In numerical study, base shear-lateral displacement curves obtained through non-linear finite element analyses were validated with the laboratory test outputs. Following the model calibration, stress profiles of

prestressing steel and mild steel were developed to estimate the specimens' plastic hinge lengths along the shear span. Then, the results were compared with empirical equations and experimental recordings. Furthermore, quantitative analyses were conducted to evaluate maximum crack width, tendon stress, confined concrete strain, and ultimate curvature obtained through finite element modeling, experiments, and design specifications.

CHAPTER 2

EXPERIMENTAL PROGRAM

2.1   General

This study examines the seismic performance of cast-in-place (CIP) reinforced concrete (RC) moment-resisting frames with post-tensioned beams. For this purpose, a four-story prototype frame building with three spans was modeled and analyzed under the combined effects of gravity and seismic loads. In the serviceability design of the post-tensioned RC system, the stresses in the beam section were computed in accordance with the limits of TS3233. The seismic design was conducted following the guidelines of TBEC, while TS500 served as the basis for the gravity design. Upon completion of ultimate and serviceability design stages, the dimensions of all structural elements and the reinforcement layouts were designated. The inflection points for the beams and columns were determined through structural analyses as described in detail below. Then, prototype building was isolated using these critical locations, and beam-to-column sub-assemblages were identified. The experimental setup was constructed by considering these boundary conditions. However, 1:2 scaled specimens were tested due to the physical inadequacy of the laboratory area. The scaling ratios applied to measurements are summarized in Table 2.1.

Table 2.1 Scaling Ratios

Measurement	Scaling factor	
Stress	1:1	dependent
Density	1:1	dependent
Length	1:2	independent
Area	1:4	dependent
Volume	1:8	dependent

Table 2.1 (cont'd)

Force	1:4	dependent
Moment	1:8	dependent

In the scope of this study, a total of five specimens were tested. All procedures related to the preparation of the experimental setup involving the formwork construction, the casting of concrete, post-tensioning application, and placement of reinforcing steel were performed in the Structural Mechanics Laboratory at Middle East Technical University. The mild steel ratio, load-balancing ratio, and specimen location were considered as control variables in this research. The details of the experimental program will be explained in the following sections.

2.2 Prototype Frame Structure

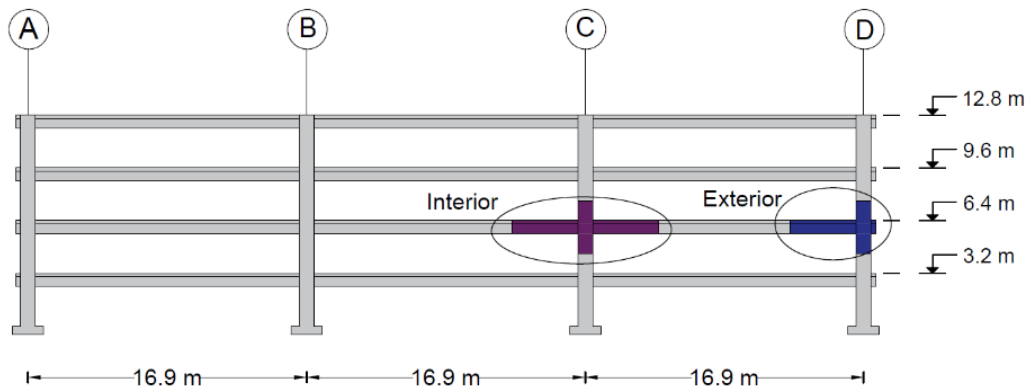### 2.2.1 Building Geometry and Material Properties

The three dimensional view and floor plan of the four-story prototype building are presented in Figures 2.1a and 2.1b. The structure consisted of three bays in both directions. The center-to-center span lengths of each bay were 16.9 m and 8.0 m in the x and y directions, respectively. Each floor had a height of 3.2 m and a slab thickness of 20 cm. All columns had the dimensions of 90 cm × 90 cm. In the long direction, post-tensioned RC beams with cross-sectional dimensions of 80 cm × 80 cm were designed. In the short direction, the cross-sectional dimensions of the exterior and interior conventional RC beams were 120 cm × 80 cm and 80 × 80 cm, respectively. The exterior and interior beam-to-column joints are also marked in Figure 2.1c. Seven-wire low-relaxation strand is shown in Figure 2.2. The material properties of C40/45 class concrete, B500c reinforcing steel, and seven-wire low-relaxation strand used in the design are provided in Table 2.2.

(a) 3D view

All dimensions in mm.
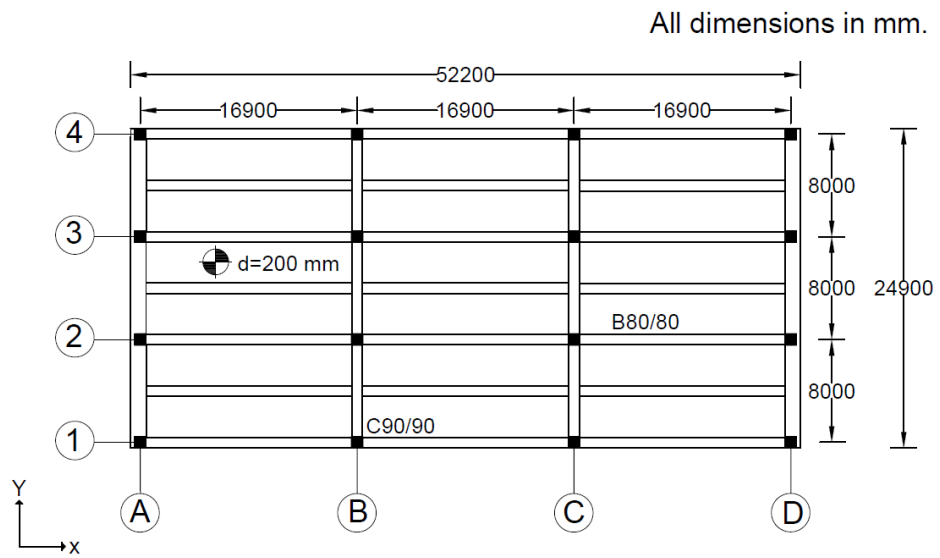
(b) Floor plan

(c) Front view

Figure 2.1. Building geometry

Figure 2.2 Seven wire low-relaxation strand

Table 2.2 Mechanical Properties of Materials

| Concrete		Reinforcing steel		Low-relaxation strand	
f_c'	40 MPa	f_y	500 MPa	f_{py}	1680 MPa
f_{ct}	2.21 MPa	f_u	625 MPa	ε_{py}	0.0084
E_c	34555 MPa	E_s	200000 MPa	f_{pu}	1860 MPa
		ε_y	0.0025	E_{ps}	200000 MPa
		ε_{sh}	0.0080		
		ε_u	0.0800		

2.2.2   Gravity Loads and Seismic Design Parameters

In the gravity design, a superimposed dead load of 300 kg/m^2 was applied to the slab to account for the loads due to coverings and partition walls. The structure was designated as an office building, therefore, a live load of 500 kg/m^2 was implemented to each floor as per the requirements of TS498. It was also assumed that the structure was located within a highly seismic region. The soil class was considered as ZB corresponding to slightly weathered medium-strength rock ground in TBEC. The response spectrum shown in Figure 2.3a was used to obtain the lateral loads using the behavior factor of 8 and overstrength factor of 3. It is noted that this pair of structural factors corresponds to a high ductile moment-resisting reinforced concrete frame building as defined in TBEC. The principle of strong column-weak beam was

followed to prevent column hinging. Accordingly, Figure 2.3b shows the location of inflection point of the beam in the prototype building. Consequently, this figure shows that zero-moment point was about 3.1 m away from the column's outer face. Similarly, the structural analyses revealed that the column inflection point occurred at nearly mid-height (1.56 m) of the floor as can be seen from Figure 2.3c. Besides, the design summary of the prototype building is given in Table 2.3. In this table, reinforcement configurations, post-tensioning strand amounts, and load-balancing ratios are provided for each specimen. Flexural moment capacities were calculated by considering the expected material strengths. According to TBEC, the characteristic compressive strength of concrete and steel strength were magnified by factors of 1.3 and 1.2, respectively.
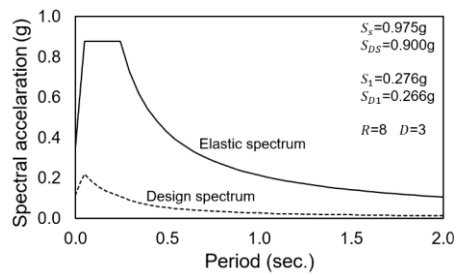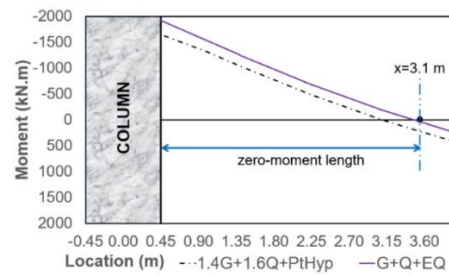
(a) Response spectrum (b) Beam inflection point
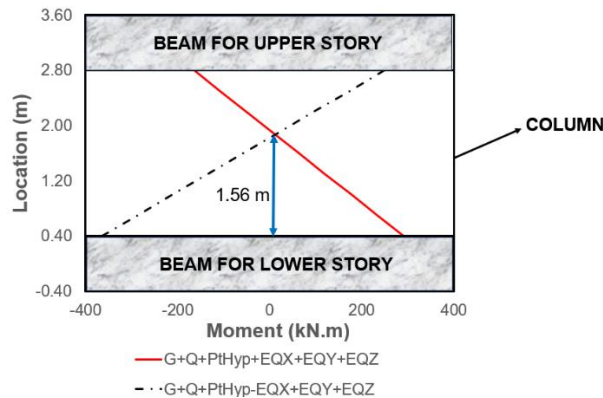
(c) Column inflection point

Figure 2.3. Technical information about the prototype building

23

Table 2.3 Design Summary for Prototype Building

Specimen label	ρ,ρ'	Longitudinal reinforcement for beam	Post-tensioning strand	Load-balancing ratio	M_{cr} (kN.m) top/bottom	M_r (kN.m) top/bottom	Longitudinal reinforcement for column
PTE-3-50	0.003	2×4φ24	8×150 mm²	50%	1298/664	2840/1750	12-φ36
PTE-4-50	0.004	2×4φ28	8×150 mm²	50%	1298/664	3053/2079	12-φ36
PTE-3-75	0.003	2×4φ24	12×150 mm²	75%	1298/664	3460/1950	12-φ36
PTI-4-50	0.004	2×4φ28	8×150 mm²	50%	1298/664	3053/2079	12-φ36
RC-10-NA	0.010	2×4φ44	N/A	N/A	1004/513	4027/3015	12-φ36

2.2.3 Selection of Tendon Geometry

In practice, tendons are commonly prestressed from both ends to reduce friction loss in spans exceeding 40 m. Therefore, an optimal tendon profile is achieved with the help of required prestress level to balance a portion of the dead loads. It is also known that parabolic tendon layout helps to increase the shear capacity. The reasoning behind parabolic tendon geometry (see Figure 2.4) used in the prototype building can be clarified as follows: The tendon passes through the center of gravity of concrete section (c.g.c) within the beam-to-column joints to prevent eccentricity at exterior supports. Consequently, secondary moments developing due to eccentricity are eliminated. Moreover, tendon is located close to the bottom face of the beam at the mid-span to increase the moment arm, thereby improving flexural moment capacity of the section.
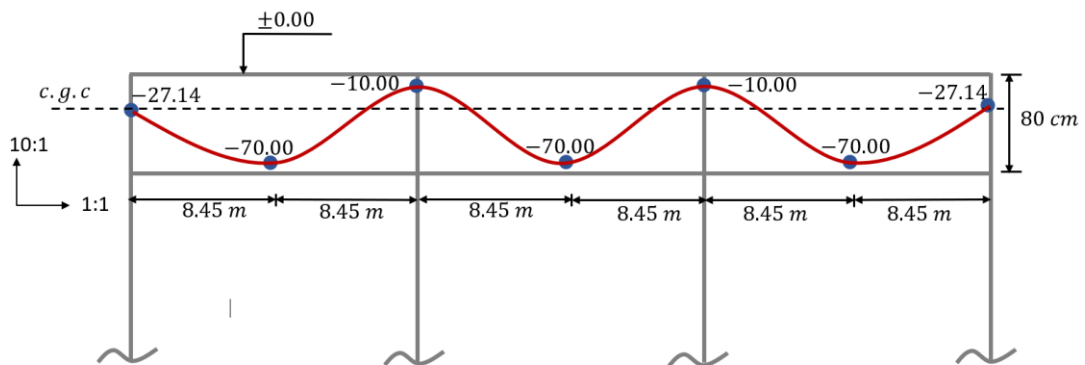

Figure 2.4. Tendon geometry for prototype building

The load-balancing principle establishes a relation between the balanced distributed load and the applied prestressing force for parabolic tendons. Accordingly, it is assumed that prestressing force remains constant along the tendon length. Also, this approach decouples the effects of bending and axial forces in a member. In Figure 2.5, a simple sketch is illustrated to derive the mathematical expressions given in Equation 2.1. In this figure, while point C corresponds to the lowest point on the tendon, the centerlines of left and right supports are denoted as A and B, respectively.
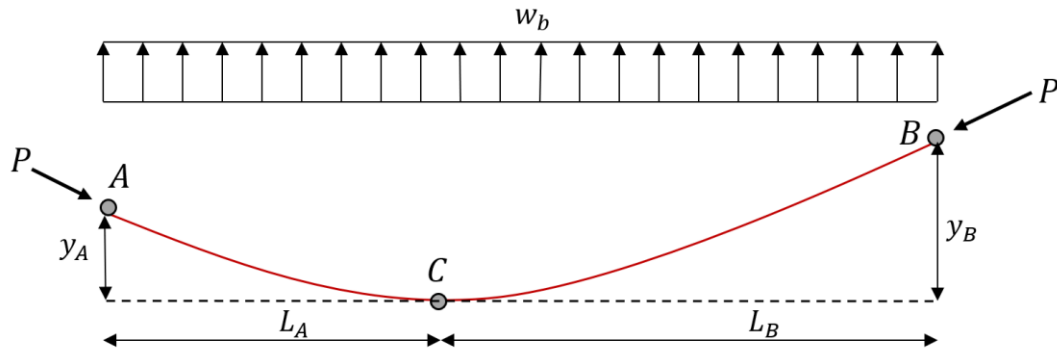
Figure 2.5. Load-balancing ratio calculation

$$w_b = \frac{2Py_A}{(L_A)^2} \qquad L_A = L_T \frac{\sqrt{\frac{y_A}{y_B}}}{1+\sqrt{\frac{y_A}{y_B}}} \qquad (2\text{-}1)$$

where:

P is the prestressing force,

w_b is the balanced distributed load,

L_A is the horizontal distance component of curve AC,

y_A is the tendon elevation at point A,

L_B is the horizontal distance component of curve BC,

y_B is the tendon elevation at point B,

L_T is the total length of tendon span.

The computations showed that the cumulative stress loss comprising immediate losses (i.e., elastic shortening of the concrete, anchorage losses, and frictional losses) and time-dependent losses (such as creep, shrinkage, and steel relaxation) was about 20% of initial prestress (f_{pi}). Additionally, the jacking force applied on the tendons was approximately 80% of strand's yield strength (f_{py}). This situation necessitated a prestressing steel area of 1200 mm^2 corresponding to eight sets of seven-wire low-

relaxation strand with a nominal diameter of 15.7 mm. Also, an effective prestress (f_{pe}) of approximately 1100 MPa was imposed on the tendons.

Figure 2.6 represents the flanged beam section. In this figure, c.g.s refers to the center of gravity of prestressing steel. Accordingly, the vertical distance $\bar{y}$, measured from the bottom face of the concrete section, is approximately 529 mm. The effective flange width (b_{eff}) was obtained according to the provisions of TS500 and ACI 318. The requirements for both design codes are summarized in Table 2.4. In this table, b_w and h correspond to the beam width and beam height, respectively. While l_n indicates the clear span length, l_p stands for plastic hinge length. The clear distance between adjacent webs is represented by s_w.
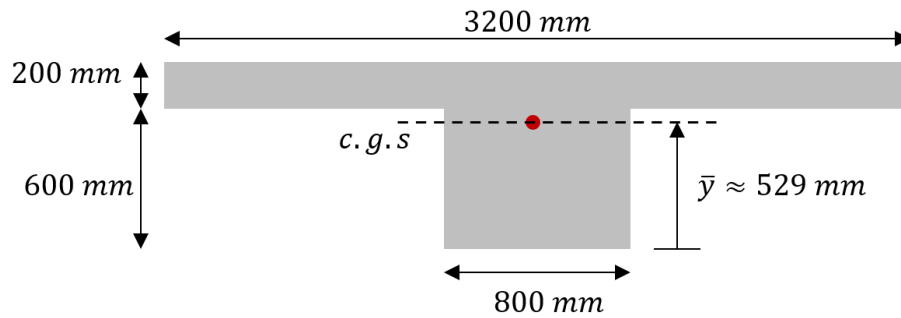

Figure 2.6. The cross-sectional dimensions of T-shaped beam

Table 2.4 Effective Flange Width Calculation

Design standard	b_{eff}
ACI 318	$\min\left\{b_w + 16h, b_w + s_w, b_w + \dfrac{l_n}{4}\right\}$
TS500	$b_w + 0.2l_p$

2.2.4   Serviceability Design

The design aims to ensure that tensile and compressive stresses in the concrete section do not exceed the allowable limits specified by relevant design codes. Stress

values caused by the service loads are computed at the top and bottom fibers of the concrete section for both support and mid-span locations. They are evaluated in two load conditions: (i) Immediately after transfer of prestress. (ii) After the occurrence of long-term losses. Stress readings were checked in accordance with the limit states of TS3233 as demonstrated in Table 2.5. In this table, while f_{ci}' implies compressive strength of concrete at the time of initial prestressing, f_c' indicates the characteristic compressive strength of concrete at the end of 28 days. For design purposes, it is noted that the ratio of f_{ci}' to f_c' can be approximately taken as 0.75.

Table 2.5 Allowable Stress Limits for Prestressed Concrete

Load condition	Tensile stress	Compressive stress
Transfer	$0.25(f_{ci}')^{1/2}$	$0.55 f_{ci}'$
Total	$0.50(f_c')^{1/2}$	$0.45 f_c'$

2.3 Test Specimens

A total of five specimens were tested during the experimental program. A systematic nomenclature is prepared to reflect their specific attributes. Accordingly, the first component of each label indicates the specimen type, distinguishing between post-tensioned and conventionally reinforced concrete specimens. For instance, specimens reinforced solely with mild steel were labeled "RC," while post-tensioned specimens were identified as "PTE" and "PTI" for exterior and interior types, respectively. The second character in each label corresponds to the longitudinal reinforcement ratio. To give an example, "3" refers to a 0.3% tensile mild steel ratio. The third letter introduces the load-balancing ratio for gravity loads; for example, "50" signifies a 50% load-balancing ratio.

This study's primary test variables were the mild steel ratio, the load-balancing ratio, and the specimen location. To evaluate the effect of mild steel ratio on seismic performance, specimens labeled PTE-3-50 and PTE-4-50 were analyzed.

Comparisons between PTE-3-50 and PTE-3-75 enabled assessment of the impact of variations in load-balancing ratio on structural behavior. Additionally, the influence of location type (i.e., exterior, interior) was examined by comparing the performance of PTE-4-50 and PTI-4-50 specimens. The specimen RC-10-NA, reinforced with mild steel only, was designated as a control specimen.

2.3.1 Frame Geometry

As discussed in previous sections, 1:2 scaled test specimens were constructed due to physical limitations of the laboratory environment. Consequently, the structural element dimensions of the prototype building were proportionally reduced. Accordingly, 45 cm × 45 cm column, 40 cm × 40 cm beam, and 10 cm thick slab were used in all beam-to-column joint tests. The geometric configurations of exterior and interior specimens are presented in Figure 2.7 and Figure 2.8, respectively.
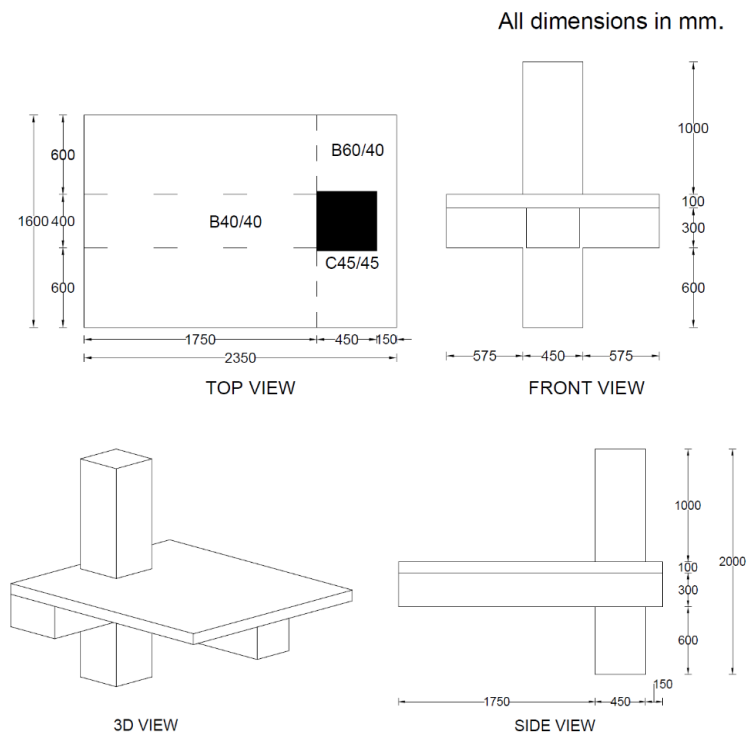
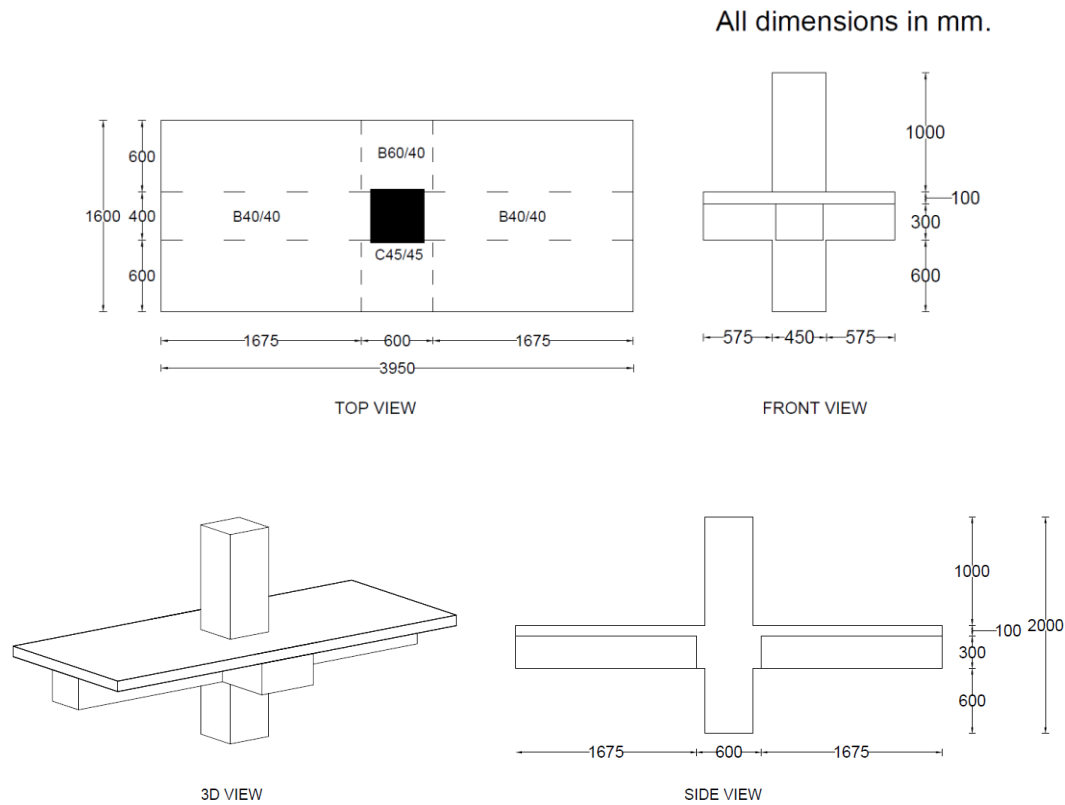

Figure 2.7. Exterior test specimen geometry

Figure 2.8. Interior test specimen geometry

2.3.2 Material Properties

The mechanical properties of concrete, reinforcing steel, post-tensioning strands, and mesh reinforcements were determined in the Materials of Construction Laboratory at Middle East Technical University.

2.3.2.1 Concrete

All specimens were constructed using C40/45 class concrete having a 28-day target characteristic compressive strength of 40 MPa. Twenty-four cylindrical samples with the standard sizes of 150 mm × 300 mm were prepared immediately after concrete casting. Each sample was compacted using a tamping rod. Then, eight test

samples were arbitrarily selected and they were removed from their steel molds at the end of 28 days. Sulfur powder was applied to cap the top and bottom faces of the specimens, ensuring smooth surfaces. Finally, they were tested using the compression machine. All these stages are illustrated in Figure 2.9. Additionally, the measured strengths are summarized in Table 2.6. Accordingly, the average concrete compressive strength at 28 days was 38.1 MPa.

Figure 2.9. Concrete compression test

Table 2.6 Uniaxial Compressive Strength of Concrete at 28 Days

Sample number	$f_{c,i}'$ (MPa)
1	39.9
2	36.6
3	35.7
4	35.3
5	36.7
6	35.1
7	44.3
8	40.9

The procedure explained above was also conducted by taking three samples from each test specimen after the completion of the relevant experiment. The uniaxial compressive strength test results for these samples are presented in Table 2.7. Besides, the components of concrete mix design are provided in Table 2.8.

Table 2.7 Uniaxial Compressive Strength of Concrete for Test Specimens

Specimen label	Sample #1 f_c' (MPa)	Sample #2 f_c' (MPa)	Sample #3 f_c' (MPa)	Average $f_{c,ave}'$ (MPa)
PTE-3-50	40.6	49.8	41.5	44.0
PTE-4-50	35.1	44.3	40.9	40.1
PTE-3-75	52.3	44.2	44.9	47.1
PTI-4-50	46.9	43.7	42.9	44.2
RC-10-NA	53.8	43.4	48.9	48.7

Table 2.8 Concrete Mix Design Elements per m^3

Water (kg)	Cement (kg)	Water/cement ratio	Sand (kg)	Aggregate (kg) Size (4-11 mm)	Size (11-22 mm)
160	280	0.57	1005	236	633

2.3.2.2   Reinforcing Steel

B500c class mild steel was used for beams and columns. Also, B500a class mesh reinforcement (Q188/188 type) with a diameter of 6 mm and a spacing of 150 mm in longitudinal and transverse directions was employed for the slabs. The available rebar diameters applied for beams and columns were 10 mm, 12 mm, 14 mm, 18

mm, and 22 mm. Mechanical properties summarized in Table 2.9 were obtained through the direct tension tests implemented on several samples in the laboratory (see Figure 2.10). As a result, typical uniaxial stress-strain curves for both mild steel and mesh reinforcement are given in Figure 2.11.

Table 2.9 Test Results for Mild Steel and Mesh Reinforcement

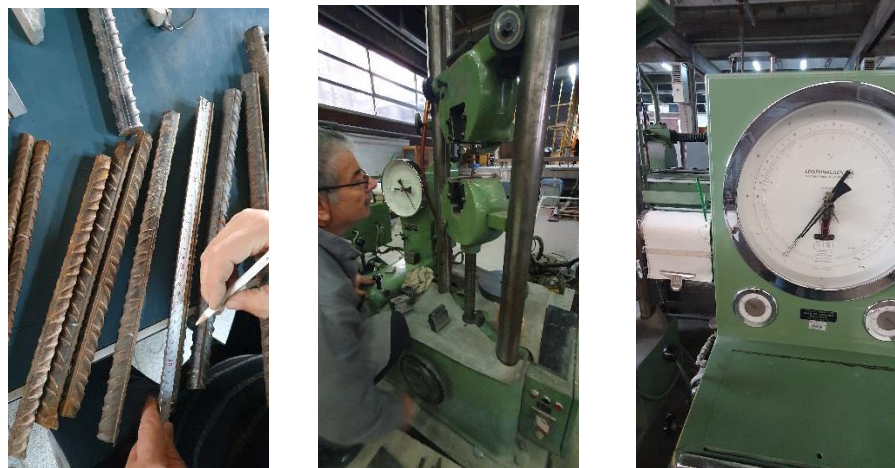| Steel class	Rebar size	ε_y (mm/mm)	ε_u (mm/mm)	f_y (MPa)	f_u (MPa)
B500c	ϕ10	0.00281	0.16222	562.5	701.6
	ϕ12	0.00278	0.14667	556.6	692.5
	ϕ14	0.00278	0.20000	555.5	678.7
	ϕ18	0.00276	0.20333	552.6	645.1
	ϕ22	0.00276	0.18833	552.7	673.1
B500a	ϕ6	0.00288	0.10000	576.0	631.5

Figure 2.10. Direct tension tests for mild steel and mesh reinforcement

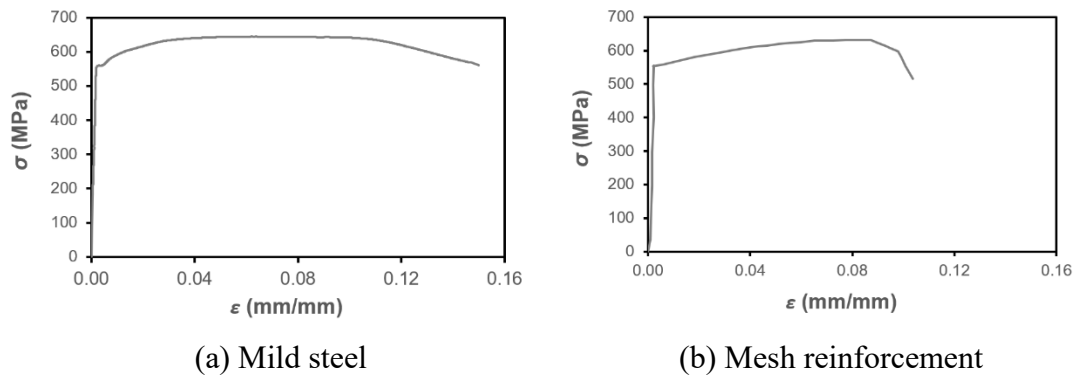(a) Mild steel   (b) Mesh reinforcement

Figure 2.11. Stress-strain characteristics for mild steel and mesh reinforcement

2.3.2.3   Prestressing Steel

Seven-wire low relaxation strands with a nominal diameter of 15.7 mm were used for each post-tensioned specimen. Four strand samples were subjected to the direct tension tests in the laboratory (see Figure 2.12). As can be followed from Table 2.10, the average rupture strength was measured as 1860 MPa. Consequently, the uniaxial stress-strain relation is exhibited in Figure 2.13.

Figure 2.12. Direct tension tests for prestressing steel

Table 2.10 Test Results for Prestressing Steel

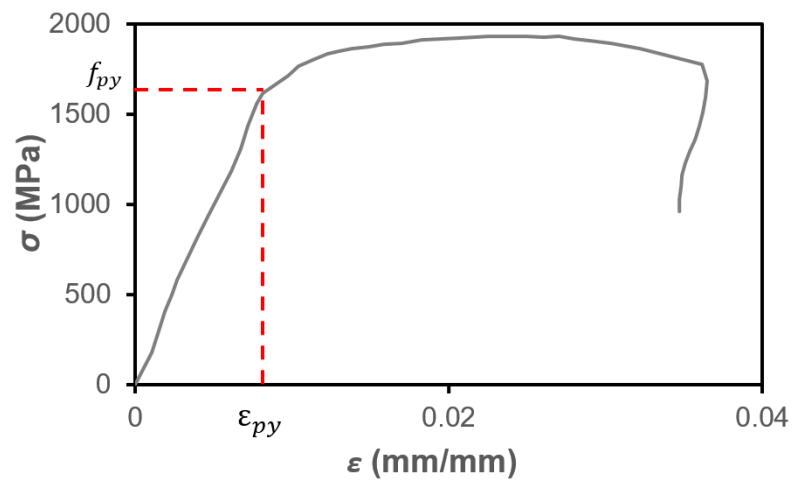| Sample number	f_{pu} (MPa)
1	1887.4
2	1907.1
3	1852.5
4	1789.3

Figure 2.13. Stress-strain curve for prestressing steel

2.3.3 Specimen Preparation

Firstly, the mild steel reinforcement assemblies and post-tensioning strands were appropriately placed within the plywood formworks. Secondly, concrete was casted. After the curing process, effective prestressing of approximately 1100 MPa was imposed on tendon groups at the end of 28 days using a hydraulic jack attached to one end of the strands. An epoxy-based cementitious grouting was also performed on the post-tensioning strands to improve bonding between tendons and surrounding reinforced concrete. Finally, the test instruments and related equipments were installed on the test specimens to commence the experiments. A summary explaining

the properties of test specimens is provided in Table 2.11. Additionally, their material characteristics are demonstrated in Table 2.12. Construction photos and technical drawings for each specimen are presented from Figure 2.14 to Figure 2.23.

Table 2.11 Reinforcement Layouts for Test Specimens

Specimen label	ρ, ρ'	Longitudinal reinforcement for beam	Post - tensioning strand	Load-balancing ratio	Slab reinforcement	Longitudinal reinforcement for column
PTE-3-50	0.003	2×4ϕ12	2×150 mm^2	50%	2×Q188/188	12-ϕ18
PTE-4-50	0.004	2×4ϕ14	2×150 mm^2	50%	2×Q188/188	12-ϕ18
PTE-3-75	0.003	2×4ϕ12	3×150 mm^2	75%	2×Q188/188	12-ϕ18
PTI-4-50	0.004	2×4ϕ14	2×150 mm^2	50%	2×Q188/188	12-ϕ18
RC-10-NA	0.010	2×4ϕ22	N/A	N/A	2×Q188/188	12-ϕ18

Table 2.12 Material Properties for Test Specimens

| Sample number | Concrete f'_c (MPa) | Longitudinal/transverse reinforcement for beam | | | | Mesh reinforcement for slab | | | | Post-tensioning strand |
		f_y (MPa)	f_u (MPa)	ε_y mm/mm	ε_u mm/mm	f_y (MPa)	f_u (MPa)	ε_y mm/mm	ε_u mm/mm	f_{pu} (MPa)
PTE-3-50	44	557	692	0.0028	0.1467	576	631	0.0029	0.1000	1887
PTE-4-50	40	555	679	0.0028	0.2000	576	631	0.0029	0.1000	1907
PTE-3-75	47	557	692	0.0028	0.1467	576	631	0.0029	0.1000	1853
PTI-4-50	45	555	679	0.0028	0.2000	576	631	0.0029	0.1000	1789
RC-10-NA	49	553	673	0.0028	0.1883	576	631	0.0029	0.1000	N/A
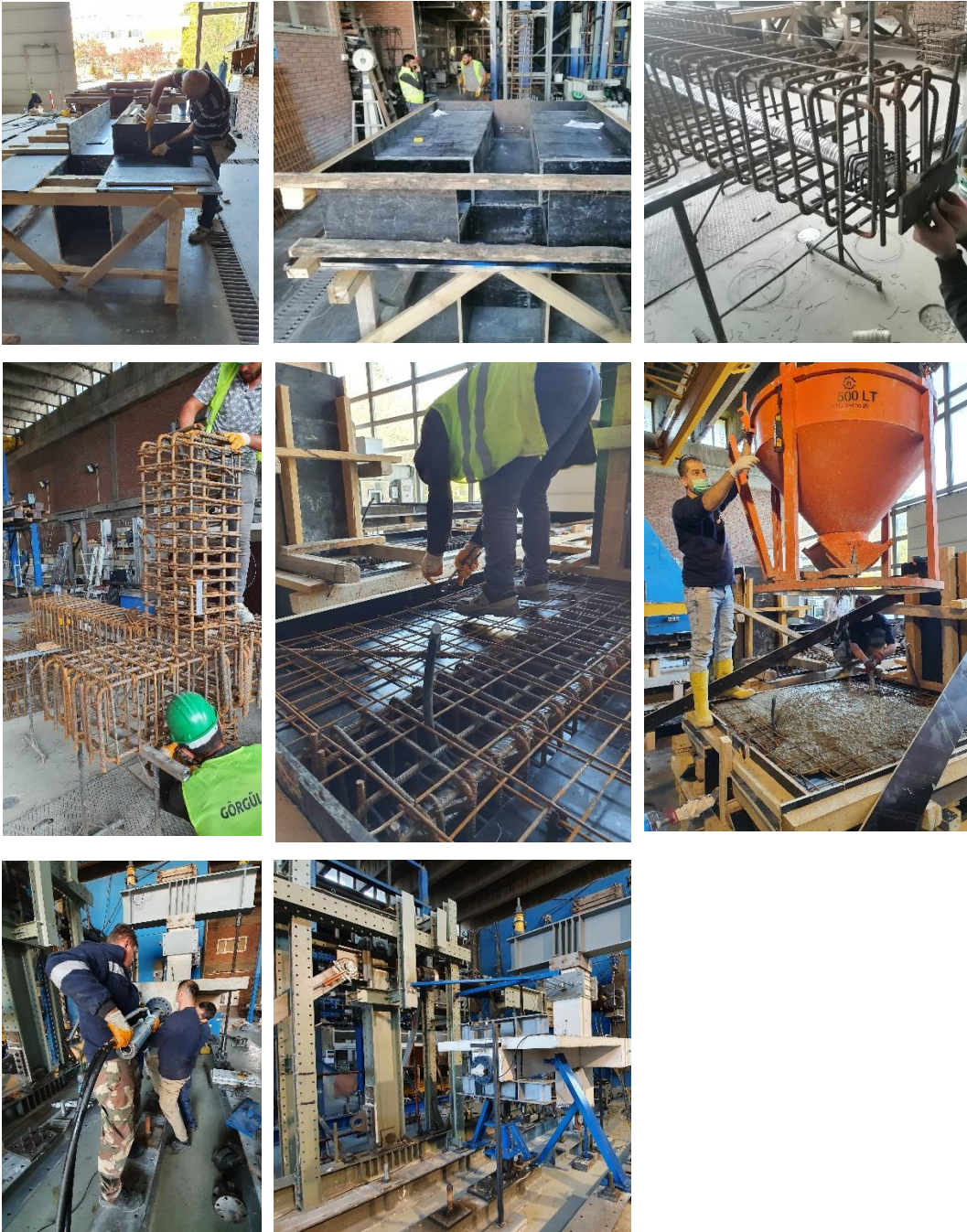
Figure 2.14. Construction stages for PTE-3-50

Column
(45 cm x 45 cm)
12Φ18

Φ12 / 80 mm stirrup

Φ12 / 80 mm tie-bar

Beam
(40 cm x 40 cm)
2 x 4Φ12

Φ12 / 80 mm stirrup

Beam
(60 cm x 40 cm)
2 x 6Φ16

Φ10 / 100 mm stirrup
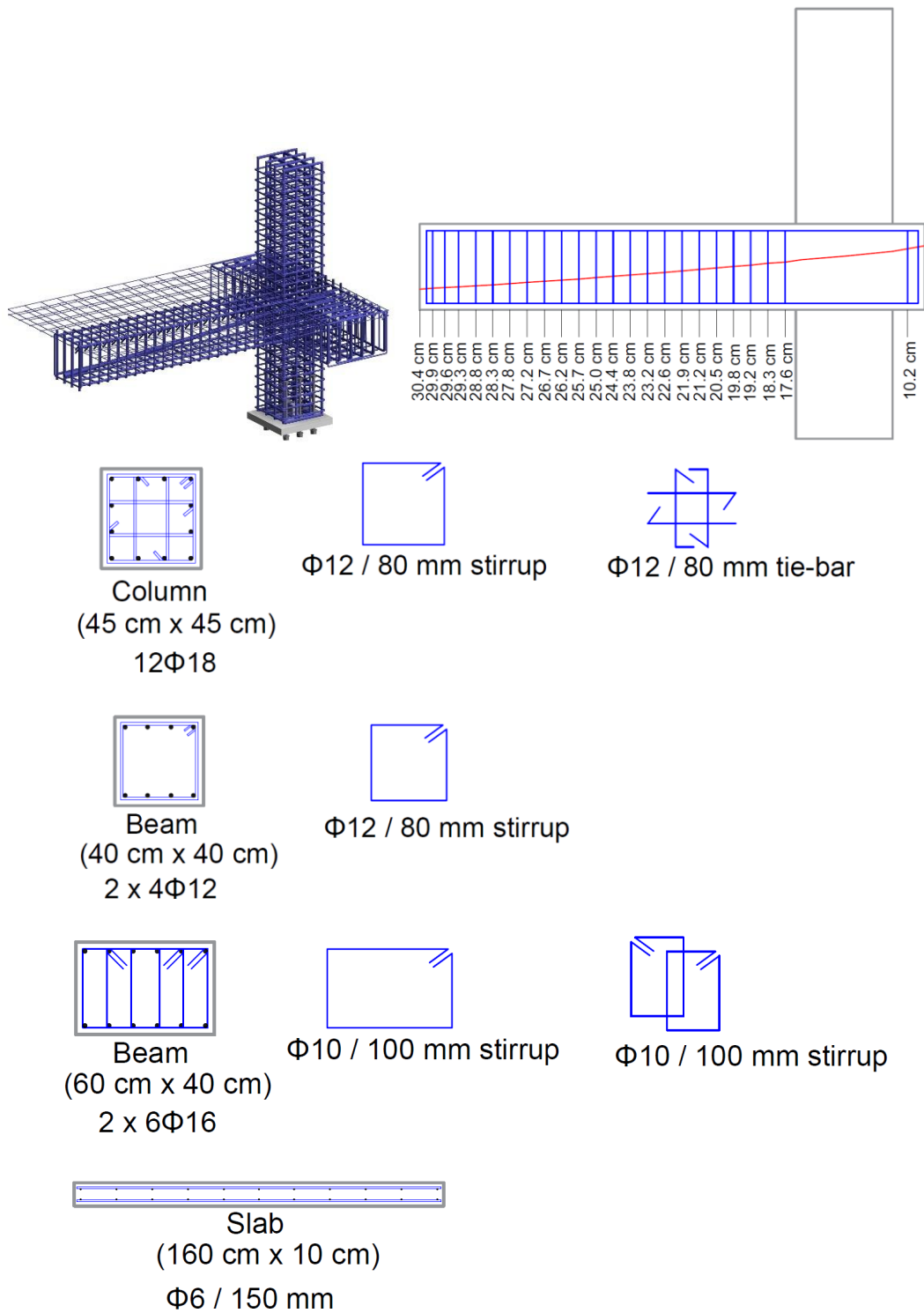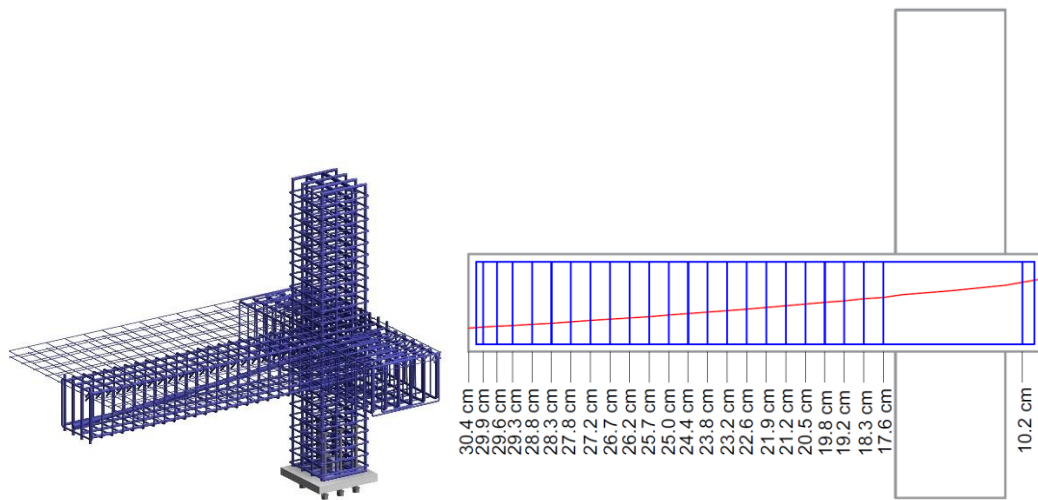
Φ10 / 100 mm stirrup

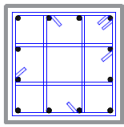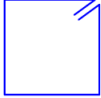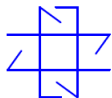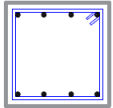Slab
(160 cm x 10 cm)
Φ6 / 150 mm

Figure 2.15. Reinforcement drawings for PTE-3-50

Figure 2.16. Construction stages for PTE-4-50

30.4 cm
29.9 cm
29.6 cm
29.3 cm
28.8 cm
28.3 cm
27.8 cm
27.2 cm
26.7 cm
26.2 cm
25.7 cm
25.0 cm
24.4 cm
23.8 cm
23.2 cm
22.6 cm
21.9 cm
21.2 cm
20.5 cm
19.8 cm
19.2 cm
18.3 cm
17.6 cm

10.2 cm

Column
(45 cm x 45 cm)
12Φ18

Φ12 / 80 mm stirrup
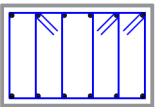
Φ12 / 80 mm tie-bar

Beam
(40 cm x 40 cm)
2 x 4Φ14
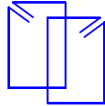
Φ12 / 80 mm stirrup

Beam
(60 cm x 40 cm)
2 x 6Φ16

Φ10 / 100 mm stirrup

Φ10 / 100 mm stirrup

Slab
(160 cm x 10 cm)
Φ6 / 150 mm

Figure 2.17. Reinforcement drawings for PTE-4-50

41

Figure 2.18. Construction stages for PTE-3-75

30.4 cm
29.9 cm
29.6 cm
29.3 cm
28.8 cm
28.3 cm
27.8 cm
27.2 cm
26.7 cm
26.2 cm
25.7 cm
25.0 cm
24.4 cm
23.8 cm
23.2 cm
22.6 cm
21.9 cm
21.2 cm
20.5 cm
19.8 cm
19.2 cm
18.3 cm
17.6 cm

10.2 cm

Column
(45 cm x 45 cm)
12Φ18

Φ12 / 80 mm stirrup

Φ12 / 80 mm tie-bar

Beam
(40 cm x 40 cm)
2 x 4Φ12

Φ12 / 80 mm stirrup

Beam
(60 cm x 40 cm)
2 x 6Φ16

Φ10 / 100 mm stirrup

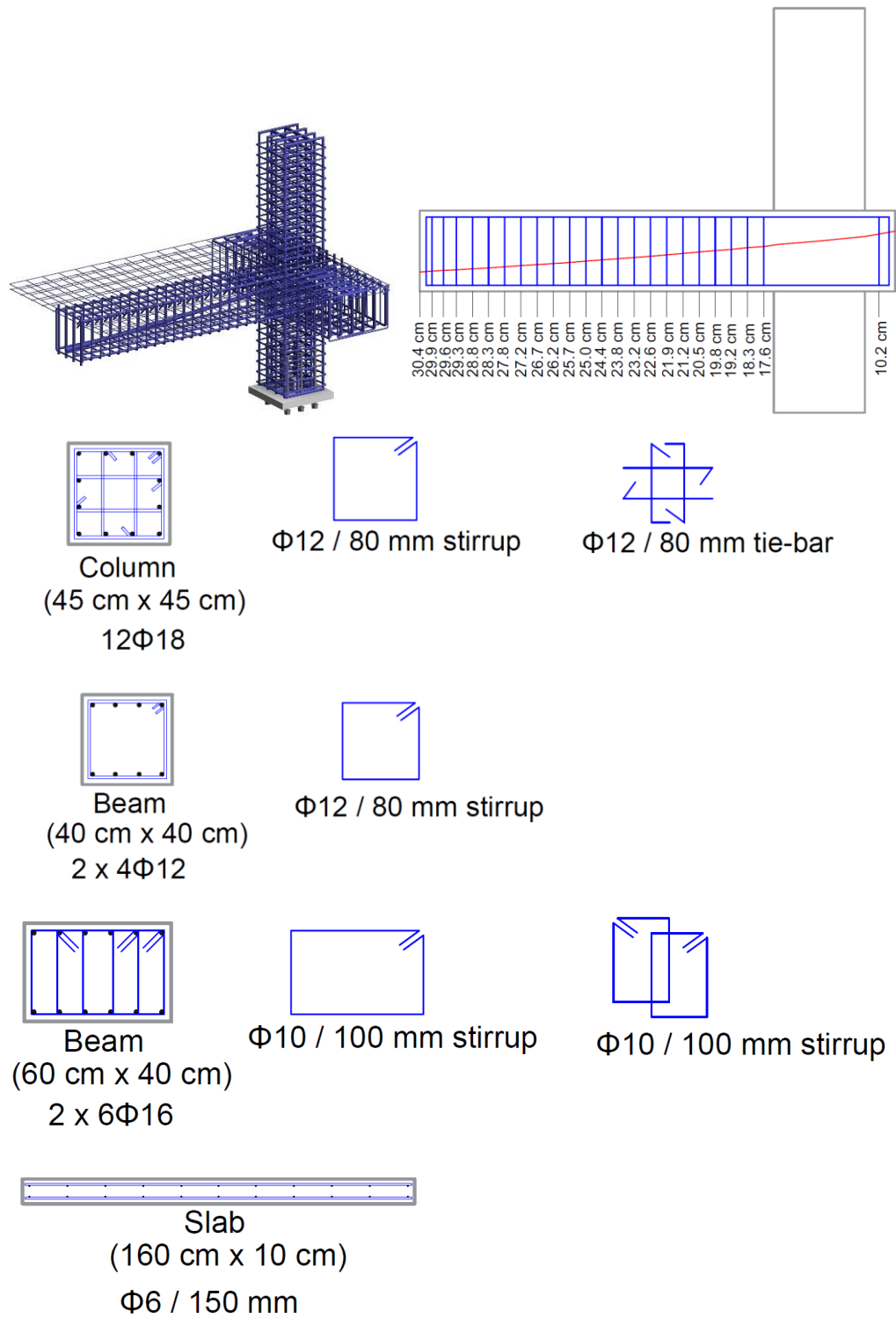Φ10 / 100 mm stirrup

Slab
(160 cm x 10 cm)
Φ6 / 150 mm

Figure 2.19. Reinforcement drawings for PTE-3-75

Figure 2.20. Construction stages for PTI-4-50

Φ12 / 80 mm stirrup   Φ12 / 80 mm tie-bar

Column
(45 cm x 45 cm)
12Φ18

Φ12 / 80 mm stirrup

Beam
(40 cm x 40 cm)
2 x 4Φ14

Beam
(60 cm x 40 cm)
2 x 6Φ16

Φ10 / 100 mm stirrup   Φ10 / 100 mm stirrup
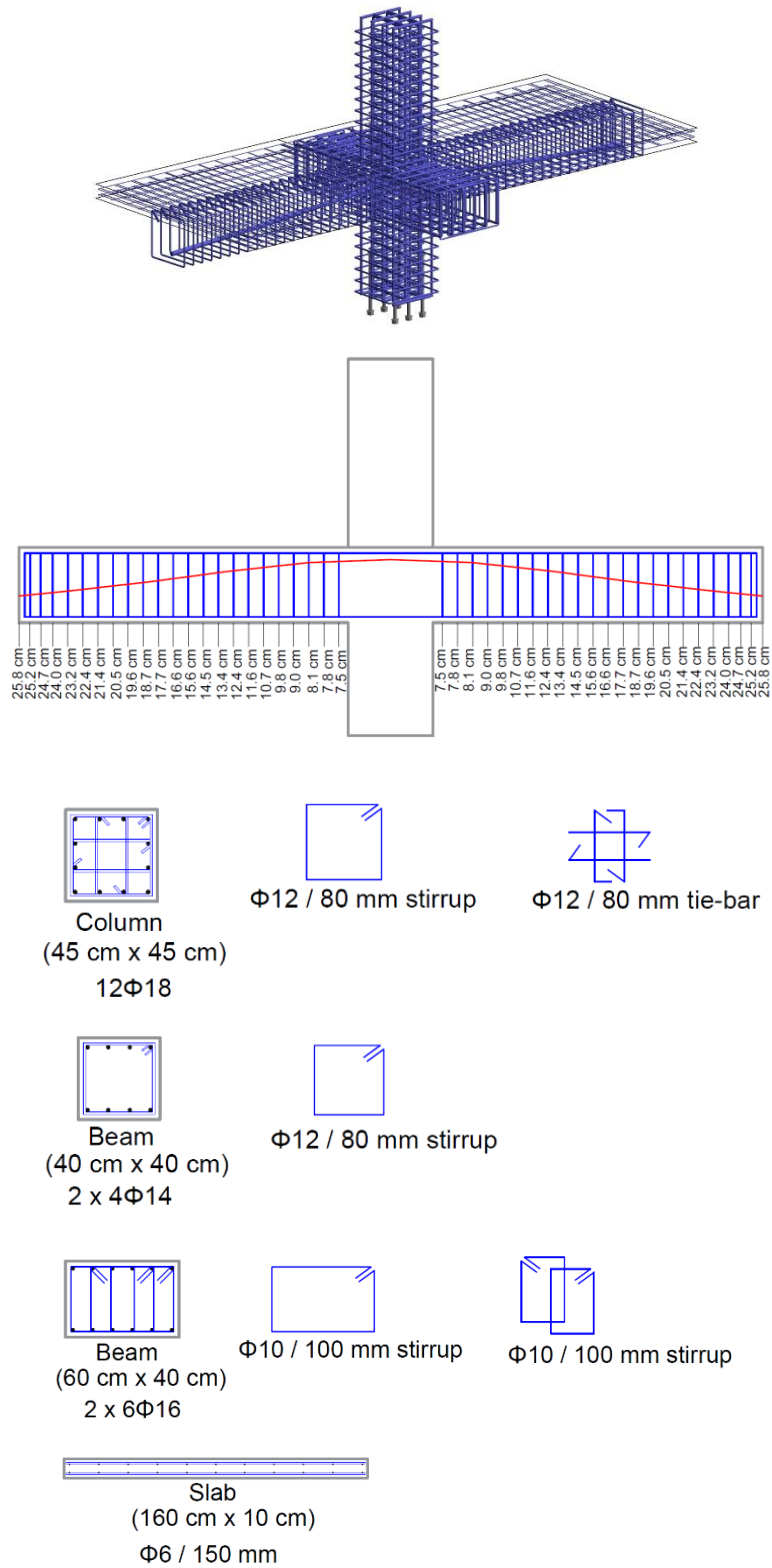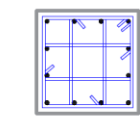
Slab
(160 cm x 10 cm)
Φ6 / 150 mm
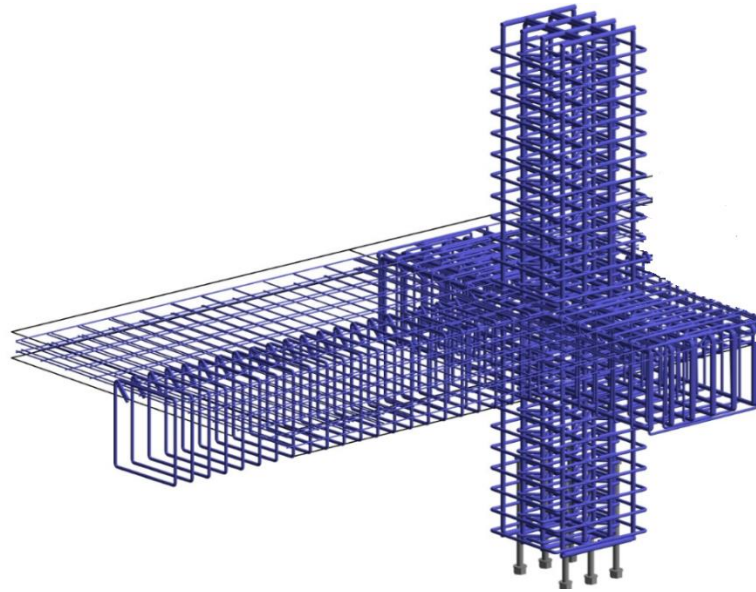
Figure 2.21. Reinforcement drawings for PTI-4-50
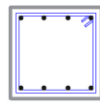
Figure 2.22. Construction stages for RC-10-NA

Column
(45 cm x 45 cm)
12Φ18

Φ12 / 80 mm stirrup

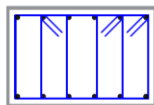Φ12 / 80 mm tie-bar

Beam
(40 cm x 40 cm)
2 x 4Φ22

Φ12 / 80 mm stirrup

Beam
(60 cm x 40 cm)
2 x 6Φ16

Φ10 / 100 mm stirrup

Φ10 / 100 mm stirrup

Slab
(160 cm x 10 cm)
Φ6 / 150 mm

Figure 2.23. Reinforcement drawings for RC-10-NA

2.4   Test Setup and Instrumentation

The test setup comprised a reaction wall, loading apparatus, and instrumentation. It was anchored to the strong floor using high-strength steel rods. Furthermore, lateral supports were installed on both faces of the beam to prevent out-of-plane deformation and enhance the system stability. The specimen was restrained by a roller support at the beam's free end and a hinge at the column's base. It should be emphasized that these locations correspond to the inflection points of the prototype structure.

An axial load was applied to the column through two vertical hydraulic jacks, each with a 100-ton capacity, mounted on a steel I-beam. A lateral load was performed by a horizontal hydraulic jack with a 50-ton capacity, positioned at the top of the column and anchored to the strong wall. Additionally, an initial prestressing force was imposed on the tendons using another hydraulic jack with a 100-ton capacity. All applied forces were continuously tracked through load cells during the experiments. In light of these explanations, the experimental setups for exterior and interior test joints are exhibited in Figure 2.24.

The schematic layouts of test instruments such as Linear Variable Differential Transformers (LVDT), load cells (LC), tiltmeters, and strain gauges are illustrated in Figure 2.25. Accordingly, four load cells, twenty-nine LVDTs, three tiltmeters, and two strain gauges were employed during the tests. Three LVDTs mounted on a steel plate attached to the column were used to measure the horizontal displacement at the column tip. Bar slip rotation was recorded with the help of two and four LVDTs placed 50 mm away from the beam-to-column joint face for exterior and interior specimens, respectively. Bar slip rotations are observed at the interfaces of beam-to-column or column-to-foundation connections, primarily caused by significant crack openings. The upward elongation of the column longitudinal reinforcement from the foundation induces substantial rotations, as detailed in the studies conducted by Ozcan et al. (2008), Sezen and Moehle (2003), and Elwood and Moehle (2003). To effectively monitor these deformations, LVDTs are strategically positioned near the

beam-to-column interface. Moreover, the plastic hinge length was estimated using the equation proposed by Priestley and Park (1987) (see Section 3.2 for details). Accordingly, four and eight LVDTs positioned 250 mm away from this reference point were used for exterior and interior joints, respectively. Consequently, a detailed summary of the test instrumentation is provided in Table 2.13. Furthermore, the exact locations of some major LVDTs are presented in Figure 2.26.
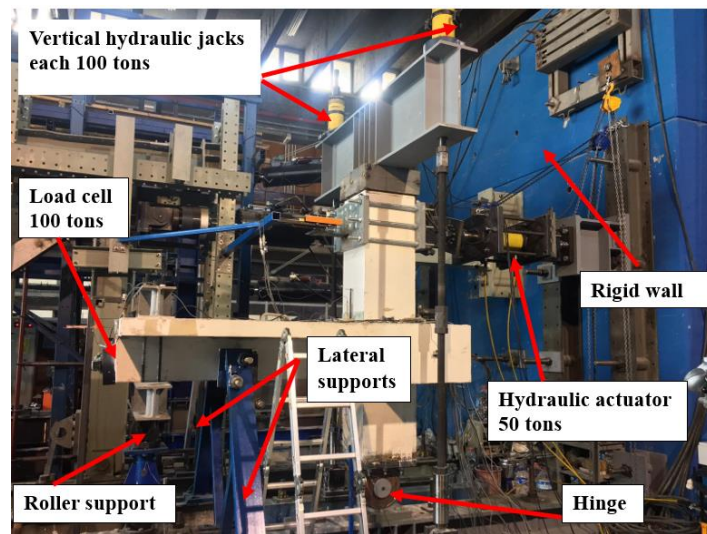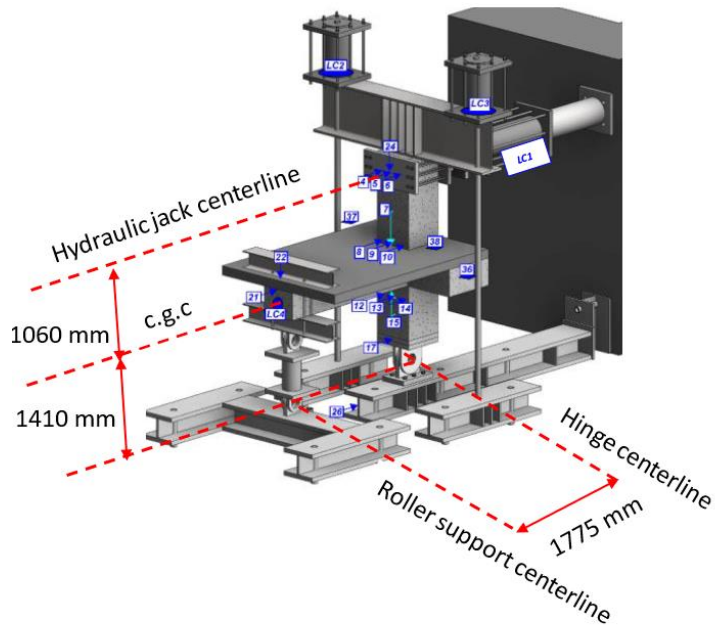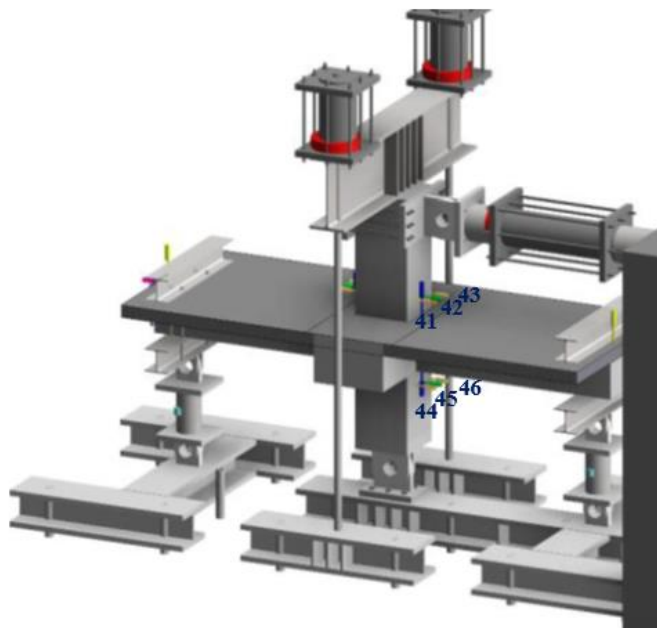

(a) Exterior test specimen
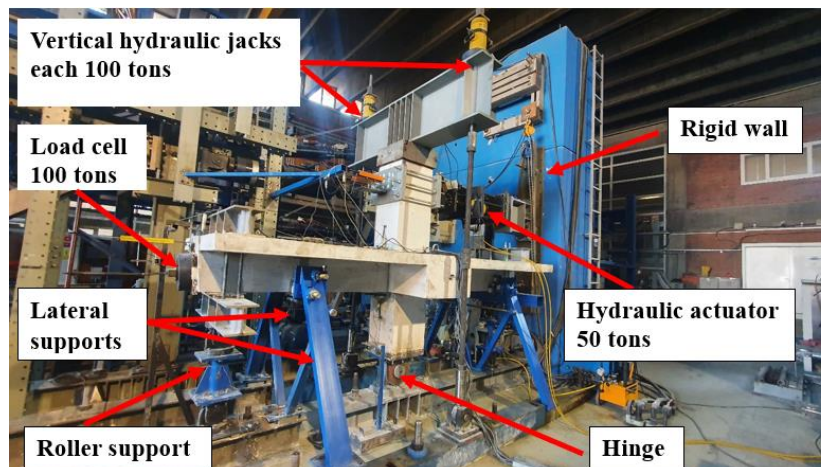
(b) Interior test specimen

Figure 2.24. Experimental setup for exterior and interior joints

(a) Exterior test specimen

(a) Interior test specimen

Figure 2.25. Test instruments for exterior and interior joints

The test was initiated by applying an axial load of 850 kN on the column, representing approximately 10% of the column's capacity as calculated for the prototype building. This load was kept constant during the experiment. Subsequently, a lateral loading protocol was carried out, whereby the specimen was subjected to progressively increasing horizontal drifts via a hydraulic jack under a reversible quasi-static displacement-controlled mechanism. Each drift consisted of two cycles in push and pull directions as recommended by FEMA 461. As a result, the displacement history is introduced in Figure 2.27. It is also important to note that the dynamic effects were not taken into account throughout the tests.

Table 2.13 Test Instruments

Number	Category	Position	Function	Capacity	Unit
LC1	Load cell	Horizontal	Lateral load	500	kN
LC2	Load cell	Vertical	Transverse load	1000	kN
LC3	Load cell	Vertical	Transverse load	1000	kN
LC4	Load cell	Horizontal	Lateral load	1000	kN
4	LVDT	Horizontal	Lateral tip deflection	200	mm
5	LVDT	Horizontal	Lateral tip deflection	200	mm
6	LVDT	Horizontal	Lateral tip deflection	200	mm
7	LVDT	Vertical	Column curvature	50	mm
8	LVDT	Horizontal	Beam curvature	50	mm
9	LVDT	Horizontal	Bar slip	50	mm
10	LVDT	Horizontal	Beam curvature	50	mm
11	LVDT	Vertical	Column curvature	50	mm
12	LVDT	Horizontal	Beam curvature	50	mm
13	LVDT	Horizontal	Bar slip	50	mm
14	LVDT	Horizontal	Beam curvature	50	mm
15	LVDT	Vertical	Column curvature	50	mm
16	LVDT	Vertical	Column curvature	50	mm
17	LVDT	Horizontal	Base plate movement	30	mm

Table 2.13 (cont'd)

21	LVDT	Horizontal	Lateral tip deflection	100	mm
22	LVDT	Vertical	Vertical tip deflection	50	mm
23	LVDT	Horizontal	Lateral tip deflection	100	mm
24	LVDT	Vertical	Steel plate deflection	50	mm
25	LVDT	Vertical	Vertical tip deflection	50	mm
26	LVDT	Horizontal	Steel beam movement	20	mm
27	Strain gauge	-	Support reaction force	-	mm/mm
28	Strain gauge	-	Support reaction force	-	mm/mm
36	Tiltmeter	Rotation	Beam rotation with respect to the ground	2π	radian
37	Tiltmeter	Rotation	Beam rotation with respect to the ground	2π	radian
38	Tiltmeter	Rotation	Beam rotation with respect to the ground	2π	radian
41[*]	LVDT	Horizontal	Beam curvature	50	mm
42[*]	LVDT	Horizontal	Bar slip	50	mm
43[*]	LVDT	Horizontal	Beam curvature	50	mm
44[*]	LVDT	Horizontal	Beam curvature	50	mm
45[*]	LVDT	Horizontal	Bar slip	50	mm
46[*]	LVDT	Horizontal	Beam curvature	50	mm

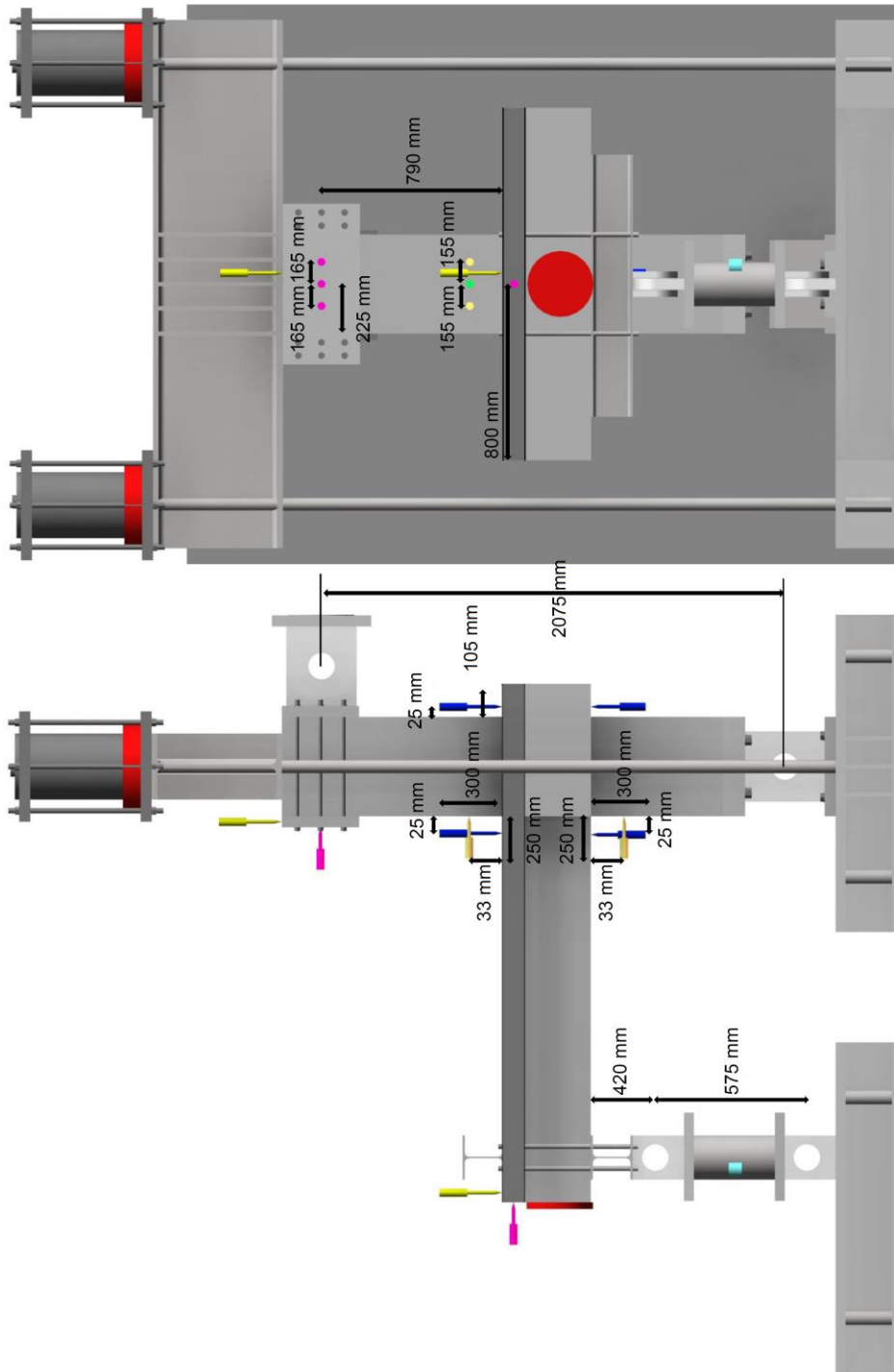[*] Related instruments were used only for interior test joints.

Figure 2.26 Location of the major instruments (a) side view, (b) front view
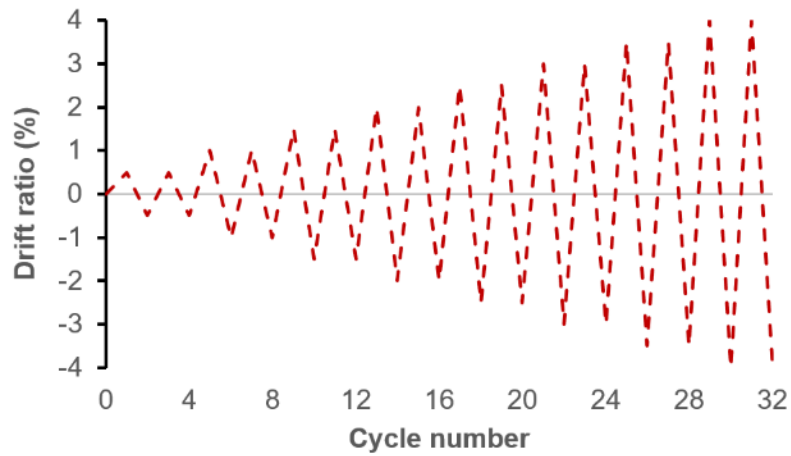
53

Figure 2.27. Displacement history

Moreover, the deformed shapes of exterior and interior test specimens are depicted in Figure 2.28. Based on this configuration, support reactions were determined and the deformations were measured by means of relevant LVDTs. In addition to the LVDT and tiltmeter photos presented in Figure 2.29, other instruments used in the experiments are shown in Figure 2.30.
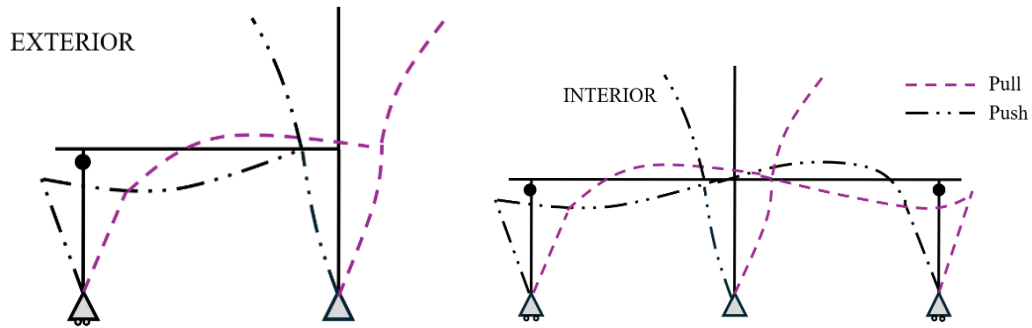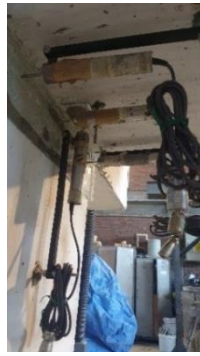

Figure 2.28. Deformed shapes for exterior and interior test beams

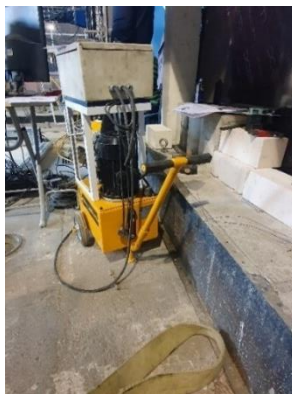(a) 7,8,9,10   (b) 12,13,14,15   (c) 4,5,6,24

(d) 23,25   (e) 36   (f) 21,22

Figure 2.29. Photos of some instruments

(a) Load pump for transverse load   (b) Data acquision system

Figure 2.30. Photos of supplementary test instruments

(c) Load pump for prestressing force	(d) Crack gauge

Figure 2.30. (cont'd)

2.5   Test Results

The followings present the curves for:

- Beam moment-curvature (Figure 2.31 for PTE-3-50, Figure 2.40 for PTE-4-50, Figure 2.49 for PTE-3-75, Figure 2.58 for PTI-4-50, Figure 2.67 for RC-10-NA),

- Base shear-lateral displacement (Figure 2.32 for PTE-3-50, Figure 2.41 for PTE-4-50, Figure 2.50 for PTE-3-75, Figure 2.59 for PTI-4-50, Figure 2.68 for RC-10-NA),

- Beam moment-bar slip rotation (Figure 2.33 for PTE-3-50, Figure 2.42 for PTE-4-50, Figure 2.51 for PTE-3-75, Figure 2.60 for PTI-4-50, Figure 2.69 for RC-10-NA),

- Column axial load-lateral displacement (Figure 2.34 for PTE-3-50, Figure 2.43 for PTE-4-50, Figure 2.52 for PTE-3-75, Figure 2.61 for PTI-4-50, Figure 2.70 for RC-10-NA),

- Tendon force-lateral displacement (Figure 2.35 for PTE-3-50, Figure 2.44 for PTE-4-50, Figure 2.53 for PTE-3-75, Figure 2.62 for PTI-4-50),

- Crack width-residual crack width (Figure 2.36 for PTE-3-50, Figure 2.45 for PTE-4-50, Figure 2.54 for PTE-3-75, Figure 2.63 for PTI-4-50, Figure 2.71 for RC-10-NA),

- Crack patterns (Figures 2.37-2.38 for PTE-3-50, Figures 2.46-2.47 for PTE-4-50, Figures 2.55-2.56 for PTE-3-75, Figures 2.64-2.65 for PTI-4-50, Figures 2.72-2.73 for RC-10-NA),

- Damage photographs (Figure 2.39 for PTE-3-50, Figure 2.48 for PTE-4-50, Figure 2.57 for PTE-3-75, Figure 2.66 for PTI-4-50, Figure 2.74 for RC-10-NA).

Finally, a summary table is presented (see Table 2.14) to outline the the occurrence of phases corresponding to various limit states observed during the tests.
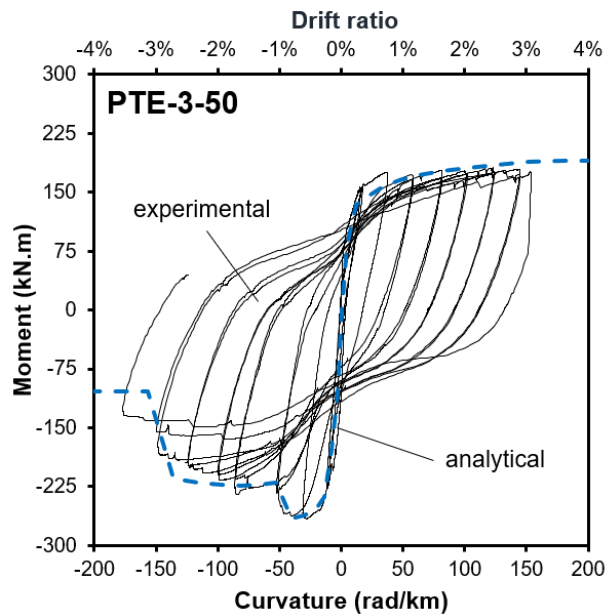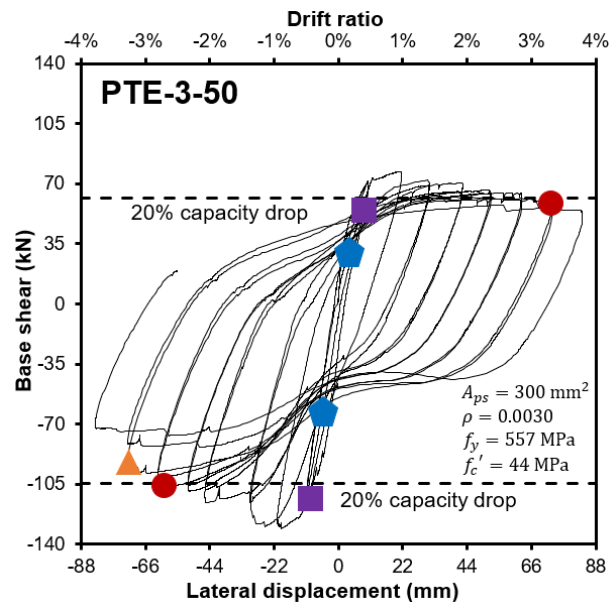

Figure 2.31. Moment-curvature for PTE-3-50

(*) Blue: First cracking, Purple: Yielding, Circle: Concrete crushing, Triangle: Bar buckling

Figure 2.32. Base shear-lateral displacement for PTE-3-50

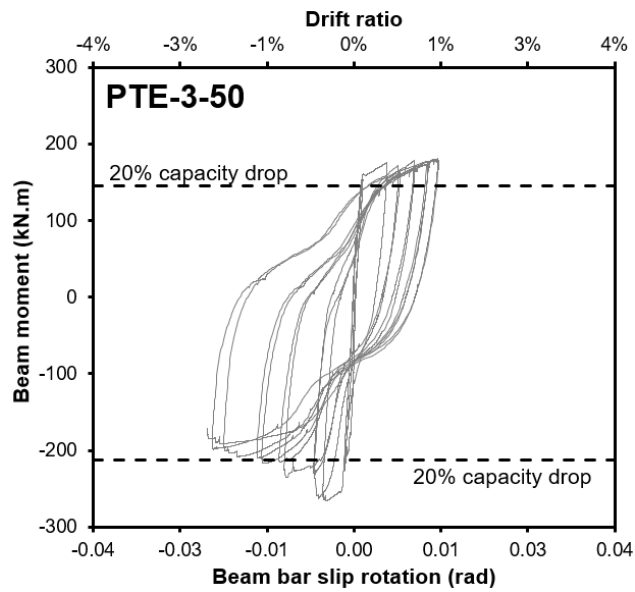
Figure 2.33. Beam moment-bar slip rotation for PTE-3-50
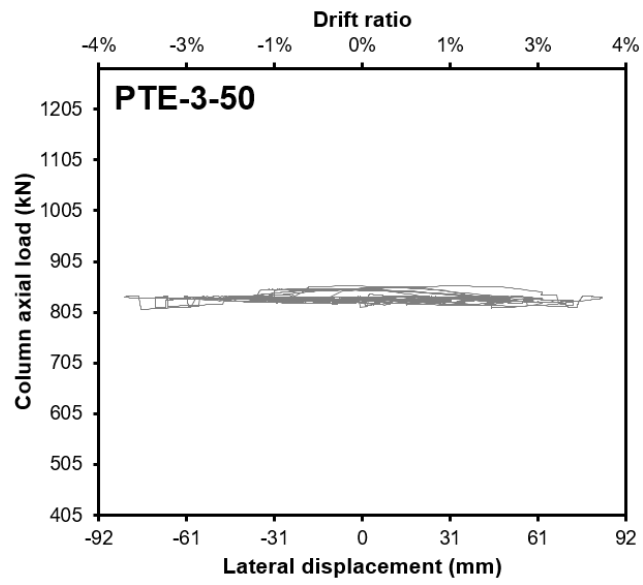
Figure 2.34. Column axial load-lateral diplacement for PTE-3-50

Figure 2.35. Tendon force-lateral diplacement for PTE-3-50

59

Figure 2.36. Crack width-drift ratio for PTE-3-50
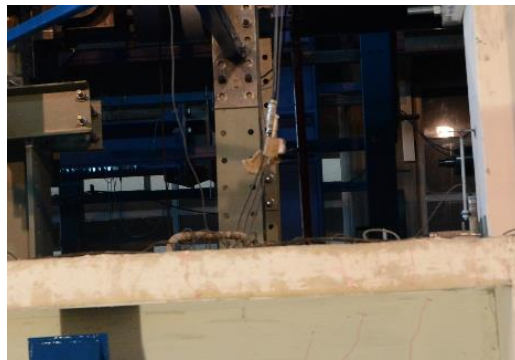
(a) 1% drift   (b) 2% drift

Figure 2.37. Crack patterns at drift ratios of 1% and 2% for PTE-3-50

(a) 3% drift   (b) 4% drift

Figure 2.38. Crack patterns at drift ratios of 3% and 4% for PTE-3-50

| (a) Slab cracking | (b) Bar buckling | (c) Plastic hinge formation |

Figure 2.39. Damage photos for PTE-3-50

Figure 2.40. Moment-curvature for PTE-4-50

(*) Blue: First cracking, Purple: Yielding, Circle: Concrete crushing, Triangle: Bar buckling

Figure 2.41. Base shear-lateral displacement for PTE-4-50

Figure 2.42. Beam moment-bar slip rotation for PTE-4-50
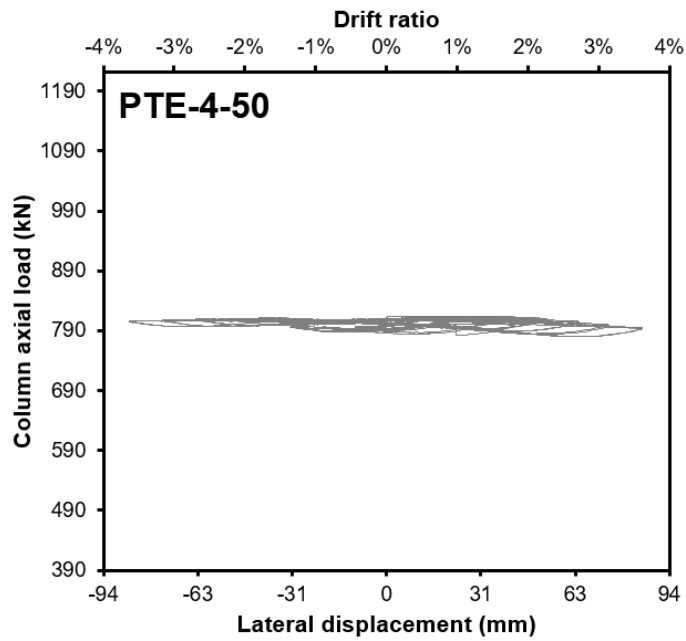
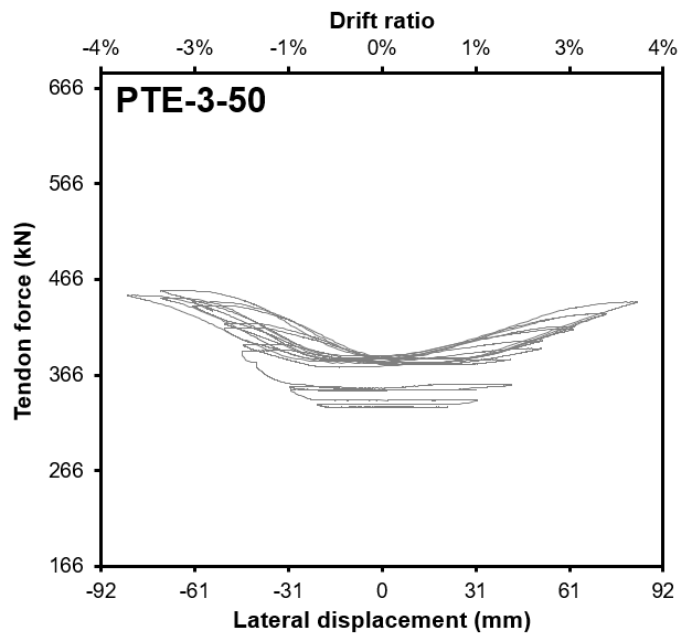Figure 2.43. Column axial load-lateral diplacement for PTE-4-50

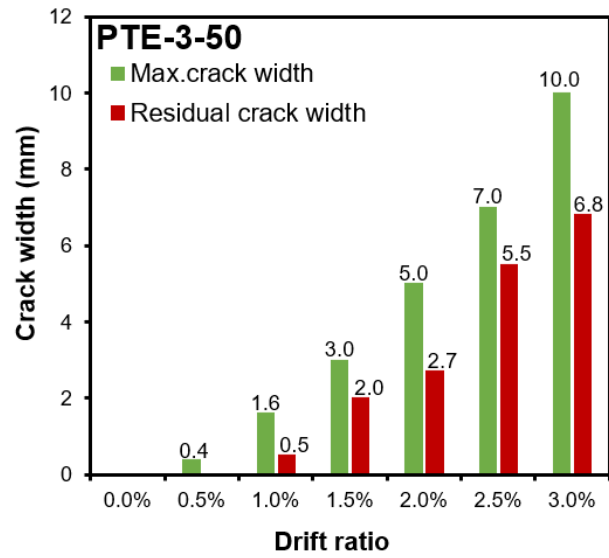
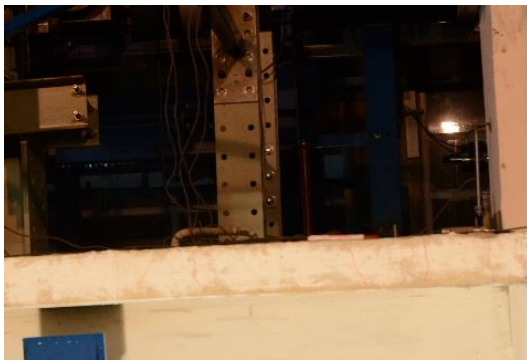Figure 2.44. Tendon force-lateral diplacement for PTE-4-50

Figure 2.45. Crack width-drift ratio for PTE-4-50

| a) 1% drift | b) 2% drift |

Figure 2.46. Crack patterns at drift ratios of 1% and 2% for PTE-4-50

| a) 3% drift | b) 4% drift |

Figure 2.47. Crack patterns at drift ratios of 3% and 4% for PTE-4-50

| (a) Slab cracking | (b) Bar buckling | (c) Plastic hinge formation |

Figure 2.48. Damage photos for PTE-4-50
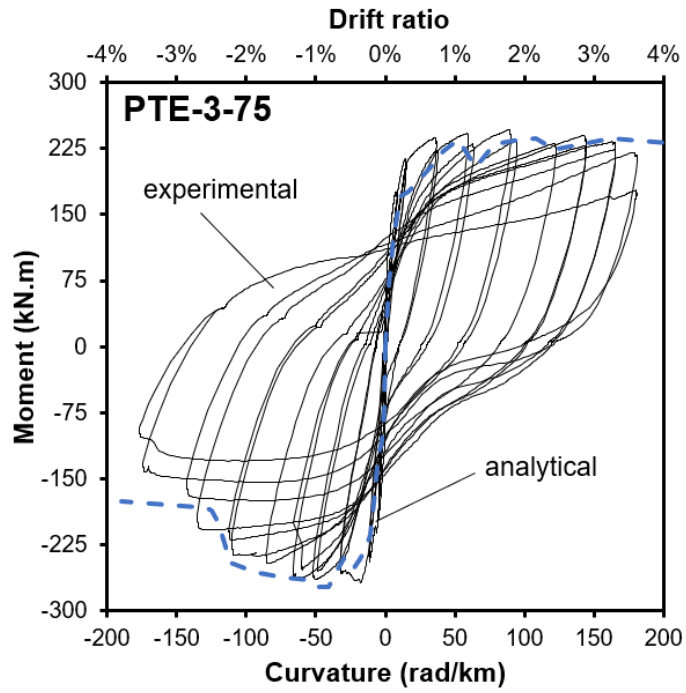
Figure 2.49. Moment-curvature for PTE-3-75
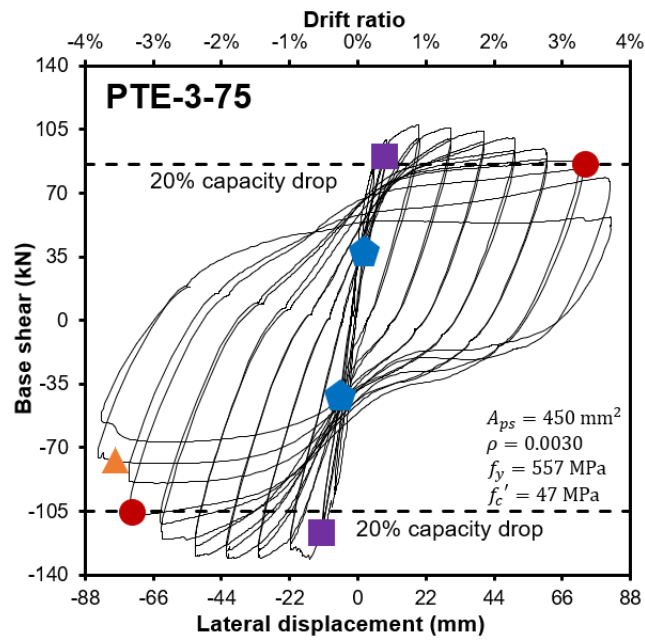
(*) Blue: First cracking, Purple: Yielding, Circle: Concrete crushing, Triangle: Bar buckling

Figure 2.50. Base shear-lateral displacement for PTE-3-75
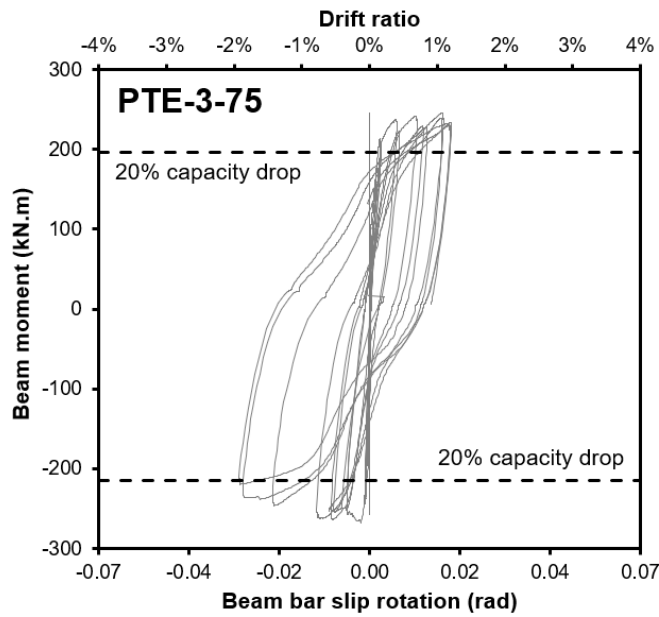
Figure 2.51. Beam moment-bar slip rotation for PTE-3-75
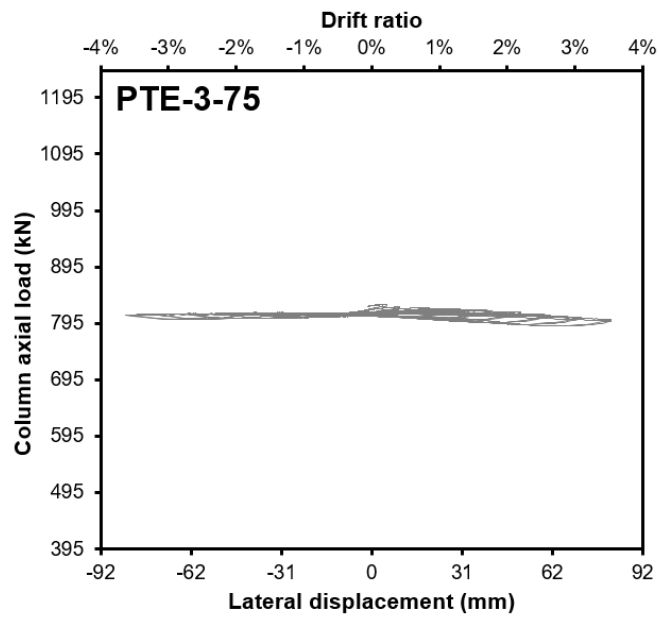
Figure 2.52. Column axial load-lateral displacement for PTE-3-75
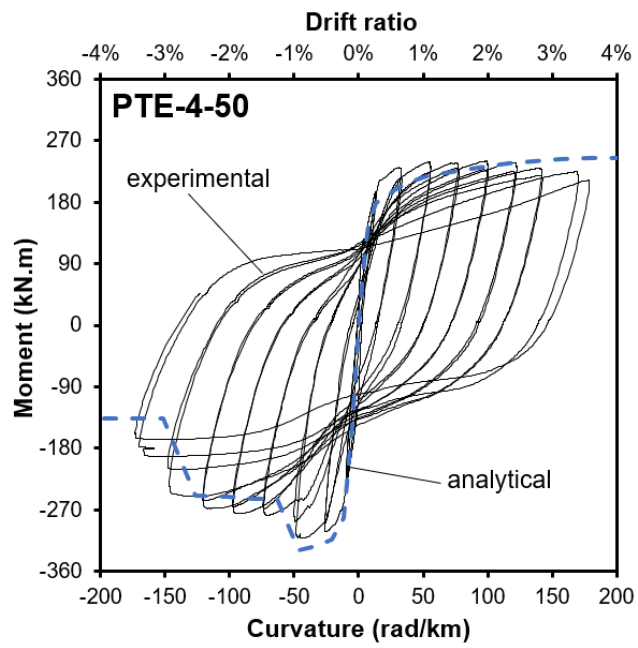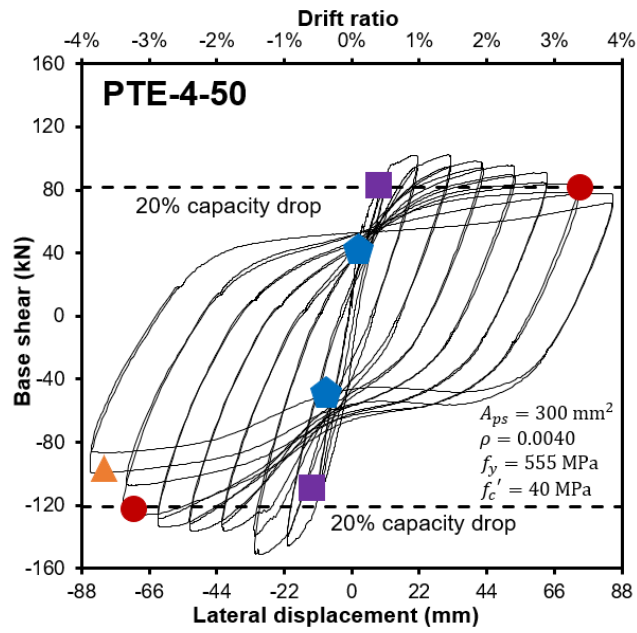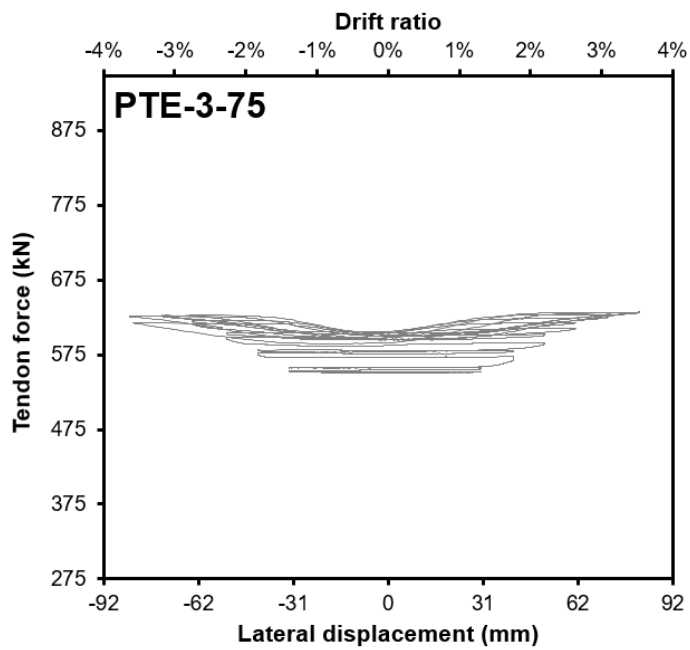

Figure 2.53. Tendon force-lateral diplacement for PTE-3-75
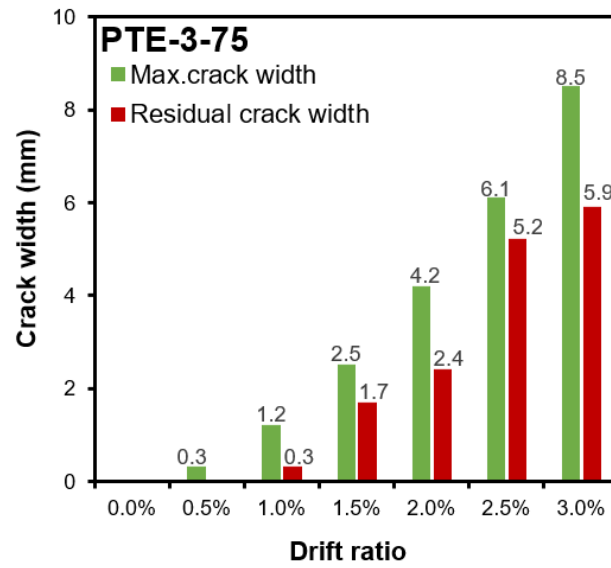
Figure 2.54. Crack width-drift ratio for PTE-3-75
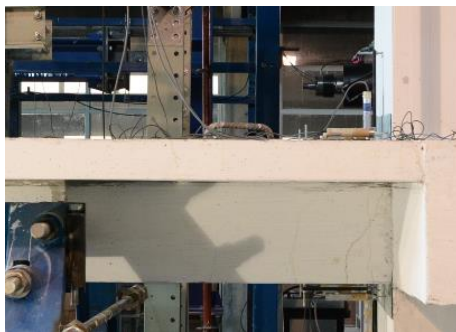
a) 1% drift   b) 2% drift

Figure 2.55. Crack patterns at drift ratios of 1% and 2% for PTE-3-75

a) 3% drift   b) 4% drift

Figure 2.56. Crack patterns at drift ratios of 3% and 4% for PTE-3-75

| (a) Slab reinforcement rupture | (b) Concrete cover spalling | (c) Plastic hinge formation |

Figure 2.57. Damage photos for PTE-3-75
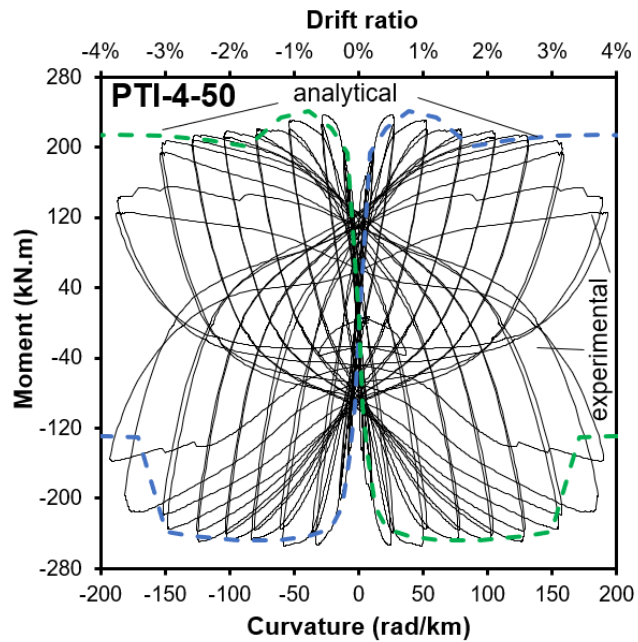
Figure 2.58. Moment-curvature for PTI-4-50 (two cyclic curves presented belong to the left end and right spans of the interior specimen)
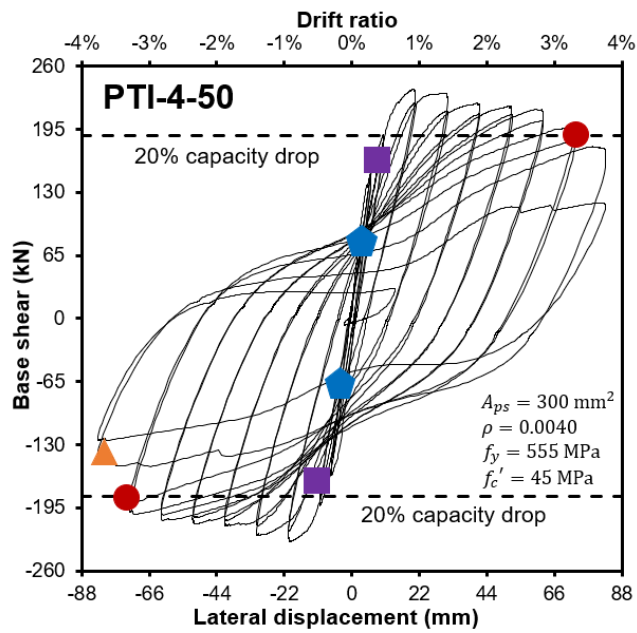
(*) Blue: First cracking, Purple: Yielding, Circle: Concrete crushing, Triangle: Bar buckling

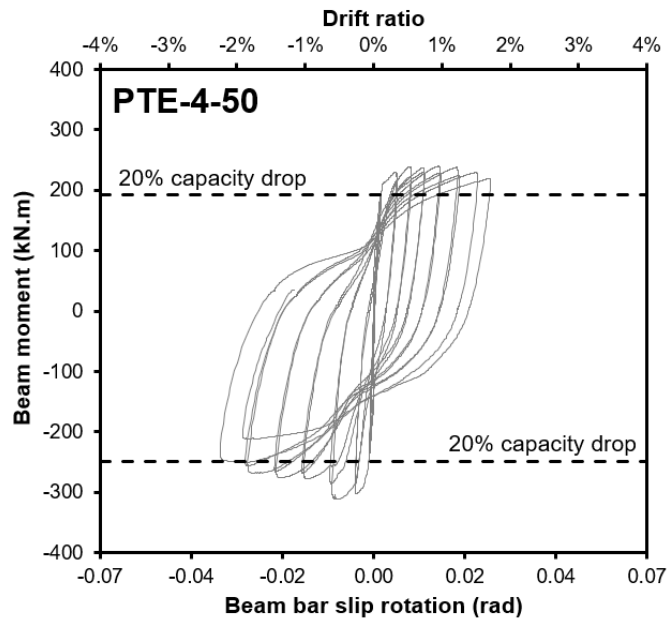Figure 2.59. Base shear-lateral displacement for PTI-4-50
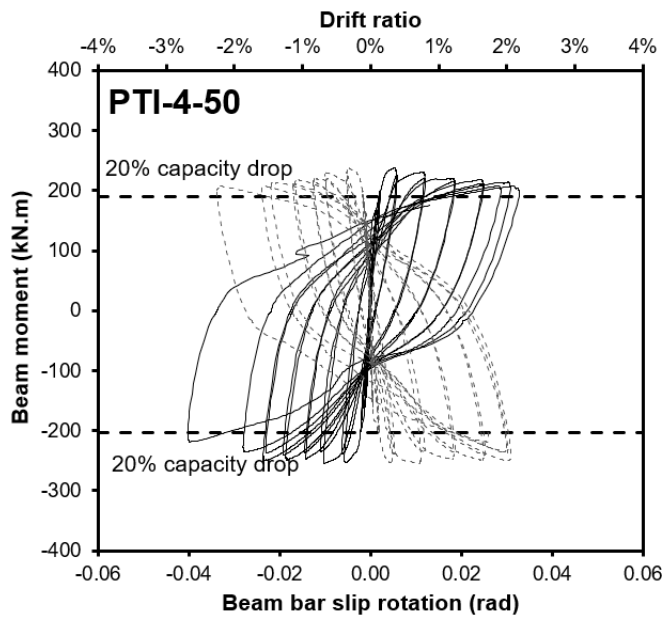
Figure 2.60. Beam moment-bar slip rotation for PTI-4-50
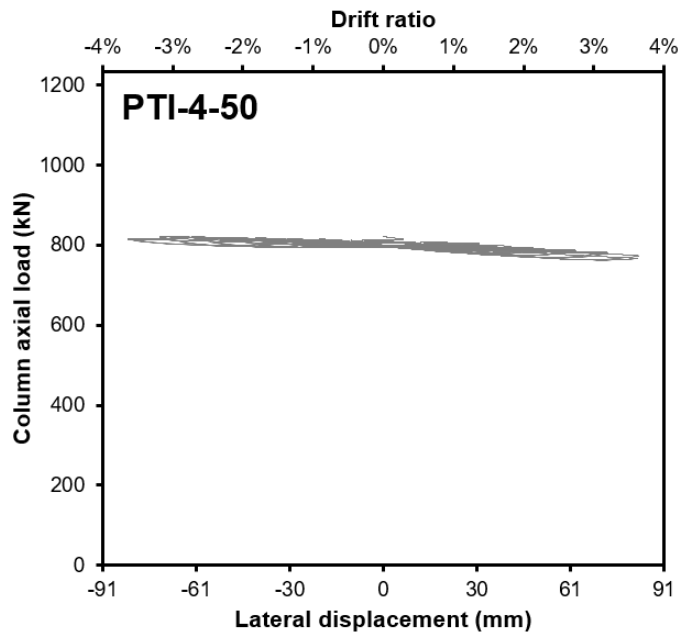
Figure 2.61. Column axial load-lateral displacement for PTI-4-50
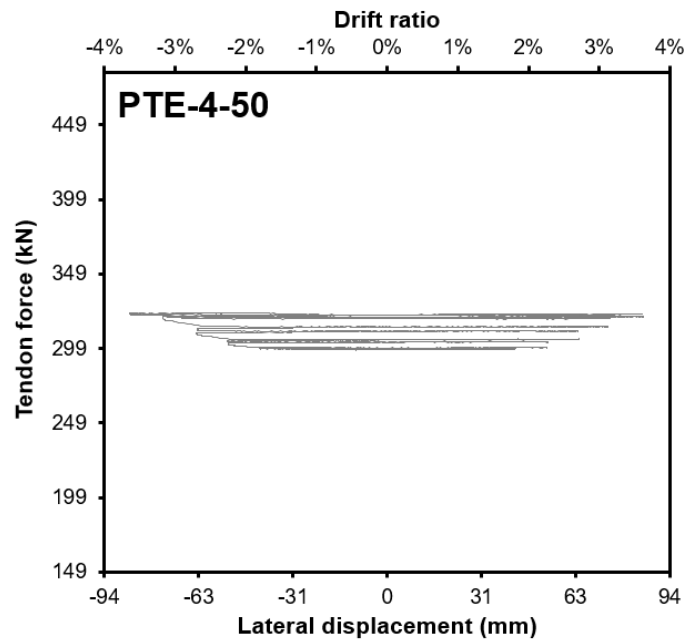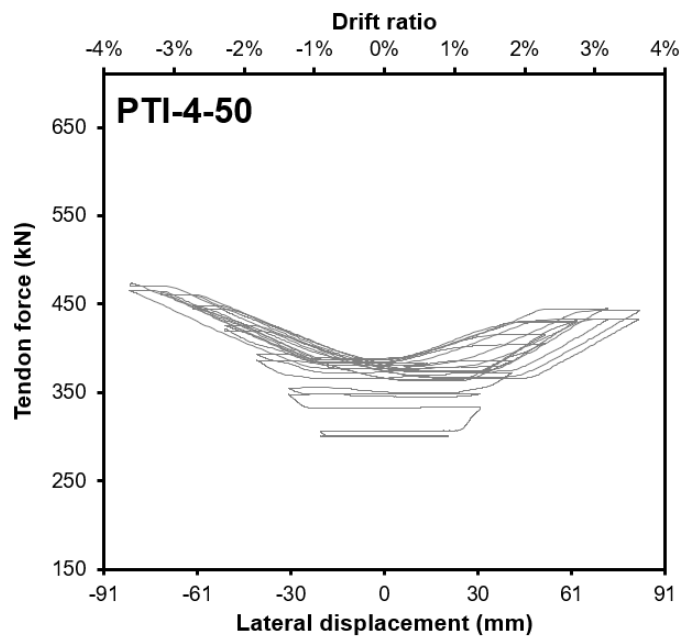

Figure 2.62. Tendon force-lateral displacement for PTI-4-50
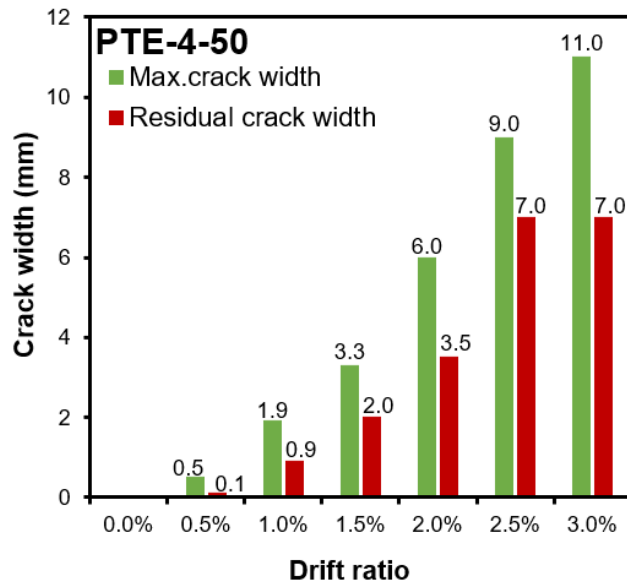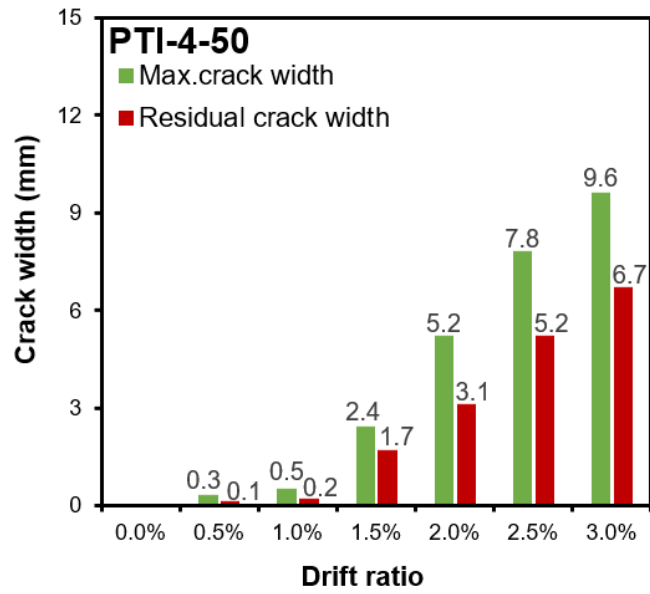
Figure 2.63. Crack width-drift ratio for PTI-4-50

a) 1% drift   b) 2% drift

Figure 2.64. Crack patterns at drift ratios of 1% and 2% for PTI-4-50

a) 3% drift   b) 4% drift

Figure 2.65. Crack patterns at drift ratios of 3% and 4% for PTI-4-50

(a) Bar buckling	(b) Plastic hinge formation

Figure 2.66. Damage photos for PTI-4-50
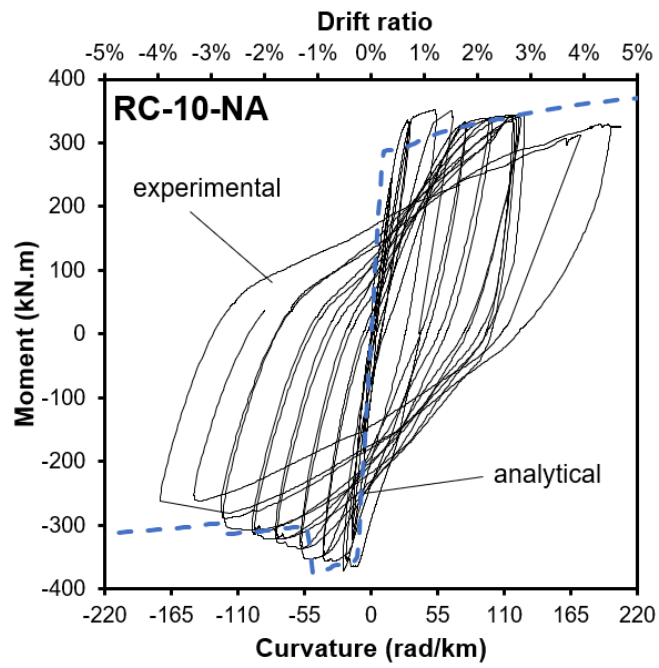
Figure 2.67. Moment-curvature for RC-10-NA
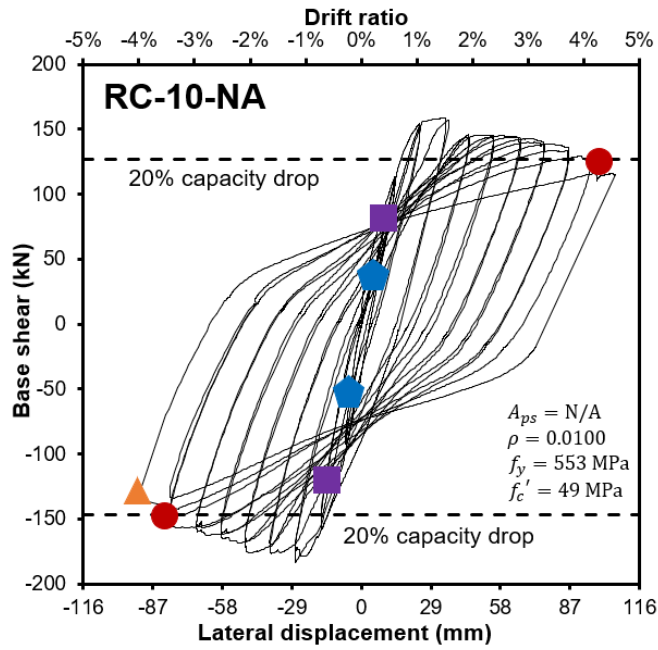
(*) Blue: First cracking, Purple: Yielding, Circle: Concrete crushing, Triangle: Bar buckling

Figure 2.68. Base shear-lateral displacement for RC-10-NA
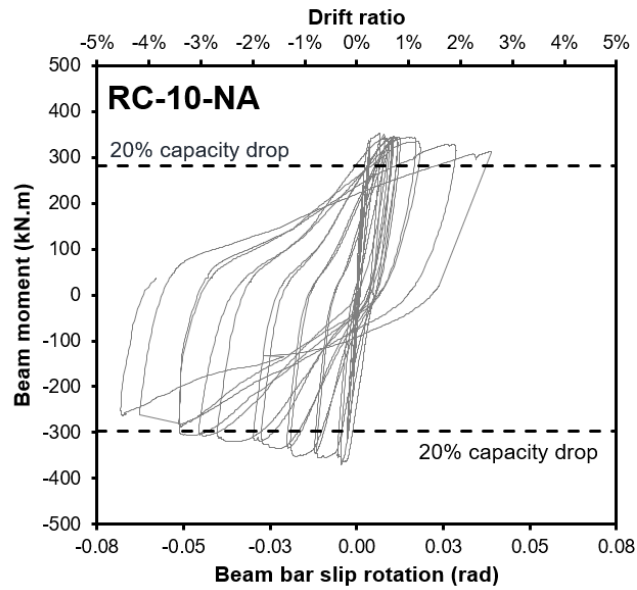
Figure 2.69. Beam moment-bar slip rotation for RC-10-NA
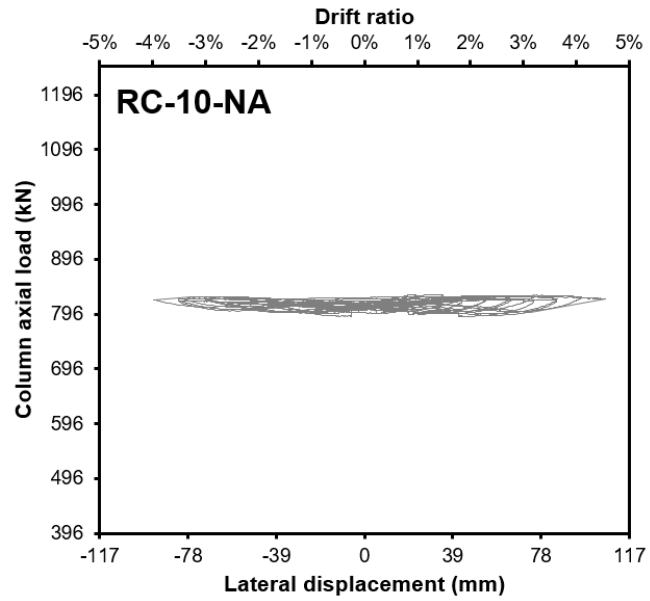
Figure 2.70. Column axial load-lateral displacement for RC-10-NA
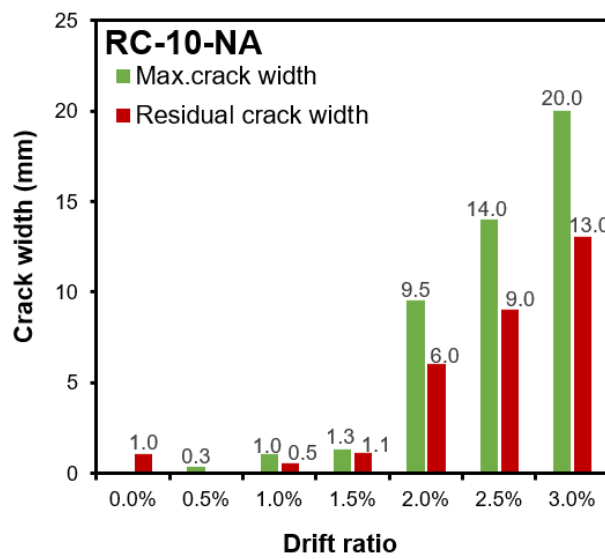
Figure 2.71. Crack width-drift ratio for RC-10-NA

a) 1% drift   b) 2% drift

Figure 2.72. Crack patterns at drift ratios of 1% and 2% for RC-10-NA

a) 3% drift   b) 4% drift

Figure 2.73. Crack patterns at drift ratios of 3% and 4% for RC-10-NA

(a) Slab cracking   (b) Bar buckling   (c) Plastic hinge
   formation

Figure 2.74. Damage photos for RC-10-NA

Table 2.14 Drift Levels of Limit States

	Push loading			
Specimen	First flexural cracking	First yielding	Peak load	Concrete crushing
PTE-3-50	0.25%	0.33%	0.99%	3.29%
PTE-4-50	0.25%	0.37%	1.48%	3.47%
PTE-3-75	0.30%	0.31%	0.94%	3.44%
PTI-4-50	0.35%	0.37%	0.97%	3.49%
RC-10-NA	0.30%	0.38%	1.68%	4.65%
	Pull loading			
Specimen	First flexural cracking	First yielding	Peak load	Concrete crushing
PTE-3-50	0.35%	0.47%	0.94%	2.62%
PTE-4-50	0.30%	0.51%	1.39%	3.29%
PTE-3-75	0.40%	0.54%	0.74%	3.42%
PTI-4-50	0.35%	0.42%	0.96%	3.49%
RC-10-NA	0.30%	0.47%	1.32%	3.95%

The results demonstrated that the capacity curves provided a reasonable prediction for the experimental outcomes of all specimens, highlighting the accuracy of the analytical approach. In addition to the laboratory results presented in the previous sections, Figure 2.75 depicts a typical cyclic load-deformation relationship, which serves as a framework for evaluating energy-based parameters listed below:

i. E_d, the cumulative energy dissipation, is represented by the enclosed area denoted as **abcda** on the hysteresis loop.

ii. E_{s0}, the strain energy, is calculated as the summation of the areas of the dashed regions labeled **oafo** and **oceo** within the hysteresis curve.

iii. ζ_{eq}, the equivalent viscous damping ratio, is defined as $E_d/2\pi E_{s0}$ (Chopra, 2015). This parameter characterizes the extent of energy dissipated during inelastic deformation, reflecting the level of damage sustained throughout the loading cycles.
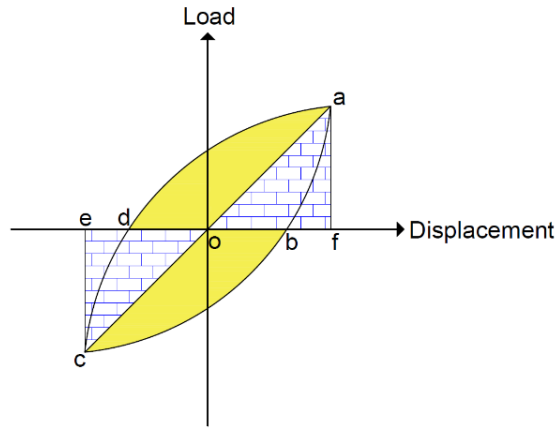
Figure 2.75. Generic hysteresis loop for cyclic loading

Figures 2.76a and 2.76b indicate the cumulative dissipated energy and the equivalent viscous damping ratio curves for the test specimens, respectively. Additionally, Figure 2.77 explores the normalized stiffness degradation behavior among the specimens. The peak load-lateral displacement pairs are extracted from the experimental data for each cycle i. Using these values, the secant stiffness (K_{sec}) is calculated based on Equation 2-2. Finally, the secant stiffness at each cycle is normalized by dividing it by the initial secant stiffness, providing a dimensionless parameter to evaluate stiffness degradation trends.

$$K_{sec} = \frac{|F_i^+| + |F_i^-|}{|\Delta_i^+| + |\Delta_i^-|} \qquad (2\text{-}2)$$

where:

F_i^+, F_i^- are the maximum loads at i^{th} cycle in push and pull directions, respectively.

Δ_i^+, Δ_i^- are the lateral displacements corresponding to F_i^+ and F_i^-, respectively.
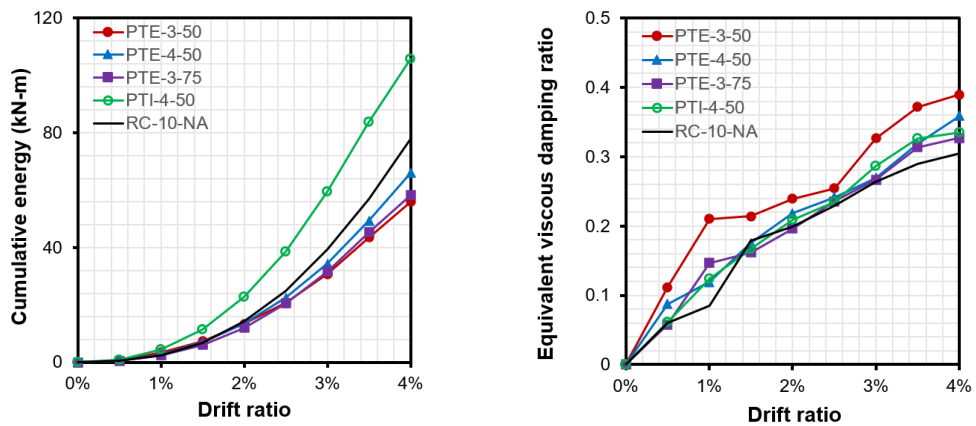
(a) Cumulative dissipated energy (b) Equivalent viscous damping ratio

Figure 2.76. Energy-based parameters
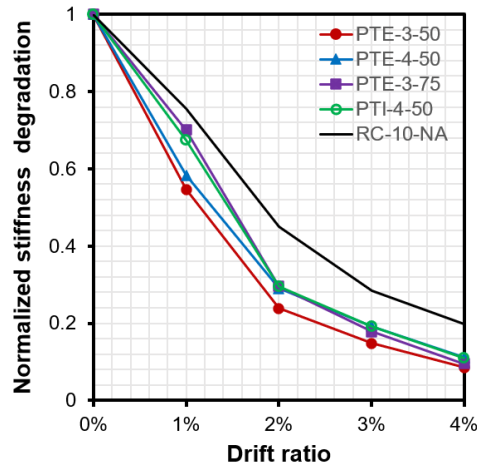
Figure 2.77. Normalized stiffness degradation

A comprehensive summary of the experimental results is provided in Table 2.15. In this table, yield displacement (Δ_y) and yield curvature (ϕ_y) values were identified based on the point where the tensile reinforcement first reached its yield strain. This determination was accomplished using data obtained from the corresponding LVDT readings. Furthermore, the associated load at this point was designated as the yield lateral load (V_y). Conversely, ultimate displacement (Δ_u) and ultimate curvature (ϕ_u) values were determined at the points where a 20% reduction in capacity was observed for the lateral load and moment, respectively, as per the criteria outlined in

the study conducted by Park (1989). The maximum load recorded during the tests was defined as the ultimate load (V_{ult}). In addition to these parameters, the shear capacity (V_{shear}) of a section reinforced with transverse steel was calculated through the following equations proposed in ACI 318:

$$V_{con,ps} = min[(0.05\sqrt{f_c'} + 4.8\frac{V_u d_p}{M_u})b_w d; \left(0.05\sqrt{f_c'} + 4.8\right)b_w d; 0.42\sqrt{f_c'}b_w d] \qquad (2\text{-}3)$$

$$V_{con,rc} = [0.17\sqrt{f_c'} + \frac{N_u}{6A_g}]b_w d \qquad (2\text{-}4)$$

$$V_{steel} = \frac{A_v f_{yt} d}{s} \qquad (2\text{-}5)$$

$$V_{shear} = 0.75(V_c + V_{steel}) \qquad (2\text{-}6)$$

Equations 2-3 and 2-4 are employed to compute the shear force due to the concrete (V_c) for prestressed and non-prestressed sections, respectively. The shear contribution from transverse reinforcement (V_{steel}) is determined using Equation 2-5. The total shear force (V_{shear}) is subsequently calculated by summing V_c and V_{steel} and applying a strength reduction factor, as defined in Equation 2-6.

In these equations, f_{yt} denotes the yield strength of the transverse reinforcement, while b_w represents the width of the rectangular section. The parameters d and d_p correspond to the distances from the extreme compression fiber of the concrete to the centroids of the tension steel and the prestressing strand, respectively. Additionally, A_g signifies the gross area of the beam section, whereas A_v and s refer to the cross-sectional area and spacing of the shear reinforcement. Finally, N_u, V_u, and M_u are the factored axial load, shear force, and moment, respectively, used in the design calculations. Additionally, the envelope curves for moment, base shear and, crack width are given in Figure 2.78.
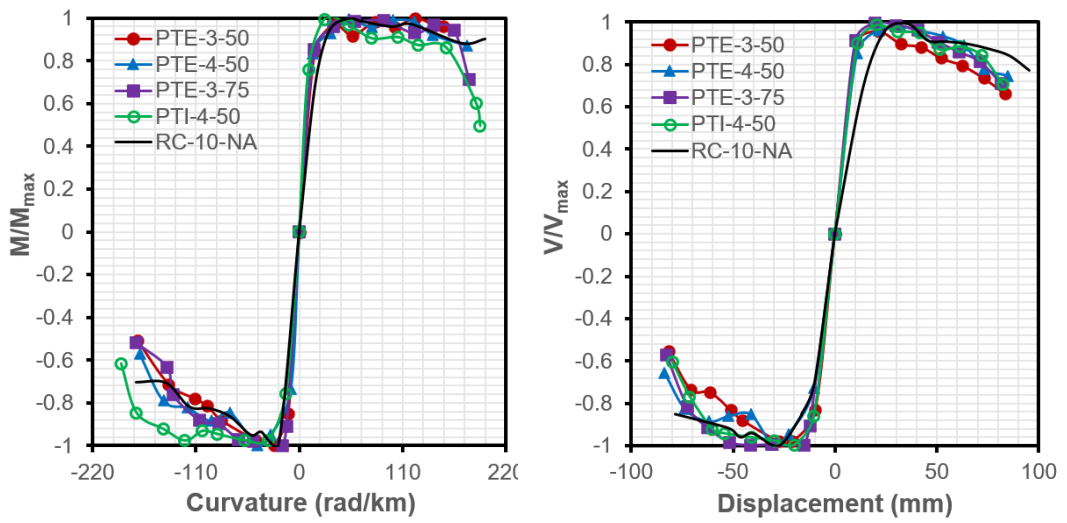
(a) Moment envelope

(b) Shear envelope
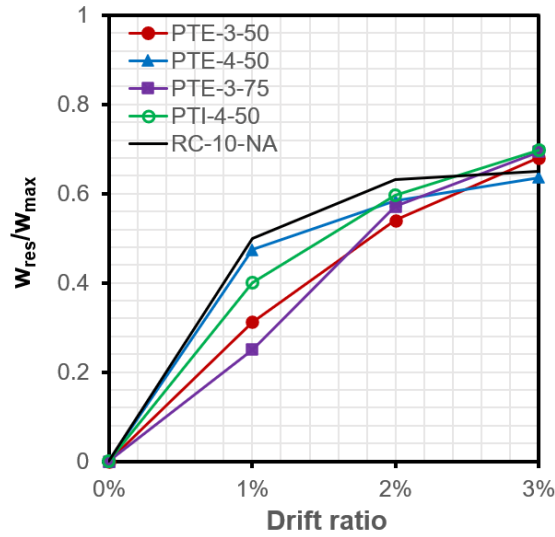
(c) Crack width envelope

Figure 2.78. Envelope curves for moment, shear, and crack width

81

Table 2.15 Summary of Test Results

Specimen	K_i^+ (kN/m)	Δ_y^+ (mm)	Δ_u^+ (mm)	ϕ_y^+ (rad/km)	ϕ_u^+ (rad/km)	μ_Δ^+	μ_ϕ^+	M_{max}^+ (kN-m)	V_{flex}^+ (kN)	V_{shear}^+ (kN)	V_y^+ (kN)	V_{ult}^+ (kN)
PTE-3-50	8992.6	6.8	68.2	9.8	144.0	10.1	14.7	181.2	116.9	720.1	60.7	77.2
PTE-4-50	10492.9	7.7	73.2	9.9	121.4	9.5	12.3	240.0	154.8	702.7	80.9	102.2
PTE-3-75	14060.0	6.3	71.3	10.3	178.6	11.3	17.3	246.2	158.9	730.1	89.0	107.7
PTI-4-50	22403.1	7.7	72.5	10.6	177.4	9.4	16.7	237.6	306.6	719.9	173.4	236.3
RC-10-NA	10140.1	7.9	96.5	9.8	206.7	12.3	21.1	352.6	227.5	538.4	79.6	158.8

Specimen	K_i^- (kN/m)	Δ_y^- (mm)	Δ_u^- (mm)	ϕ_y^- (rad/km)	ϕ_u^- (rad/km)	μ_Δ^-	μ_ϕ^-	M_{max}^+ (kN-m)	V_{flex}^+ (kN)	V_{shear}^+ (kN)	V_y^+ (kN)	V_{ult}^- (kN)
PTE-3-50	11228.1	9.7	54.4	10.5	95.5	5.6	9.1	266.1	171.7	720.1	108.8	130.7
PTE-4-50	10577.3	10.7	69.3	10.6	120.0	6.5	11.3	311.7	201.1	702.7	113.6	151.1
PTE-3-75	10535.2	11.2	70.7	11.1	111.8	6.3	10.1	268.7	173.3	730.1	118.1	131.3
PTI-4-50	20422.4	8.8	72.5	10.3	171.0	8.3	16.6	254.1	327.8	719.9	178.9	239.7
RC-10-NA	12482.0	9.7	82.0	9.3	116.1	8.4	12.5	371.8	239.9	538.4	121.2	183.4

2.6 Evaluation of Test Results

2.6.1 Moment-curvature response

Moment-curvature responses (see Figures 2.31, 2.40, 2.49, 2.58, 2.67) highlight two abrupt capacity reductions in the pull direction at a drift ratio of approximately 1% and at a drift ratio of around 3%. The first reduction can be attributed to the fracture of slab mesh reinforcement which has limited ductility whereas the second drop is associated with extensive damage in the plastic hinge region in the form of concrete crushing, large crack openings, and possibly reduction of bond strength for the post-tensioning steel. Also, the figures demonstrated that a high level of accuracy was obtained between standard moment-curvature analyses. The test results summarized in Table 2.15 reveal that the maximum moment capacities, in both push and pull directions, were achieved by specimen RC-10-NA.

The influence of longitudinal reinforcement ratio on structural behavior was analyzed by evaluating specimens PTE-3-50 and PTE-4-50. Accordingly, PTE-4-50 exhibited approximately 33% and 17% higher moment capacities as compared to PTE-3-50 in the positive and negative load directions, respectively. In other words, post-tensioning effectively acting in the pull (negative) direction decreases the contribution of mild steel, which can be attributed to the presence of partial prestressing. Besides, the pull-to-push moment capacity ratios were around 1.5 for PTE-3-50 and 1.3 for PTE-4-50, indicating that post-tensioning effects are more pronounced in specimens with lower mild steel ratios.

The role of tendon area was further investigated by comparing PTE-3-50 and PTE-3-75. The improvement in moment capacities from push to pull direction was significantly higher for PTE-3-50 (1.5 times) than for PTE-3-75 (1.1 times). The difference might result from the mild steel-to-tendon area ratio. This indicates that a larger ratio contributes to enhanced structural performance.

Lastly, the responses of exterior (PTE-4-50) and interior (PTI-4-50) specimens were examined. Due to the symmetry in tendon layout and support configuration, the interior specimen demonstrated nearly identical push and pull moment capacities, as expected. Conversely, the exterior specimen exhibited approximately 20% higher moment capacity in the pull direction, which can be explained by its cantilever configuration, where all loads were transferred to a roller support, leading to increased force demands.

Based on Table 2.15, it can be stated that all post-tensioned specimens had lower curvature ductility in the pull direction, reflecting the brittle behavior of the prestressing steel. Additionally, the yield curvature values in the push and pull directions for all test joints were closely similar due to the equal ratios of top reinforcement area to bottom reinforcement area, which were 1.0. Apart from those, the reductions in curvature ductility were about 40% and 10% for PTE-3-50 and PTE-4-50, respectively (the effect of reinforcing steel). Such a major difference might be explained by the crucial role of mild steel on the specimen response. This result implies that a higher amount of longitudinal rebar provided similar curvature ductility trends in both loading scenarios. Besides, greater curvature ductility was attained in the pull direction as the percentage of mild steel became larger (see Figure 2.79). In this figure, it is noted that the specimen having a mild steel ratio of 0.67% was examined in the study of Karageyik (2024). On the other hand, curvature ductility drops of about 40% were observed for both PTE-3-75 and PTE-3-50 (the effect of tendon area). Then, it can be thought that the level of load-balancing ratio showed little impact on curvature ductility (see Figure 2.80). Furthermore, it was seen that PTE-4-50 and PTI-4-50 provided nearly identical curvature ductility responses in both loading directions. It is theoretically known that frame geometry is not a significant parameter in the evaluation of curvature ductility. In this regard, this behavior is an expected result because cross-sectional dimensions, material properties, mild steel amounts, and tendon areas are identical for both test specimens. For the evaluation of RC-10-NA, the table also shows that the curvature ductility in

the pull direction was about 60% of that in the push direction. This situation can be supported by the earlier crushing of concrete in the pull direction.

Figure 2.79. The effect of tension steel ratio on the curvature ductility
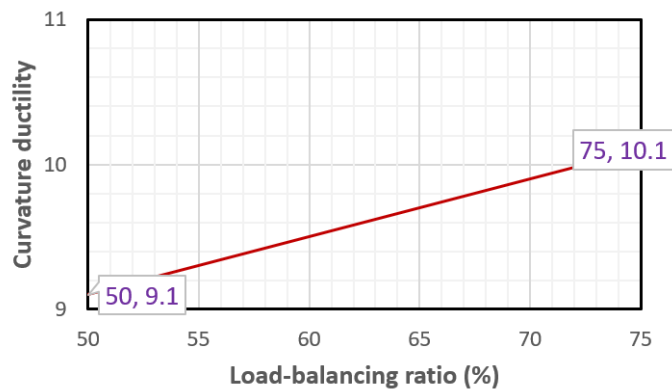
Figure 2.80. The effect of load-balancing ratio on the curvature ductility

2.6.2 Base shear-lateral displacement

The detailed comparative analyses of the moment-curvature relationship can be extended to base shear-lateral displacement behavior, enabling a consistent evaluation of ultimate loads (see Figures 2.32, 2.41, 2.50, 2.59, 2.68) through the reasoning applied to maximum moments in Section 2.6.1. Additionally, further insights can be derived using supplementary observations. For instance, as noted in

Table 2.15, ultimate lateral loads (V_{ult}) exceeded the flexural-shear capacities (V_{flex}) for all specimens, indicating a flexure-dominated failure mechanism.

The discussion on displacement ductility levels (μ_Δ) reveals the influence of post-tensioning, particularly in the pull direction and the comparisons between specimens demonstrate notable trends (see Table 2.15). For example, the higher ratio of mild steel in PTE-4-50 compared to PTE-3-50 resulted in a more ductile response, as the increased non-prestressed steel ratio reduced the partial prestressing ratio and mitigated the influence of post-tensioning (see Figure 2.81). Therefore, PTE-4-50 showed approximately 15% greater displacement ductility. Similarly, an increase in load-balancing ratio, as seen in PTE-3-75 relative to PTE-3-50, provided additional tensile force and marginally improved displacement ductility (see Figure 2.82). Another significant inference in ductility was done between the exterior specimen (PTE-4-50) and the interior specimen (PTI-4-50). The interior specimen exhibited approximately 30% higher ductility due to the symmetric placement of roller supports on either side of the beam-to-column joint, which enhanced its deformation capacity. Notably, the highest ductility was recorded in the non-post-tensioned specimen (RC-10-NA), implying the crucial role of mild steel in determining deformation capacity.

Insights from Table 2.14 further explain the influence of post-tensioning. In the pull direction, the first flexural cracks appeared at higher drift ratios because post-tensioning minimized residual deformations and reduced seismic vulnerability. Post-tensioned specimens reached their peak loads earlier in the pull direction, driven by the additional load-carrying capacity imparted by prestressing steel. However, this enhancement in capacity was accompanied by distinct failure patterns: Steel yielding occurred at higher drift ratios, while concrete crushing initiated at lower drift ratios.

These phenomena can be attributed to the combined behavior of mild steel and prestressing strand. The synergy between these materials delays the yielding of tension steel through mechanisms such as force redistribution, thereby contributing to the load resistance. However, the restriction on deformation capacity imposed by

post-tensioning promotes brittle failure. Consequently, concrete reaches its ultimate strain more quickly, leading to cover spalling and premature crushing, as observed during testing.
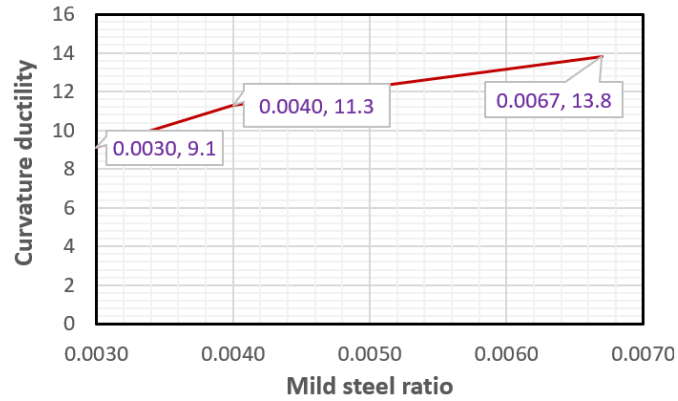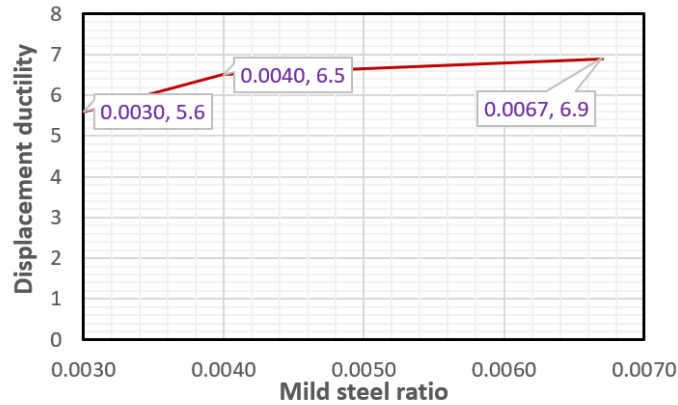

Figure 2.81. The effect of tension steel ratio on the displacement ductility
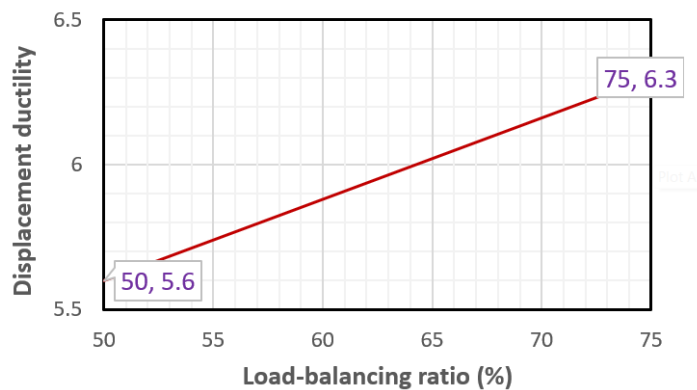
Figure 2.82. The effect of load-balancing ratio on the displacement ductility

2.6.3   Maximum and residual crack width

Figures 2.36, 2.45, 2.54, 2.63, 2.71 provide valuable insights into the progression of damage levels observed in the test specimens throughout the loading protocol. These figures demonstrate that as loading advanced, the maximum and residual crack widths increased proportionally with the mild steel ratio in post-tensioned beams (e.g., PTE-3-50 vs. PTE-4-50). This indicates that higher non-prestressed steel ratios

resulted in larger crack widths (see Figure 2.83). Besides, smaller crack widths were observed in PTE-3-75 compared to PTE-3-50, primarily due to differences in their load-balancing ratios. Theoretically, a greater load-balancing ratio in post-tensioned specimens induces a compressive force that counteracts the tensile stresses caused by vertical loads. This reduction in tensile stress helps mitigate crack formation. Experimental results, as illustrated in Figures 2.36, 2.45, 2.54, 2.63, align with this theoretical expectation, confirming that increased load-balancing ratios contribute to better crack control. Moreover, PTI-4-50 exhibited smaller crack widths and a more organized crack pattern compared to PTE-4-50. This behavior can be attributed to the symmetrical test setup, which distributed internal forces more evenly.

Notably, post-tensioned specimens displayed no residual cracks up to a drift ratio of 1%, unlike the conventional reinforced concrete beam, which exhibited visible cracks during the early stages of loading. This distinction signifies the self-centering capability of post-tensioning systems, which effectively minimize residual deformations, such as cracks and excessive deflections. As a result, post-tensioned systems demonstrate superior crack control and structural integrity compared to conventional reinforced concrete systems.

Figure 2.78c further highlights the influence of post-tensioning on crack propagation by examining the ratio of residual crack width to maximum crack width (w_{res}/w_{max}). At a 1% drift level, the minimum and maximum values of this parameter were observed for PTE-3-75 and RC-10-NA, respectively, with corresponding ratios of approximately 0.25 and 0.50. This difference indicates that higher values of w_{res}/w_{max} correlate with more inelastic deformation, emphasizing the effectiveness of post-tensioning in reducing crack development, particularly in the initial stages of loading. At a 3% drift level, however, the w_{res}/w_{max} ratio converged to about 0.6 for all specimens. This outcome can be attributed to the onset of concrete cover spalling, which typically occurs at such deformation levels, marking a transition to more significant structural degradation.
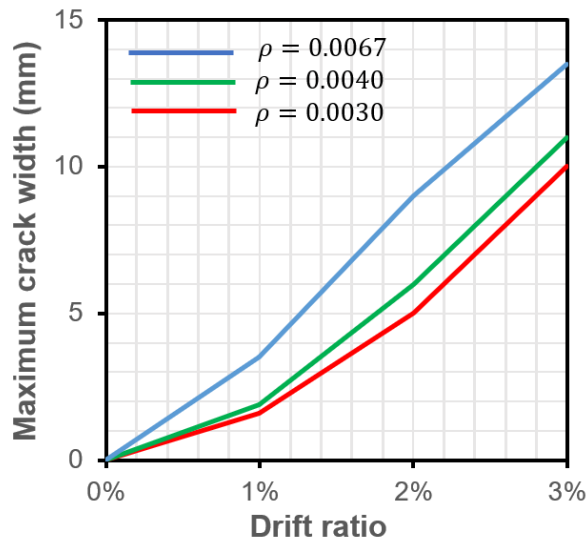
Figure 2.83. The effect of tension steel ratio on the crack width

2.6.4 Cumulative dissipated energy

Figure 2.76a illustrates that the cumulative energy dissipation paths for PTE-3-50 and PTE-3-75 were nearly identical. This similarity can be explained by the same amount of mild steel used in both specimens, despite the difference in their tendon areas. Consequently, the variation in prestressing steel had a limited influence on the cumulative energy dissipation. However, the same figure reveals that PTE-4-50 exhibited approximately 15% higher cumulative energy dissipation compared to PTE-3-50. This observation aligns with the ductility levels in the pull direction presented in Table 2.15 and it is primarily due to the elastoplastic behavior and inherent ductility of mild steel.

When considering the reinforced concrete specimen RC-10-NA, it displayed the highest cumulative energy dissipation among the exterior test beams, surpassing PTE-4-50 by a factor of approximately 1.2. This outcome further indicates the critical role of mild steel in determining energy dissipation, consistent with its influence on displacement ductility levels.

The interior specimen PTI-4-50 demonstrated significantly better performance, with a cumulative energy dissipation ratio to PTE-4-50 of approximately 1.75. This notable difference can be attributed to the double flange effect, which enhanced energy dissipation capacity, facilitated uniform load distribution, and improved seismic performance.

Figure 2.76b focuses on the equivalent viscous damping ratios, revealing that all specimens except PTE-3-50 exhibited similar trends up to a 3% drift ratio, corresponding to the onset of concrete cover spalling. Also, PTE-3-50 achieved the highest equivalent viscous damping ratio at the 4% drift level (approximately 0.4). This behavior can be linked to the earlier occurrence of concrete crushing in this specimen, as detailed in Table 2.14. Consequently, the hysteresis loops narrowed, decreasing the ratio of strain energy to total energy. This reduction resulted in the lowest displacement ductility among all test specimens, as noted in Table 2.15.

Conversely, RC-10-NA exhibited the lowest equivalent viscous damping ratio at the 4% drift level (approximately 0.3), because concrete crushing occurred in the later stages of this specimen. This delayed failure mechanism is consistent with the specimen's superior ductile performance, as discussed earlier. These results emphasize the interaction between energy dissipation, damping characteristics, and ductility in evaluating seismic performance.

2.6.5 Normalized stiffness degradation

Figure 2.77 highlights the progressive reduction in normalized stiffness for the beam-to-column joints as the drift level increased. Initially, a rapid deterioration in stiffness was observed due to the formation of flexural cracks. This degradation decelerated after the tension steel yielded, resulting in a more gradual reduction.

Both PTE-3-50 and PTE-4-50 exhibited comparable trends in stiffness degradation throughout the tests. However, PTE-4-50 demonstrated slightly smaller stiffness loss due to its higher mild steel content. Furthermore, at a 1% drift ratio, PTE-3-50

experienced approximately 1.3 times greater stiffness loss than PTE-3-75. This difference can be caused by the variations in tendon area and load-balancing levels, emphasizing the role of prestressing steel in improving stiffness. The high tensile strength of the prestressing steel contributed to reduced stiffness loss, with greater tendon areas and higher load-balancing ratios mitigating severe degradation.

A comparison between PTE-4-50 and PTI-4-50 further illustrates the influence of structural configuration. At a 1% drift ratio, PTI-4-50 displayed around 30% greater stiffness degradation compared to PTE-4-50. This outcome signals that the interior specimen experienced less stiffness loss due to its symmetric configuration, which facilitated effective load transfer through the support elements and structural members. The double-flanged beam design of PTI-4-50 mitigated abrupt capacity changes, contributing to its enhanced stiffness performance.

Towards the end of the tests, all post-tensioned beams exhibited similar levels of normalized stiffness degradation. However, the conventional RC-10-NA specimen demonstrated the least stiffness reduction among all specimens. This finding underscores the greater influence of mild steel on stiffness degradation compared to prestressing steel. Additionally, the RC-10-NA specimen likely benefited from superior bonding between its longitudinal rebar and the surrounding concrete compared to the bonding between prestressing steel and concrete.

CHAPTER 3

PARAMETRIC AND NUMERICAL STUDY

In this section, a parametric study was conducted to propose the minimum mild steel ratio for bonded post-tensioned reinforced concrete beams. Additionally, non-linear finite element analyses were performed to make a comparison with the experimental results of test specimens. Based on the calibrated numerical models, stress profiles for reinforcing steel and prestressing strands were developed to estimate plastic hinge lengths of test beams. In addition, maximum crack width, tendon stress, confined concrete strain, and ultimate curvature analyzed through finite element simulations were compared with the laboratory outputs and design code limits.

3.1 Parametric Study

This section outlines a straightforward approach employed to determine the required mild steel ratio satisfying a ductile response. The analysis was carried out using specific assumptions. For instance, Grade 420 mild steel conforming to ASTM A615 specifications was used for longitudinal reinforcement. Seven-wire low-relaxation strands were considered for prestressing steel, as defined by ASTM A416. The reinforcing steel was modeled by considering an elastic-perfectly plastic stress-strain response. The compression behavior of concrete was represented by the equivalent rectangular stress block approach, however, its tensile strength was neglected. Besides, the concrete section incorporated a single layer of mild steel and a post-tensioning tendon.

To guarantee a ductile behavior, the strain (ε_s) at the level of the mild steel nearest to the tension face was set to 0.005 mm/mm, aligning with the minimum requirement specified in ACI 318. The analysis minimized the required longitudinal reinforcement ratio by maximizing the prestressing steel area, adhering to the upper

limit of the prestressing steel index (ψ_p) designated in TS3233. Equation 3-1 provides the corresponding calculation framework. In this equation, f_{cd} stands for design strength of concrete, whereas f_{pd} denotes design strength of prestressing strand. Besides, post-tensioning tendon area is described by A_{ps}. The ratio of d_p to d was selected within the range of 0.4 to 0.8. The lower bound of this range is deemed acceptable based on considerations such as preliminary design dimensions, the parabolic geometry of the tendon, and engineering judgement. For the upper bound, ACI 318 specifies that d_p must not exceed $0.8h$, where h represents the section depth. Accordingly, it might be considered that this range is reasonable and practical for design applications.

$$\psi_p = \frac{A_{ps}}{b_w d_p} \frac{f_{pd}}{f_{cd}} \leq 0.25 \tag{3-1}$$

To ensure a ductile response, it is essential that the tension steel yields prior to the concrete reaches its ultimate crushing strain ($\varepsilon_{cu} = 0.003\ \text{mm/mm}$). The strain profile and stress distribution for a post-tensioned reinforced concrete rectangular beam section are depicted in Figure 3.1. As can be seen from this figure, the strain (ε_s) in the tension steel exceeds the yield strain (ε_y), that is, the tension steel stress reaches its design yield strength (f_{yd}). Additionally, the stress in the prestressing steel (f_{ps}) can be calculated using Equation 3-2 provided in ACI 318.

$$f_{ps} = f_{pd}\left\{1 - \frac{\gamma_p}{\beta_1}\left[\rho_p \frac{f_{pu}}{f_c'} + \frac{d}{d_p} \frac{f_y}{f_c'}(\rho - \rho')\right]\right\} \tag{3-2}$$

where:

γ_p: factor used for prestressing reinforcement type,

β_1: factor relating depth of equivalent rectangular compressive stress block to depth of neutral axis,

ρ: tension steel ratio,

ρ': compression steel ratio,

ρ_p: prestressing steel ratio.

The neutral axis depth, denoted as c, was determined using strain compatibility principles (Equation 3-3). Subsequently, this calculated depth was utilized in Equation 3-4 to compute the compressive force in concrete (F_c), then, the required area of tensile reinforcement (A_s) was obtained (Equation 3-5).

$$\frac{\varepsilon_{cu}}{\varepsilon_s} = \frac{0.003}{0.005} = \frac{c}{d-c} \longrightarrow c = \frac{3d}{8} \tag{3-3}$$

$$(\overrightarrow{+}) \sum F_x = F_s + F_{ps} - F_c = 0 \tag{3-4}$$

where:

F_s: force due to reinforcing steel ($f_{yd}A_s$),

F_{ps}: force due to prestressing steel ($f_{ps}A_{ps}$),

F_c: force due to concrete ($0.85f_{cd}\beta_1 c b_w$).

$$A_s = \frac{0.31875 f_{cd}\beta_1 b_w d - \psi_p f_{cd} b_w d_p (1 - \frac{\gamma_p f_{pu} f_{cd}\psi_p}{\beta_1 f_c' f_{pd}})}{f_{yd} - \psi_p f_{cd}\frac{\gamma_p}{\beta_1 f_c'} f_y} \tag{3-5}$$

Finally, Equation 3-5 was divided by the term of ($b_w d$) to reach the minimum value of ρ.

$$\rho = \frac{0.31875 f_{cd}\beta_1 + \frac{\psi_p f_{cd} d_p}{d}(\frac{\gamma_p}{\beta_1 f_c'}\frac{\psi_p f_{cd} f_{pu}}{f_{pd}} - 1)}{f_{yd} - \psi_p f_{cd}\frac{\gamma_p}{\beta_1 f_c'} f_y} \tag{3-6}$$
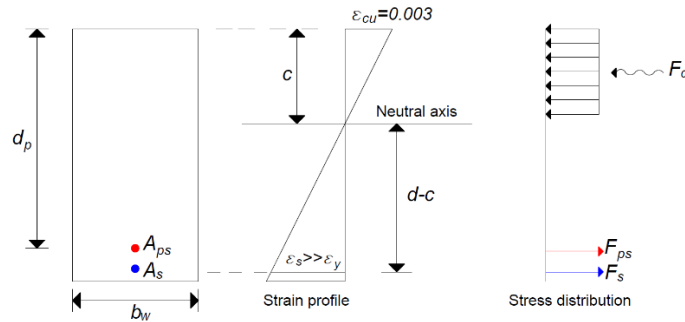
Figure 3.1. Strain profile and stress distribution of prestressed section

Figure 3.2 depicts the relation between the tension steel ratio (ρ) and $\frac{d_p}{d}$ for various values of ψ_p. For practical purposes, where $\frac{d_p}{d}$ typically ranges between 0.6 and 0.7, the intersection points of the lines corresponding to different concrete grades can be interpreted as the minimum required tension steel ratio (ψ_p=0.25). Based on this analysis, it is recommended that bonded post-tensioned reinforced concrete beams incorporate a minimum mild steel ratio of approximately 0.6%. In comparison, ACI 318 specifies this limit as 0.4% for beams with unbonded tendons. From this point of view, ρ value of 0.0060 can be examined as a reasonable proposal. Experimental findings further corroborate this recommendation, as beams with higher mild steel ratios demonstrated superior performance during testing.

Figure 3.2. Tension steel ratio vs. $\frac{d_p}{d}$ comparison

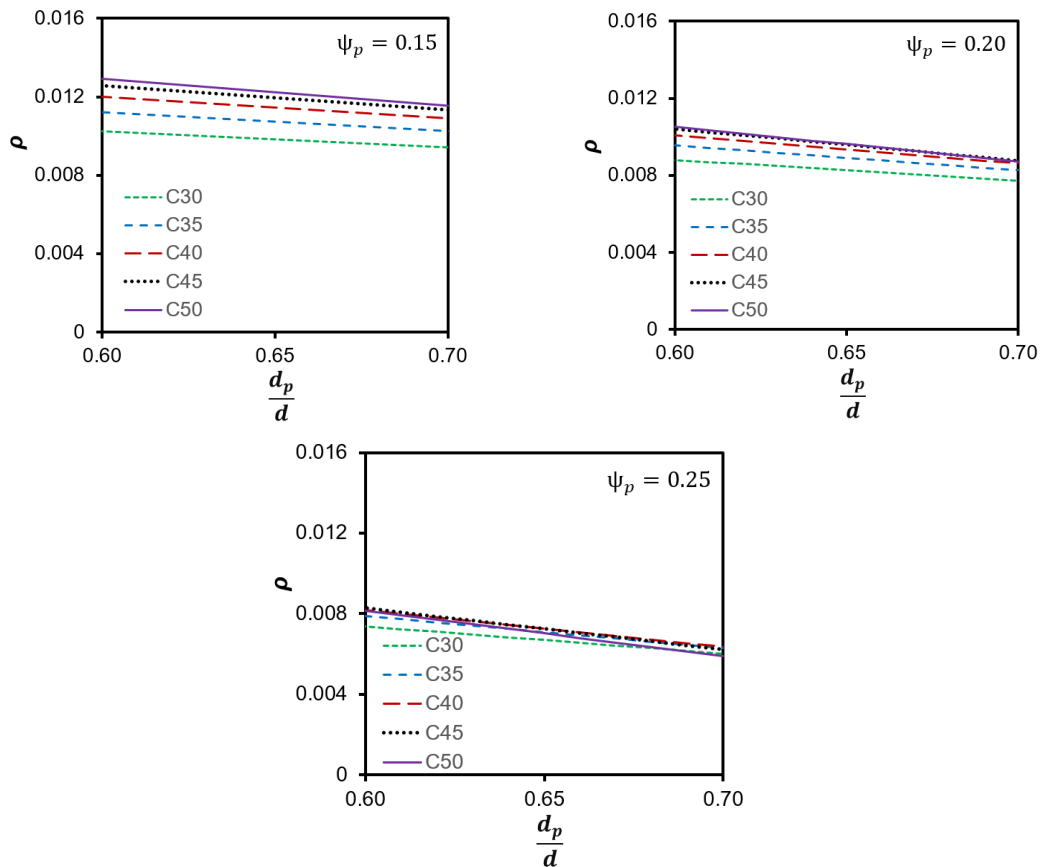## 3.2   Numerical Study

This section was conducted through the collaboration of Norgen Muka, Can Karageyik, and the author. In the scope of this research, the test specimens were investigated via non-linear structural analysis techniques. For this purpose, finite element models for exterior and interior test specimens were developed using DIANA (2012) software as illustrated in Figure 3.3. The material models used in this study are also explained in the following paragraph.

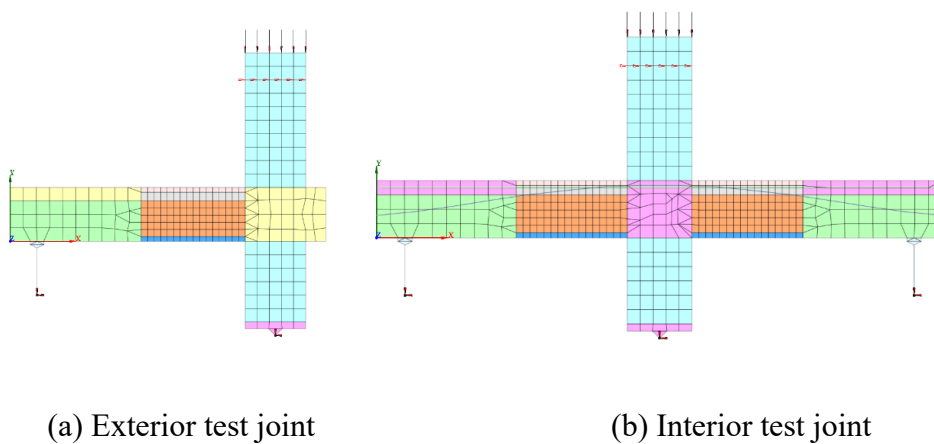(a) Exterior test joint   (b) Interior test joint

Figure 3.3. Finite element modeling for test specimens

Concrete was modeled using four-node quadrilateral iso-parametric plane stress elements (Q8MEM), while mild steel was described by one-dimensional (1D) embedded reinforcements exhibiting truss response. Furthermore, perfect bonding was assumed between the steel and surrounding concrete. Prestressing steel was considered as a reinforcement bar. A parabolic stress-strain relation was adopted for unconfined concrete in compression (see Figure 3.4a), and the confined concrete in the stirrup region was characterized using Mander et al. (1988) model. For concrete in tension, Hordijk (1991) model given in Figure 3.4b was implemented by means of the parameters derived from Hendriks et al.'s (2017) study. As can be seen from Figure 3.4c, the cyclic behavior of reinforcing steel was represented by Menegotto-Pinto (1973) model comprising Bauschinger effect (1886). It is essential to emphasize that the parameters used in this study were compiled from both Deaton's

(2013) study and calibration established between the experimental outputs and numerical model. Besides, concrete behavior was simulated using the total strain rotating crack model, where the material's orthotropic axes were aligned with the principal strain axes. Then, the constitutive material properties previously given in Table 2.12 were incorporated into these models. Consequently, their computational model parameters are summarized in Table 3.1.
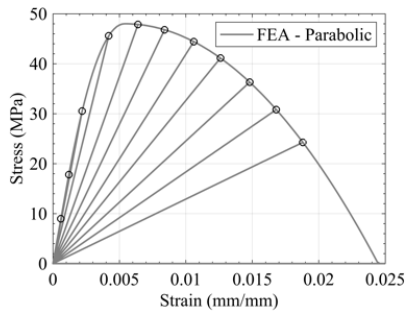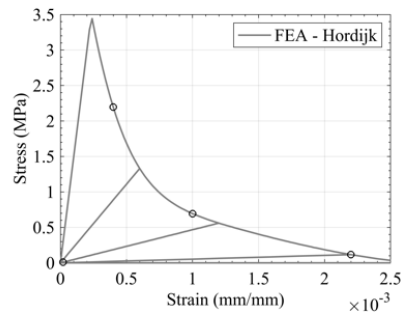
(a) Concrete in compression   (b) Concrete in tension
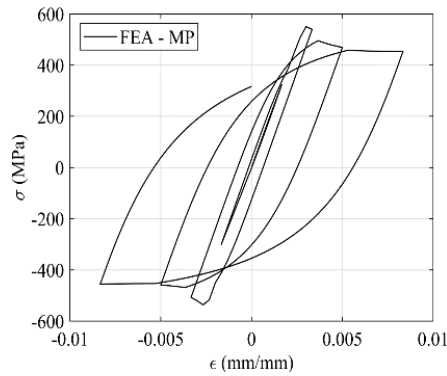
(c) Steel cyclic model

Figure 3.4. Stress-strain curves for the materials

Table 3.1 Material Parameters for Computational Modeling

Concrete		Steel	
Parameter	Value	Parameter	Value
G_f	0.103 N/mm	b	0.00336
G_C	30.528 N/mm	R_0	20.5
		a_1	19.5
		a_2	0.10
		a_3	0.00
		a_4	0.00

In Figure 3.5, the base shear-lateral displacement curves obtained from the finite element model (FEM) and laboratory works are compared for each specimen. Accordingly, it can be concluded that the numerical models accurately predicted the experimental results.

Figure 3.5. Base shear-lateral displacement comparison
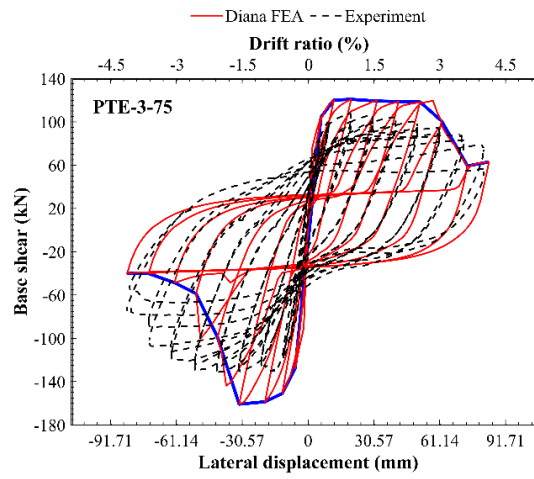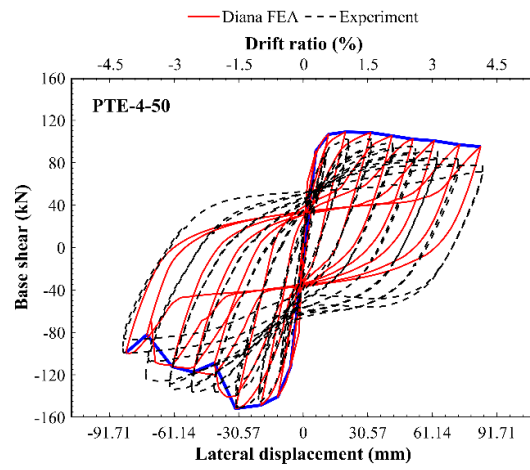
Figure 3.5. (cont'd)
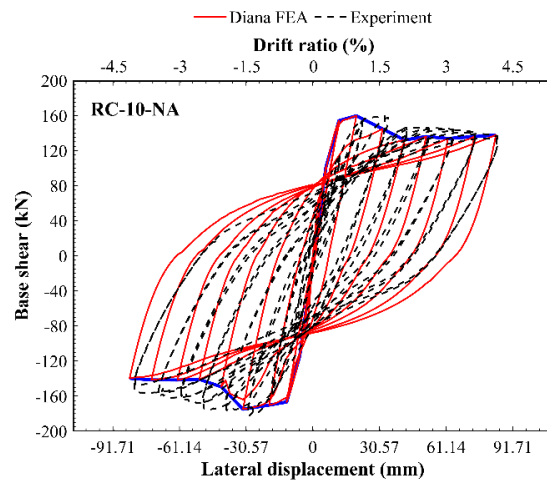
Figure 3.5. (cont'd)

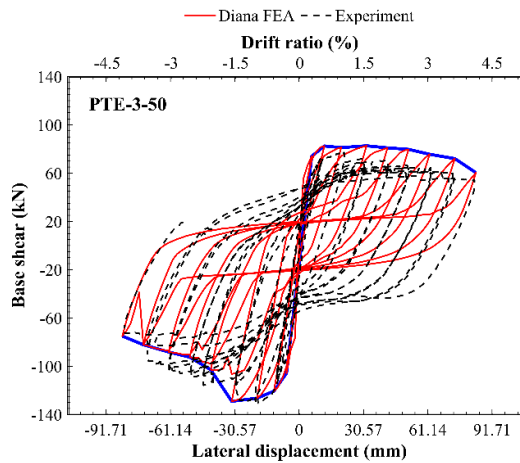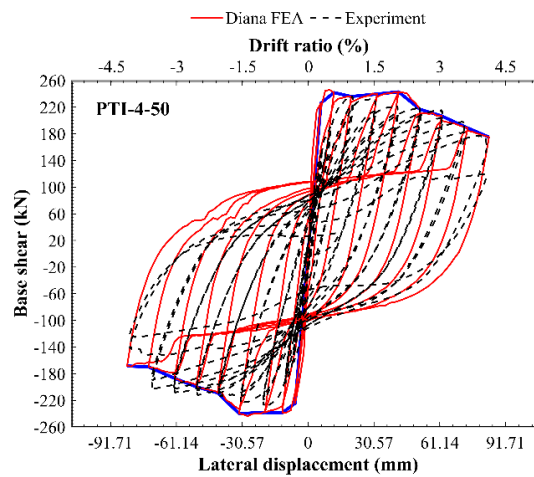The stress distribution of the prestressing steel along the shear span is depicted in Figure 3.6. The numerical analyses revealed that initial yielding occurred at a distance of approximately 12 cm from the column's outer face designated as datum point for all exterior post-tensioned joints, regardless of the variations in mild steel amount or load-balancing ratios. The following findings provided insights into the influence of design parameters on stress fluctuation:

i. Although the stress profiles for PTE-3-50 and PTE-4-50 were broadly similar, the onsets of constant stress zones occurred at approximately 51 cm and 62 cm, respectively. This difference might be linked to the higher reinforcing steel ratio in PTE-4-50, which reduced the rate of stress relaxation by mitigating abrupt stress degradation. At a drift ratio of 4% and a distance of $x = 20$ cm, the push-to-pull stress ratio was approximately 1.5 for PTE-4-50 and 1.3 for PTE-3-50, highlighting the role of the concrete flange width in enhancing compressive resistance under push loading. These factors resulted in significant stress concentrations at the beam-to-column joints during negative loading.

ii. Beyond a distance of $x = 50$ cm, PTE-3-50 and PTE-3-75 exhibited comparable stress values despite differences in their load-balancing ratios.

101

Then, it can be inferred that tendon area had a limited effect on stress distribution. On the contrary, deformation capacity appeared to be predominantly controlled by the mild steel amount. Furthermore, PTE-3-75 exhibited nearly identical stress levels at 4% drift ratio and $x = 20$ cm under both loading directions, whereas PTE-3-50 showed pronounced differences. The reasoning behind it is that the specimen converges to the behavior of a fully-prestressed beam as the higher load-balancing ratio is used, resulting in minimal stress variations between push and pull directions for PTE-3-75.

    iii. The interior specimen PTI-4-50 reached the first yielding point within a shorter length segment compared to the exterior specimen PTE-4-50. This behavior can be attributed to the symmetrical tendon layout of PTI-4-50, which provided a uniform load distribution (i.e., effective load transfer mechanism) across both shear spans.

Figure 3.7 and Figure 3.8 represent the stress profiles of the top and bottom reinforcements, which experienced tensile forces in the pull and push directions, respectively. The results demonstrated that tensile stresses in the push direction were substantially higher than those in the pull direction at longer distances (i.e., $x = 60$ cm), consistent with the influence of the parabolic prestressing steel layout in enhancing tensile capacity under push loading. Additionally, initial yielding was observed at approximately 8 cm for all post-tensioned specimens, whereas the conventional RC-10-NA specimen, characterized by a higher mild steel ratio, exhibited delayed yielding at approximately 14 cm.
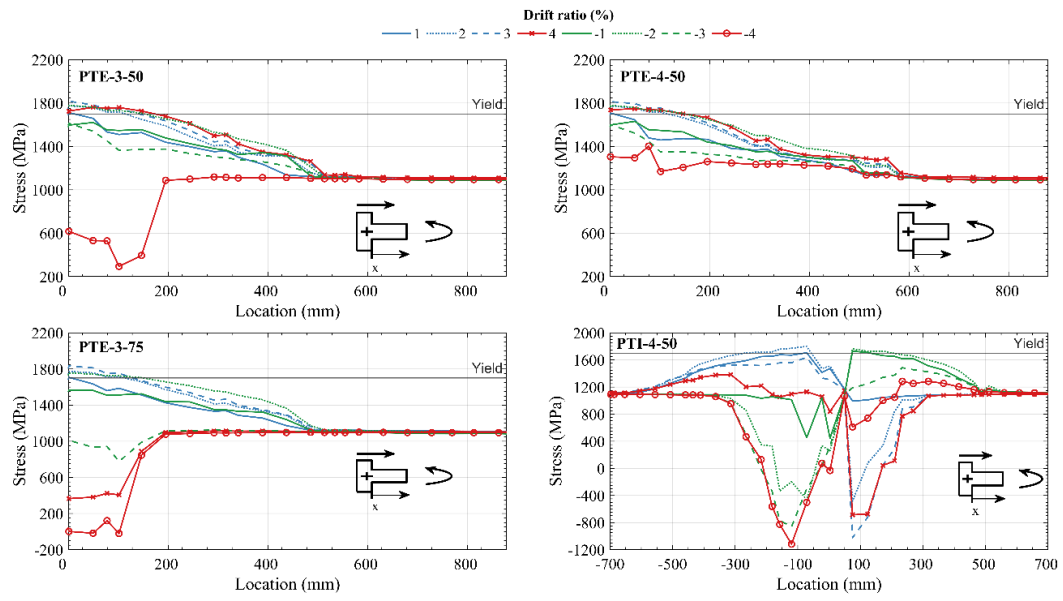
Figure 3.6. Stress profiles for prestressing steel
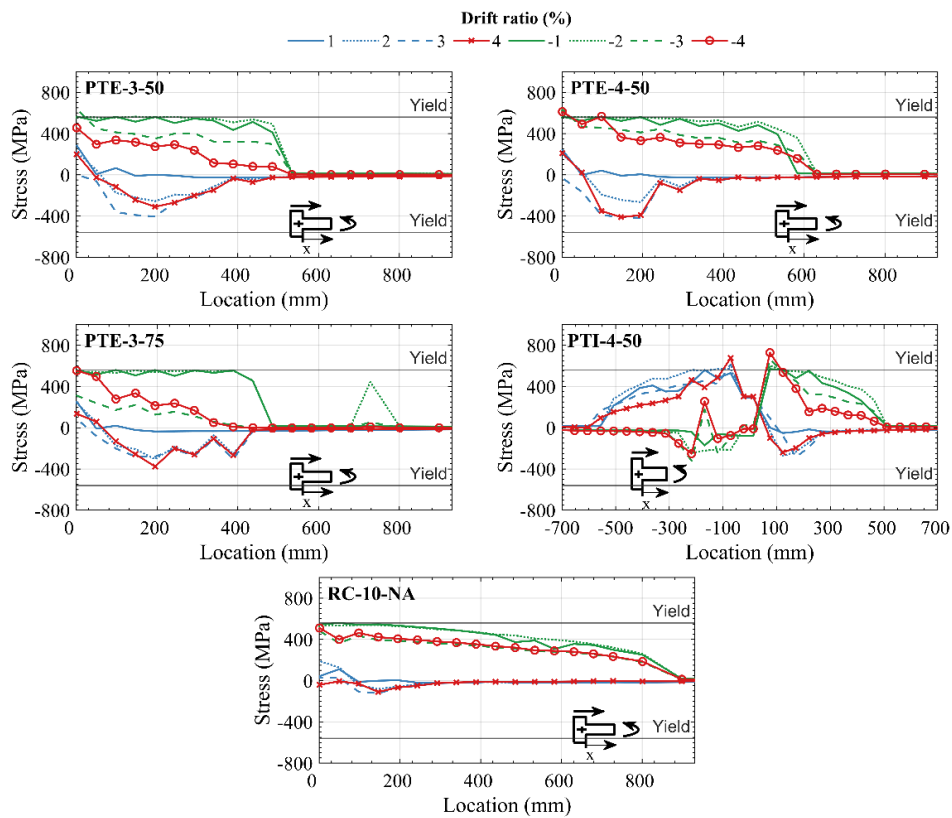
Figure 3.7. Stress profiles for beam top reinforcement
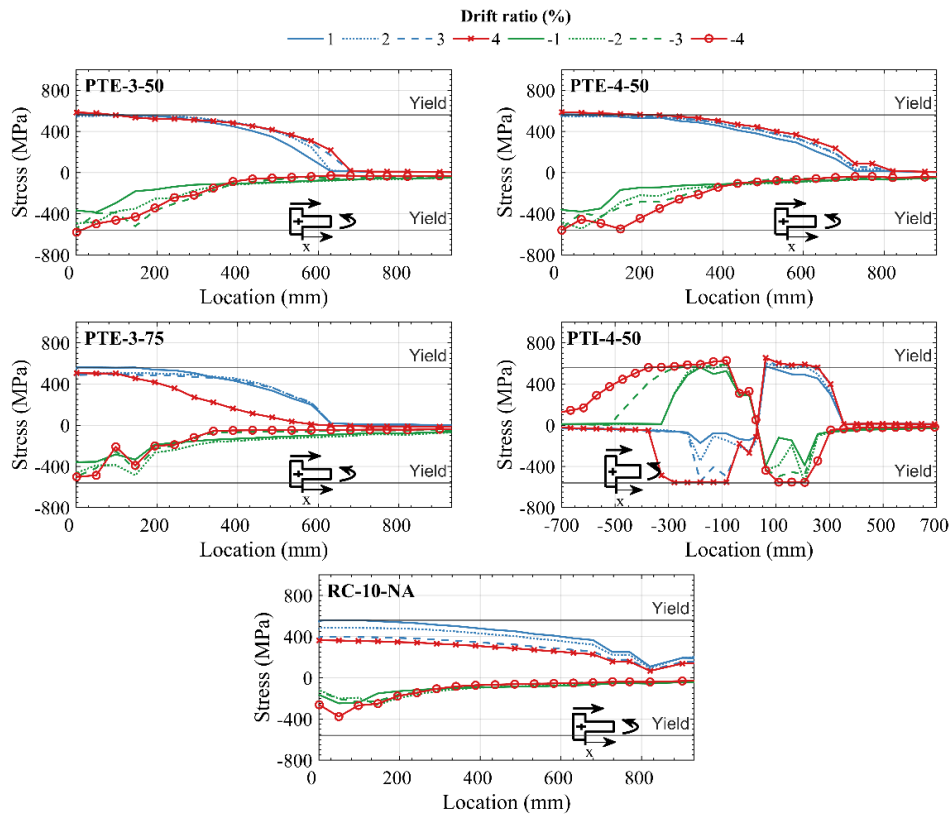
Figure 3.8. Stress profiles for beam bottom reinforcement

Based on Figures 3.6, 3.7, 3.8, the points corresponding to the onset of yielding were specified and the average of these values was subsequently utilized to obtain the plastic hinge length (l_p) of the test beams. It is also known that several analytical approaches have been developed to approximate the beam plastic hinge location. For example, Mattock (1965) derived a formula that integrates the effective depth of the beam and the shear span as primary variables. Priestley and Park (1987) proposed an empirical expression that correlates the plastic hinge length with the shear span (z) and the diameter of the longitudinal reinforcement (d_b). Also, Berry et al. (2008) presented a more comprehensive equation incorporating additional material properties such as the yield strength of steel and the compressive strength of concrete, to account for their influence on the plastic hinge characteristics. All these suggestions are given below:

$$l_p = 0.5d + 0.05z \qquad (3-7) \qquad (\text{Mattock (1965)})$$

104

$$l_p = 0.08z + 6d_b \qquad \text{(3-8)} \qquad \text{(Priestley and Park (1987))}$$

$$l_p = 0.05z + 0.1d_b f_y/\sqrt{f_c'} \qquad \text{(3-9)} \qquad \text{(Berry et al. (1965))}$$

Table 3.2 introduces a comparison between finite element analyses, analytical equations, and experimental observations. It demonstrates a high level of consistency, reflecting the reliability of both the numerical simulations and the empirical models in estimating the plastic hinge lengths.

Table 3.2 Plastic Hinge Length Summary

Specimen	Experiment	Mattock (1965)	Priestley & Park (1987)	Berry (2008)	Average	FE analysis
PTE-3-50	227	256.0	196.0	178.3	210.1	242
PTE-4-50	235	255.5	208.0	200.4	221.3	241
PTE-3-75	231	256.0	196.0	175.0	209.0	247
PTI-4-50	239	255.5	208.0	193.3	218.9	253
RC-10-NA	241	253.5	256.0	251.3	253.6	219

Note: All values are in mm.

Furthermore, the crack propagation patterns at 4% drift ratio are illustrated in Figure 3.9. Accordingly, cracks exceeding 0.2 mm in width are highlighted in blue, while those exceeding 0.5 mm are marked in red, providing a clear visualization of the damage distribution under reverse cyclic loading.

(a) PTE-3-50   (b) PTE-4-50   (c) PTE-3-75

(d) PTI-4-50   (e) RC-10-NA
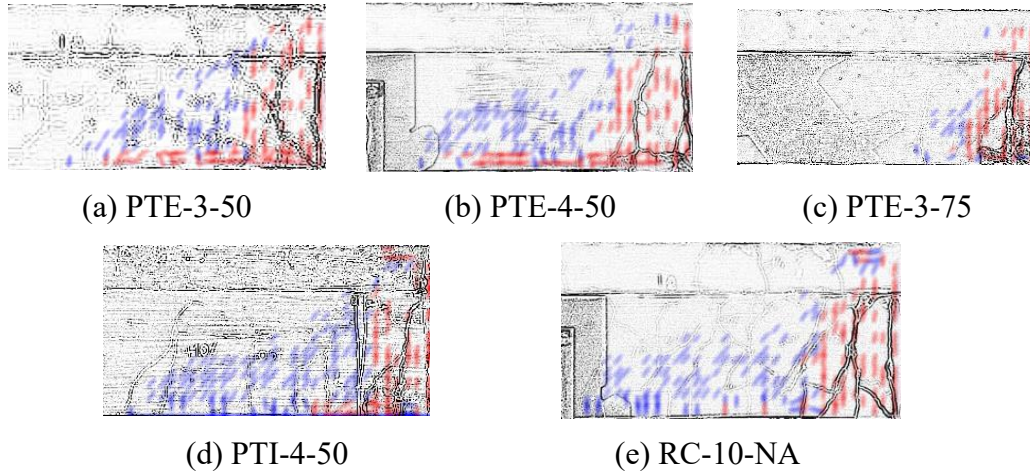
Figure 3.9. Crack propagations at 4% drift ratio

Apart from those, finite element analysis results of post-tensioned test specimens were evaluated through the laboratory work and design codes. Accordingly, the discussions focusing on the comparisons of the maximum crack width, tendon stress, confined concrete strain, and ultimate curvature are presented as follows:

i.   Maximum crack width

The average stress values along the plastic hinge length at drift ratios of 1%, 2%, and 3% were derived for the prestressing steel. Then, the strain values (ε_{ps}) were calculated using the stress-strain response of the tendon. Lastly, maximum crack widths were obtained by multiplying these average strains by the specimens' plastic hinge lengths. The crack widths measured during the testing are compared with those predicted by the numerical model, as illustrated in Figure 3.10. Accordingly, numerical model overestimated the crack widths as compared to the experimental results up to a drift ratio of 1% .

.
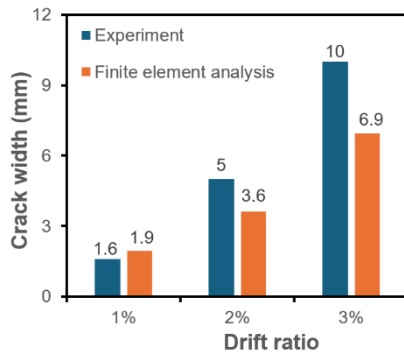
(a) PTE-3-50
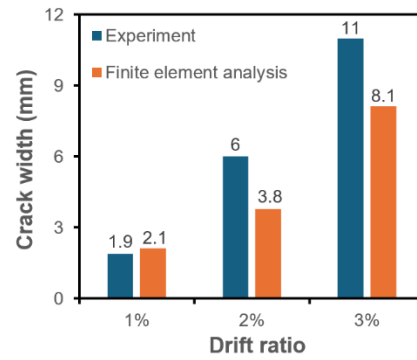
(b) PTE-4-50
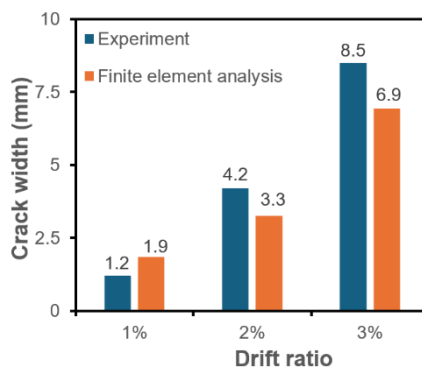
(c) PTE-3-75
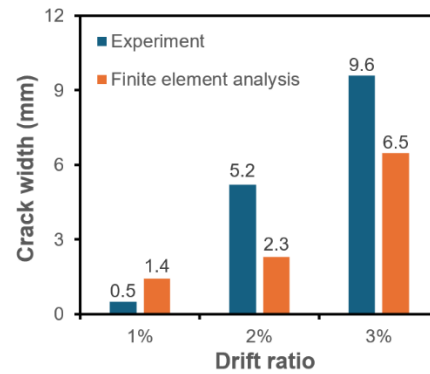
(d) PTI-4-50

Figure 3.10. Crack width comparison between numerical model and experimental results

ii.   Tendon stress

Figure 3.11 compares the tendon stresses (f_{ps}) computed based on ACI 318 recommendations, observed during the experiments, and obtained through finite element simulations at a drift ratio of 3%. Accordingly, the maximum tendon stress was determined using ACI 318 equation compared to other approaches. It can be attributed to the conservative nature of the design codes. Furthermore, a reasonable agreement was reached among all methods for all test beams, except for the laboratory results of PTE-4-50. This situation might result from an issue with the malfunction of jacking operational system.
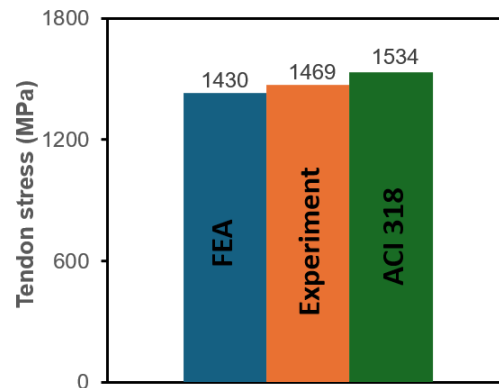
Figure 3.11. Tendon stress comparison between finite element modeling, experimental observations, and ACI 318 proposal

iii.   Confined concrete strain

The average strain (ε_{ps}) for prestressing steel was obtained as previously explained in part-i. The ultimate curvature (ϕ_u) presented in Table 2.15 was used to obtain the confined concrete strain ($\varepsilon_{cu,c}$) at the tension steel level. For this purpose, the strain profile was drawn based on the fundamental assumption of ultimate limit state, namely that plane section remains plane (see Figure 3.12).
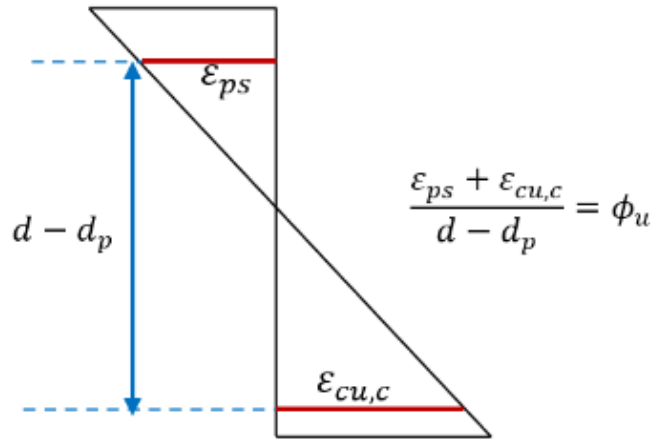
Figure 3.12. Strain profile

Then, the computed strain was compared with the confined concrete strain at collapse prevention (CP) limit state defined by TBEC (see Equation 3-10). The results are summarized in Table 3.3. To ensure safety, the design code provided lower limit values as compared to those obtained from numerical modeling and laboratory study.

$$\varepsilon_c{}^{CP} = 0.0035 + 0.04\sqrt{a_{se}\rho_{sh,min}\frac{f_{ywe}}{f_{ce}}} \leq 0.018 \qquad (3\text{-}10)$$

where:

$\varepsilon_c{}^{CP}$: confined concrete strain at collapse prevention limit state,

α_{se}: coefficient for confining steel,

$\rho_{sh,min}$: minimum of the volumetric ratio of the transverse reinforcement in both directions,

f_{ywe}: average yield strength of the transverse reinforcement,

f_{ce}: average compressive strength of the concrete.

Table 3.3 A Comparison for Confined Concrete Strain

Specimen label	TBEC	Numerical model & experimental work
PTE-3-50	0.01013	0.01025
PTE-4-50	0.01052	0.01250
PTE-3-75	0.00998	0.01220
PTI-4-50	0.01019	0.01327

iv.   Ultimate curvature

The design target for the drift ratio (DR) was specified (for instance, 3% drift). By using the yield curvature (ϕ_y) given in Table 2.15, ultimate curvature (ϕ_u) was calculated through Equation 3-11 applicable to the cantilever beam. Consequently, ultimate curvature values obtained from numerical model and experiments are summarized in Table 3.4. This table indicates that finite element modeling well predicted the experimental measurements, except for the interior specimen PTI-4-50.

$$\left(\phi_u - \phi_y\right)l_p + \frac{\phi_y L}{3} = DR \qquad (3\text{-}11)$$

Table 3.4 A Summary for Ultimate Curvature Evaluation

Specimen label	Finite element analyses	Laboratory results
PTE-3-50	105.4	95.5
PTE-4-50	124.5	120.0
PTE-3-75	121.4	111.8
PTI-4-50	118.7	171.0

Note: All units are in rad/km.

CHAPTER 4

CONCLUSION

In the scope of this research, the seismic performance of post-tensioned cast-in-place reinforced concrete beams subjected to reverse cyclic loading was investigated. In this regard, firstly, an extensive experimental program was conducted. It was aimed to discover the effects of mild steel amount, load-balancing ratio, and specimen location on the structural performance of beam-to-column sub-assemblages. In addition to the beams with post-tensioning strands, a conventional test beam reinforced with mild steel only was constructed as reference specimen. Secondly, a parametric study was prepared to propose the minimum mild steel ratio for bonded post-tensioned beams. Lastly, non-linear finite element analyses were performed to simulate specimen behavior, then, they were validated with the experimental findings. Additionally, the beam plastic hinge lengths measured during the tests were compared with the computational modeling results. Apart from those, discussions were carried out between finite element modeling, laboratory work, and design codes by examining the maximum crack width, tendon stress, confined concrete strain, and ultimate curvature. Based on the results of limited number of test specimens, the following key conclusions can be drawn:

▪ The displacement ductility of post-tensioned reinforced concrete beams is strongly influenced by the mild steel amount. An increase in the mild steel content both in the tension and compression sides (keeping them equal) enhances the ductility of the beams. This is contradictory according to the code given expression stating that $(\rho - \rho')$ is proportional to ductility of reinforced concrete beams.

▪ The curvature ductility and displacement ductility are not substantially affected by load-balancing ratio conducted within the scope of project varying between 0.5 to 0.75.

▪ As a result of less ductile nature of prestressing strand working nearly linear elastic zone during significant inelastic action of beam ends and increase of compressive strain demands in concrete due to the presence of prestressing strands, a reduction in the energy dissipation capacity is expected in post-tensioned beams compared to conventional reinforced concrete beams.

▪ Post-tensioning effectively limits the residual crack widths, thereby reducing the necessity for post-earthquake repairs, particularly when the ultimate drift demands remain below 1%. It might be explained by the self-centering ability of post-tensioning.

▪ The standard fiber-based section analyses demonstrated reasonable accuracy in estimating the moment-curvature responses of the test specimens.

▪ The experimental and finite element analysis results reasonably agreed in terms of load-displacement response including cyclic degradation.

▪ A good agreement was achieved between finite element analyses and experimental results when the maximum crack width, tendon stress, confined concrete strain, and ultimate curvature were compared.

▪ The calibrated material models derived from these analyses can be utilized in non-linear dynamic simulations to evaluate the ductility of frame structures incorporating post-tensioned beams.

▪ Based on experimental data, finite element simulations, and theoretical considerations, a minimum tensile mild steel ratio of 0.60% is proposed to achieve a sufficient displacement ductility. This value of minimum reinforcement ratio can be used by limiting interstory drift ratio to 2% and selecting the response modification factor as 4, based on the results of this study and Karageyik (2024).

REFERENCES

Aalami, B. O. (2023). *Post-Tensioning in Building Construction*. CRC Press.

Alcocer, S. M., Carranza, R., Perez-Navarrete, D., & Martinez, R. (2002). Seismic tests of beam-to-column connections in a precast concrete frame. *PCI Journal*, *47*(3). https://doi.org/10.15554/pcij.05012002.70.89.

American Concrete Institute. (2019). *Building code requirements for structural concrete* (ACI 318).

American Society for Testing and Materials. (2018). *Standard specification for low-relaxation, seven-wire steel strand for prestressed concrete* (ASTM A416).

American Society for Testing and Materials. (2022). *Standard specification for deformed and plain carbon- steel bars for concrete reinforcement* (ASTM A615).

Bauschinger, J. (1886). On the change of the position of elastic limit of iron and steel under cyclic variation of stress. *Mitt. Mech.-Tech. Lab., Munich*, 13 (1).

Berry, M. P., Lehman, D. E., & Lowes, L. N. (2008). Lumped-plasticity models for performance simulation of bridge columns. *ACI Structural Journal*, 105(3), 270–279. https://doi.org/10.14359/19786.

Cai, X., Pan, Z., Zhu, Y., Gong, N., & Wang, Y. (2021). Experimental and numerical investigations of self-centering post-tensioned precast beam-to-column connections with steel top and seat angles. *Engineering Structures*, *226*, 1–17. https://doi.org/10.1016/j.engstruct.2020.111397.

Cheok, G. S., & Lew, H. S. (1991). Performance of precast concrete beam-to-column connections subject to cyclic loading. *PCI Journal*, *36*(3), 56–67. https://doi.org/10.15554/pcij.05011991.56.67.

Cheok, G. S., & Lew, H. S. (1993). Model precast concrete beam-to-column connections subject to cyclic loading. *PCI Journal*, *38*(4), 80–92. https://doi.org/10.15554/pcij.07011993.80.92.

Chopra, A. K. (2015). *Dynamics of Structures: Theory and Applications to Earthquake Engineering*. Prentice Hall.

Davey, M. J., Abdouka, K., & Al-Mahaidi, R. (2016). Exterior post-tensioned band beam to column connections under earthquake loading. *Australian Journal of Structural Engineering*, *17*(1). https://doi.org/10.1080/13287982.2015.1116179.

Deaton, J.B. (2013). *Nonlinear finite element analysis of reinforced concrete exterior beam-to-column joints with nonseismic detailing* [Doctoral dissertation, Georgia Institute of Technology].

Diana (2012). *User's Manual - Release 9.4.4*. Delft: TNO Building and Construction Research.

El-Sheikh, M. T., Sause, R., Pessiki, S., & Lu, L. W. (1999). Seismic behavior and design of unbonded post-tensioned precast concrete frames. *PCI Journal*, *44*(3). https://doi.org/10.15554/pcij.05011999.54.71.

Elwood, K. J., & Moehle, J. P. (2003). Shake table tests on the axial load failure of rein forced concrete columns. *Proceedings of the Fib Symposium 2003: Concrete Structures in Seismic Regions*.

European Standard. (2004). *Eurocode 2: Design of concrete structures - Part 1-1: General rules and rules for building*s (EN 1992-1-1).

Federal Emergency Management Agency. (2007). *Interim protocols for determining seismic performance characteristics of structural and nonstructural components through laboratory testing* (FEMA 461).

Feng, S., Yang, Y., Xue, Y., & Yu, Y. (2021). A post-tensioned hybrid beam-column connection with a web friction device: Experimental study and theoretical analysis. *Journal of Building Engineering*, *43*. https://doi.org/10.1016/j.jobe.2021.103105.

Guan, D., Yang, H., Ju, D., Guo, Z., & Yang, S. (2019). Cyclic loading test on a locally post-tensioned precast concrete beam–column connection. *Advances in Structural Engineering*, *22*(12). https://doi.org/10.1177/1369433219849811.

Hamahara, M., Nishiyama, M., Okamoto, H., & Watanabe, F. (2007). Design for shear of prestressed concrete beam-column joint cores. *Journal of Structural Engineering*, *133*(11). https://doi.org/10.1061/(asce)0733-9445(2007)133:11(1520).

Hawileh, R. A., Rahman, A., & Tabatabai, H. (2010). Nonlinear finite element analysis and modeling of a precast hybrid beam-column connection subjected to cyclic loads. *Applied Mathematical Modelling*, *34*(9). https://doi.org/10.1016/j.apm.2009.11.020.

Hendriks, M.A.N., Boer, A., & Belletti, B. (2017). *Guidelines for Nonlinear Finite Element Analysis of Concrete Structures, Rijkswaterstaat Centre for Infrastructure*. Report RTD:1016-1.

Hordijk, D.A. (1991). *Local approach to fatigue of concrete* [Doctoral dissertation, Delft University of Technology].

Huang, L., Zhou, Z., Huang, X., & Wang, Y. (2020). Variable friction damped self-centering precast concrete beam–column connections with hidden corbels: Experimental investigation and theoretical analysis. *Engineering Structures*, *206*. https://doi.org/10.1016/j.engstruct.2019.110150.

Huang, L., Clayton, P. M., & Zhou, Z. (2021). Seismic design and performance of self-centering precast concrete frames with variable friction dampers. *Engineering Structures*, *245*. https://doi.org/10.1016/j.engstruct.2021.112863.

Hwang, J. H., Kim, K. S., Choi, S. H., Kwon, O. S., & Lee, D. H. (2021). Seismic behaviour of post-tensioned precast concrete beam–column connections. *Magazine of Concrete Research*, *73*(9). https://doi.org/10.1680/jmacr.19.00083.

Karageyik, C. (2024). Seismic behavior of post-tensioned beams [Doctoral dissertation, Middle East Technical University].

Kashiwazaki, T., & Noguchi, H. (2001). Seismic performance evaluation of beam-column joints for prestressed RC buildings with high performance materials. *High Performance Materials in Bridges*, 406–415. https://doi.org/https://doi.org/10.1061/40691(2003)36.

Khodaei, M., Saghafi, M. H., & Golafshar, A. (2021). Seismic retrofit of exterior beam-column joints using steel angles connected by PT bars. *Engineering Structures*, 236. https://doi.org/10.1016/j.engstruct.2021.112111.

Liao, X., Zhang, B., & Xue, W. (2024). Cyclic loading response of precast concrete beam-column connections with partially bonded draped prestressing tendon. *Engineering Structures*, *302*. https://doi.org/10.1016/j.engstruct.2023.117435.

Maddah, A., Golafshar, A., & Saghafi, M. H. (2020). 3D RC beam–column joints retrofitted by joint enlargement using steel angles and post-tensioned bolts. *Engineering Structures*, *220*. https://doi.org/10.1016/j.engstruct.2020.110975.

Mander, J. B., Priestley, M. J. N., & Park, R. (1988). Theoretical stress-strain model for confined concrete. *Journal of Structural Engineering*, *114*(8), 1804–1826. https://doi.org/10.1061/(asce)0733-9445(1988)114:8(1804).

Mattock, A. H. (1965). Rotational capacity of hinging regions in reinforced concrete beams. *American Concrete Institute, ACI Special Publication*, *SP-012*, 143–181. https://doi.org/10.14359/16716.

Menegotto, M., Pinto, P.E. (1973). *Method of analysis of cyclically loaded RC plane frames including changes in geometry and non-elastic behavior of elements under normal force and bending*. Preliminary Report IABSE vol 13.

Morgen, B. G., Morgen, B. G., & Kurama, Y. C. (2008). Seismic response evaluation of posttensioned precast concrete frames with friction dampers. *Journal of Structural Engineering*, https://doi.org/10.1061/(ASCE)0733-9445(2008)134:1(132).

Naaman, A. E., Harajli, M. H., & Wright, J. K. (1986). Analysis of ductility in partially prestressed concrete flexural members. *PCI Journal*, *31*(3). https://doi.org/10.15554/pcij.05011986.64.87.

Nawy, E. (2009). *Prestressed Concrete: A Fundamental Approach*. Prentice Hall.

Ozcan, O., Binici, B., & Ozcebe, G. (2008). Improving seismic performance of deficient reinforced concrete columns using carbon fiber-reinforced polymers. *Engineering Structures*, *30*(6). https://doi.org/10.1016/j.engstruct.2007.10.013.

Ozden, S., & Ertas, O. (2007). Behavior of unbonded, post-tensioned, precast concrete connections with different percentages of mild steel reinforcement. *PCI Journal*, *52*(2), 32–44. https://doi.org/10.15554/pcij.03012007.32.44.

Park, R., & Thompson, K. J. (1977). Cyclic load tests on prestressed and partially prestressed beam-column joints. *PCI Journal*, 22(5), 84–110. https://doi.org/10.15554/pcij.09011977.84.110.

Park, R. (1989). Evaluation of ductility of structures and structural assemblages from laboratory testing. *Bulletin of the New Zealand Society for Earthquake Engineering*, *22*(3). https://doi.org/10.5459/bnzsee.22.3.155-166

Paudel, S., Tanapornraweekit, G., & Tangtermsirikul, S. (2022). Numerical study on seismic performance improvement of composite wide beam-column interior joints. *Journal of Building Engineering*, *46*. https://doi.org/10.1016/j.jobe.2021.103637.

Priestley, M. J. N. & Park, R. (1987). Strength and ductility of concrete bridge columns under seismic loading. *ACI Structural Journal* 84, 61–76. https://doi.org/10.14359/2800.

Priestley, M. J. N., & Tao, J. R. (1993). Seismic response of precast prestressed concrete frames with partially debonded tendons. *PCI Journal*, *38*(1). https://doi.org/10.15554/pcij.01011993.58.69.

Priestley, M. J. N., & MacRae, G. A. (1996). Seismic tests of precast beam-to-column joint subassemblages with unbonded tendons. *PCI Journal*, *41*(1). https://doi.org/10.15554/pcij.01011996.64.81.

Qing, Y., Liu, Y., Wang, C. L., Du, D., & Meng, S. (2023). Experimental study of a post-tensioned precast concrete beam-column joint with energy dissipaters and partially-precast slabs. *Engineering Structures*, *285*. https://doi.org/10.1016/j.engstruct.2023.115988.

Sezen, H., & Moehle, J. P. (2003). Bond-slip behavior of rein forced concrete members. *Proceedings of the Fib Symposium 2003: Concrete Structures in Seismic Regions*.

Srisuwan, T., & Yooprasertchai, E. (2024). Effects of unbonded prestressing steel tendons and slit dampers on the seismic behavior of precast concrete beam-column joints. *Structures*, *59*. https://doi.org/10.1016/j.istruc.2023.105721.

Stanton, J., Stone, W. C., & Cheok, G. S. (1997). A hybrid reinforced precast frame for seismic regions. *PCI Journal*, *42*(2). https://doi.org/10.15554/pcij.03011997.20.23.

Stone, W. C., Cheok, G. S., & Stanton, J. (1995). Performance of hybrid moment-resisting precast beam-column concrete connections subjected to cyclic loading. *ACI Structural Journal*, *92*(2). https://doi.org/10.14359/1145.

Thompson, K. J., & Park, R. (1980). Ductility of prestressed and partially prestressed concrete beam sections. *PCI Journal*, *25*(2). https://doi.org/10.15554/pcij.03011980.46.70.

Turkish Standards. (1979). *Building code requirements for prestressed concrete* (TS3233).

Turkish Standards. (1997). *Design loads for buildings* (TS498).

Turkish Standards. (2000). *Requirements for design and construction of reinforced concrete structures* (TS500).

Turkish Standards. (2018). *Turkey building earthquake code* (TBEC).

Wang, H., Marino, E. M., Pan, P., Liu, H., & Nie, X. (2018). Experimental study of a novel precast prestressed reinforced concrete beam-to-column joint. *Engineering Structures*, *156*. https://doi.org/10.1016/j.engstruct.2017.11.011.

Wu, Z., Lu, X., Li, L., Bao, H., Lu, Z., & Yu, K. (2023). Seismic performance of full-scale self-centering reinforced concrete beam-column joints: Experimental, numerical and theoretical analysis. *Journal of Building Engineering*, *78*. https://doi.org/10.1016/j.jobe.2023.107683.

Yurdakul, Ö., & Avşar, Ö. (2016). Strengthening of substandard reinforced concrete beam-column joints by external post-tension rods. *Engineering Structures*, *107*. https://doi.org/10.1016/j.engstruct.2015.11.004.

Zhou, Y., Song, G., & Huang, W. (2020). Performance-based damage evaluation of hybrid joints. *Bulletin of Earthquake Engineering*, *18*(8), 3781–3816. https://doi.org/10.1007/s10518-020-00838-8.

APPENDICES

A. Calculation of Reaction Forces

Reaction forces were obtained through the deformed shapes of test specimens. Accordingly, Figure A.1 typically represents the free body diagrams of exterior test specimen in pull and push directions. Firstly, the angles at critical locations were computed using LVDT recordings. Then, force equilibrium equations were established as follows:

$$V = H.\cos\alpha + R_1.\sin\beta + N.\sin\theta \tag{A-1}$$

$$M_{j,lower} = V.\cos\theta.H_{bottom} + R_1.\sin\theta.H_{bottom} \tag{A-2}$$

$$M_{j,upper} = H.\cos\theta.(H_{top} - \Delta_v + h_{column}.\sin\theta) + H.\Delta_h.\sin\alpha \tag{A-3}$$

$$M_j = M_{j,lower} + M_{j,upper} \tag{A-4}$$

The reaction at the roller support, R_1, was measured using the strain gauge. While H stands for horizontal hydraulic jack force, N refers to the applied axial load on the column. V and R_2 correspond to the base shear and vertical reaction force at pinned support, respectively. $M_{j,lower}$ and $M_{j,upper}$ are the moments for lower story and upper story at the beam-to-column joint. Total moment at the connection region is denoted by M_j. Horizontal and vertical displacements monitored at the column tip are represented by Δ_h and Δ_v, respectively. While H_{top} is the vertical distance between horizontal hydraulic jack and top face of the beam, H_{bottom} indicates the vertical distance between top face of the beam and hinge at the column bottom. The equations given above can similarly be derived for the interior specimen due to its symmetrical geometry.
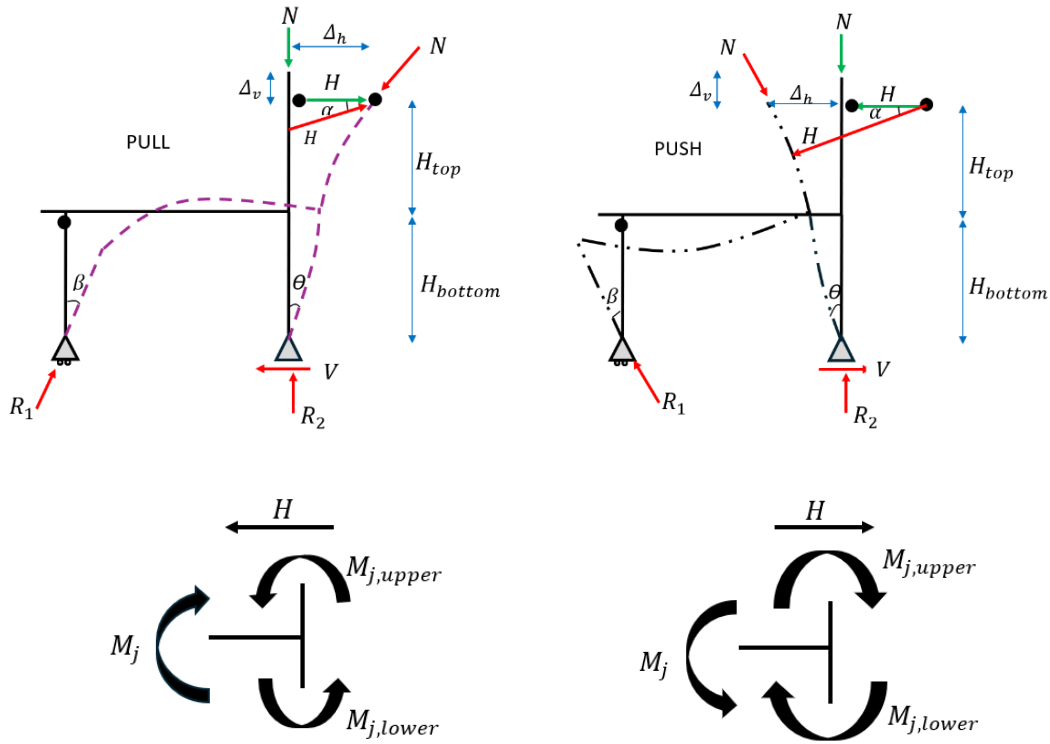
Figure A.1. Free body diagrams of deformed shapes of exterior test specimens

B. Calculation of Beam Curvature

Figure B.1 shows the typical strain profile for the exterior test specimen. Based on Table 2.13, beam curvature was computed with the help of four different LVDTs numbered as 8,10,12, and 14. Accordingly, top and bottom average strains were calculated as follows:

$$\varepsilon_{top} = \frac{\Delta L_{top}}{L_0} \qquad \varepsilon_{bottom} = \frac{\Delta L_{bottom}}{L_0} \qquad \text{(B-1)}$$

where:

ε_{top}= Average strain for top face of the beam,

ε_{bottom}= Average strain for bottom face of the beam,

ΔL_{top}= Average displacement for top face of the beam (LVDT #8,#10),

ΔL_{bottom}= Average displacement for bottom face of the beam (LVDT #12,#14),

L_o=Initial length.

Then, the algebraic summation of average strains were divided by h implying the vertical distance between top and bottom LVDTs to determine beam curvature (ϕ).

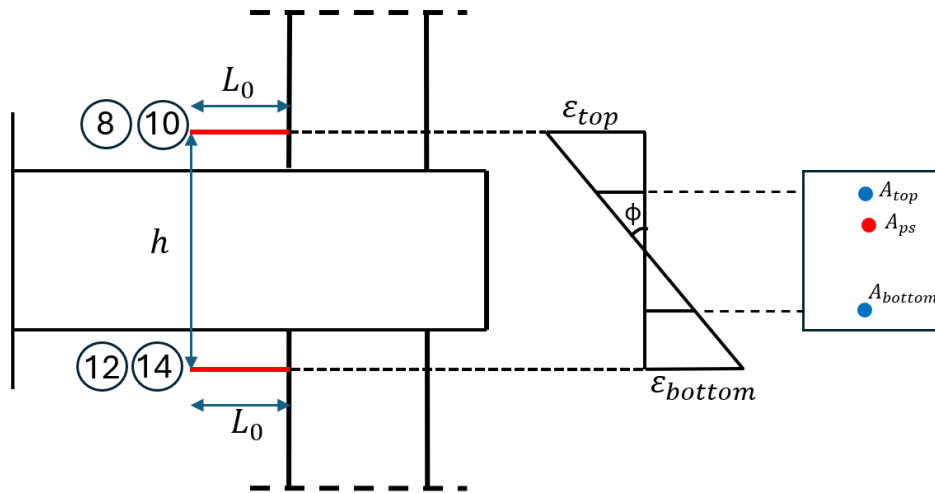$$\phi = \frac{\varepsilon_{top}+\varepsilon_{bottom}}{h} \qquad \text{(B-2)}$$

Figure B.1. Evaluation of beam curvature

CURRICULUM VITAE

Surname, Name: Tuncer, Ertürk

EDUCATION

Degree	Institution	Year of Graduation
MS	METU Civil Engineering	2018
BS	METU Civil Engineering	2014
High School	Kalaba Anatolian High School, Ankara	2009

WORK EXPERIENCE

Year	Place	Enrollment
2022-Present	TEDU	Instructor
2019-2022	TEDU	Research and teaching assistant
2016-2018	Promer Müşavirlik Mühendislik	Structural design engineer
2014-2016	Gen Mühendislik	Structural design engineer

FOREIGN LANGUAGES

Advanced English

PUBLICATIONS

1. Tuncer, E., Binici, B., & Canbay, E. (2021). Behavior and design of FRP bonded autoclaved aerated concrete beams. *Construction and Building Materials*, *282*. https://doi.org/10.1016/j.conbuildmat.2021.122712.